# Dehydration and Decarboxylation Reactions in Brønsted and Lewis Acidic Zeolites

Zur Erlangung des akademischen Grads eines

DOKTORS DER NATURWISSENSCHAFTEN
(Dr. rer. nat.)

von der KIT-Fakultät für Chemie und Biowissenschaften
des Karlsruher Instituts für Technologie (KIT)

genehmigte

DISSERTATION

von

Philipp Huber

1. Referent: Prof. Dr. Felix Studt
2. Referent: Dr. Sebastian Höfener
Tag der mündlichen Prüfung: 11.12.2023

# Abstract

Acidic zeolites play a pivotal role as versatile catalysts in the conversion of biomass-based materials into valuable chemicals, making them indispensable for a sustainable industry. While many aspects of zeolite catalysis are still incompletely understood, knowledge about reaction mechanisms and catalytically active centers is a prerequisite for optimizing catalytic processes. Obtaining this information only from experimental methods is challenging. Computational chemistry can fill this gap and enable further insights. In this work, I investigate Brønsted and Lewis acid sites (BASs and LASs) as well as reaction mechanisms in zeolites computationally with a particular focus on the H-SSZ-13 zeolite. Density functional theory in combination with single-point calculations for cluster models at the DLPNO-CCSD(T) level of theory as well as kinetic simulations for a batch reactor model are used. The results of this work are organized into three parts, each involving reaction mechanisms with dehydration or decarboxylation reactions.

In chapter 3, I discuss H-SSZ-13 surface models and their stability, which mainly depends on the number of silanol groups per area at the surface termination. Surface BASs and the BAS inside the zeolite bulk are equally stable. Surface LASs are more stable than BASs in presence of $H_2O$ above temperatures of approximately 150 °C. To evaluate the reactivity of both types of surface acid sites, the dehydration of methanol to dimethyl ether, an important reaction in zeolite catalysis, was investigated as a probe reaction. At BASs, a step-wise or concerted methanol dehydration can take place, where the concerted mechanism is less important. At LASs, only one mechanism occurs, which equals the concerted reaction at BASs with respect to free energy barriers. While formation of LASs is favored at zeolite surfaces, their role for methanol dehydration is insignificant. However, LASs might be more important for other reactions.

The reaction of acetic acid to isobutene is investigated in chapter 4 by computing reaction barriers at 400 °C in H-SSZ-13 and conducting a kinetic simulation. A zeolite surface acetate and a ketene, both formed from acetic acid, react to 3-oxobutanoic acid. Decarboxylation of 3-oxobutanoic acid yields acetone. After subsequent aldol self-condensation, mesityl oxide is formed, whose decomposition releases isobutene. The C-C coupling between the C2 derivatives is the rate-determining step. Acetone is transitionally formed with high concentrations as a stable intermediate before reacting further to isobutene. This study demonstrates that H-SSZ-13 can produce acetone or isobutene from acetic acid which can be obtained sustainably.

The conversion of methanol to olefins (MTO), another broad application of zeolites, is studied in chapter 5. After initiation, this process is co-catalyzed by the hydrocarbon pool. I investigated the initiation of the MTO process, i.e., the formation of olefins through direct C-C coupling, by computing Gibbs free energy profiles and conducting kinetic simulations at 400 °C in H-SSZ-13. I focused on mechanisms involving decarboxylation reactions to explain experimentally observed $CO_2$. Ketene is formed during the initiation process and can be further methylated. Ketene species can either react with formaldehyde

to $\beta$-lactones, which decarboxylate to olefins, or decarbonylate to olefins. Reaction barriers and kinetic simulations show that both mechanisms initiate the MTO process with similar efficiency. However, the amount of $CO_2$ formed during a kinetic simulation is lower than observed in experiments. Additionally, key reaction steps in H-SAPO-34 and H-ZSM-5 were computed. While barriers for decarboxylation reactions are similar for all three zeotypes, barriers for decarbonylation and methylation reactions are higher for H-SAPO-34 and lower for H-ZSM-5 compared to H-SSZ-13.

# Zusammenfassung

Als vielseitige Katalysatoren spielen saure Zeolithe eine zentrale Rolle bei der Umwandlung von Biomasse in nützliche Chemikalien und sind daher für eine nachhaltige Industrie unerlässlich. Viele Aspekte der Zeolithkatalyse sind noch nicht vollständig verstanden, jedoch stellt das Wissen über Reaktionsmechanismen und katalytisch aktive Zentren eine Grundvoraussetzung für die Optimierung katalytischer Prozesse dar. Diese Informationen über rein experimentelle Methoden zu erhalten ist eine Herausforderung. Kommen experimentelle Methoden an ihre Grenzen, ermöglicht die computergestützte Chemie weitere Einblicke auf atomarer Ebene. In dieser Arbeit untersuche ich mit computergestützten Methoden Brønsted- und Lewis-saure Zentren (BSZ und LSZ) sowie Reaktionsmechanismen in Zeolithen, insbesondere dem H-SSZ-13-Zeolithen. In diesem Zusammenhang habe ich Dichtefunktionaltheorie für periodische Strukturen in Kombination mit DLPNO-CCSD(T)-Rechnungen an Clustermodellen verwendet. Außerdem habe ich kinetische Simulationen für ein Rührkessel-Reaktor-Modell durchgeführt. Die Ergebnisse dieser Arbeit sind in drei Teile gegliedert, die Reaktionsmechanismen mit besonderem Fokus auf Dehydratisierungs- oder Decarboxylierungsreaktionen behandeln.

In Kapitel 3 diskutiere ich H-SSZ-13-Oberflächenmodelle und ihre Stabilität, die hauptsächlich von der Anzahl der Silanolgruppen pro Fläche an der Oberflächenterminierung abhängt. Die BSZ an der Oberfläche sind ebenso stabil wie die BSZ innerhalb des Zeolithkristalls. In Gegenwart von $H_2O$ sind Oberflächen-LSZ oberhalb von etwa 150 °C stabiler als BSZ. Um die Reaktivität beider Arten von Säurezentren zu evaluieren, habe ich die Dehydratisierung von Methanol zu Dimethylether, eine wichtige Reaktion in der Zeolithkatalyse, als Testreaktion untersucht. An BSZ kann eine dissoziative oder assoziative Methanol-Dehydratisierung stattfinden, wobei der assoziative Mechanismus weniger relevant ist. Für LSZ existiert nur ein Mechanismus, der bezüglich der freien Energiebarrieren der assoziativen Reaktion bei BSZ gleicht. Obwohl die Bildung von Oberflächen-LSZ wahrscheinlich ist, spielen diese für die Methanol-Dehydratisierung eine geringe Rolle. Für andere Reaktion könnten LSZ jedoch von größerer Bedeutung sein.

In Kapitel 4 untersuche ich die Reaktion von Essigsäure zu Isobuten in H-SSZ-13 durch Berechnung von Reaktionsbarrieren bei 400 °C und Durchführung einer kinetischen Simulation. Ein Zeolith-Oberflächenacetat und Keten, welche beide aus Essigsäure gebildet werden können, reagieren zu 3-Oxobutansäure. Die nachfolgende Decarboxylierung von 3-Oxobutansäure erzeugt Aceton. Nach anschließender Aldolkondensation bildet sich Mesityloxid, dessen Zersetzung Isobuten freisetzt. Die C-C-Kopplung zwischen den C2-Derivaten ist der geschwindigkeitsbestimmende Schritt. Aceton wird übergangsweise in hohen Konzentrationen als stabiles Zwischenprodukt gebildet, bevor es weiter zu Isobuten reagiert. Diese Studie zeigt, dass H-SSZ-13 Aceton oder Isobuten aus Essigsäure herstellen kann, die sich wiederum nachhaltig gewinnen lässt.

In Kapitel 5 untersuche ich die Umwandlung von Methanol in Olefine (methanol-to-olefins, MTO), eine weitere wichtige Anwendung von Zeolithen. Nach einer Initiierung läuft dieser Prozess co-katalysiert

durch den Kohlenwasserstoffpool ab. In diesem Zusammenhang habe ich die Initiierung des MTO-Prozesses erforscht, also die Bildung von Olefinen durch direkte C-C-Kopplung. Dafür habe ich Gibbs'sche freie Energieprofile bei 400 °C in H-SSZ-13 erstellt und kinetische Simulationen durchgeführt. Um die experimentell beobachtete Freisetzung von $CO_2$ zu erklären, habe ich mich insbesondere auf Mechanismen, die Decarboxylierungsreaktionen beinhalten, konzentriert. Keten wird während der Initiierung gebildet und kann weiter methyliert werden. Diese Ketenspezien können entweder zu Olefinen decarbonylieren oder mit Formaldehyd zu $\beta$-Lactonen reagieren, die weiter zu Olefinen decarboxylieren. Reaktionsbarrieren und kinetische Simulationen zeigen, dass beide Mechanismen den MTO-Prozess ähnlich effizient initiieren können. Allerdings ist die während der kinetischen Simulation gebildete Menge an $CO_2$ geringer als experimentell beobachtet. Zusätzlich habe ich wichtige Reaktionsschritte in H-SAPO-34 und H-ZSM-5 untersucht. Die Barrieren für Decarboxylierungsreaktionen sind in allen drei Zeolithen ähnlich. Die Barrieren für Decarbonylierungs- und Methylierungsreaktionen sind in H-SAPO-34 höher und in H-ZSM-5 niedriger als in H-SSZ-13.

# Contents

# 1

# Introduction

## 1.1 Motivation

The over-exploitation of fossil resources is the main driver of human-made global warming with all its negative consequences for environment and humanity. Between 1800 and 2021, the overall consumption of coal, oil, and gas increased exponentially from 0 TWh to 137 TWh (see Fig. 1.1), accompanied by the emission of greenhouse gases accelerating global warming. In 2021, the annual $CO_2$ emission reached 37,124 Gt, a value more than three orders of magnitude higher than the 28 Gt in 1900.[1] Caused by $CO_2$, $CH_4$, and $NO_2$ emissions, the global mean surface temperature has increased by 1.61 °C between 1851 and 2021 .[2] To fight global warming effectively, satisfying the growing population's demand for common commodities requires sustainable alternatives to the utilization of fossil resources in industry and energy.

Addressing this problem, renewable resources received more and more attention over the last decades. Substituting fossil with renewable resources can decrease the emission of greenhouse gases significantly. Since 1990, the *Web of Science* database[4] has shown an exponential increase of studies on renewable resources (see Fig. 1.2a). Zeolite catalysis is an important part of this subject that similarly has been increasingly investigated (see Fig. 1.2b). Zeolites can convert biomass-based resources into valuable chemicals.[5–8] For example, olefins can be obtained from methanol[9], acrylates can be converted to terephthalates,[10] and acetic acid reacts to acetone.[11].

Understanding and optimizing zeolite-catalyzed processes by unravelling the reaction mechanisms is a key for becoming independent of fossil resources. However, these mechanisms are intricate and revealing them experimentally is challenging. Computational chemistry provides complementary information by simulating and comparing reaction paths and evaluation different factors influencing catalytic processes.

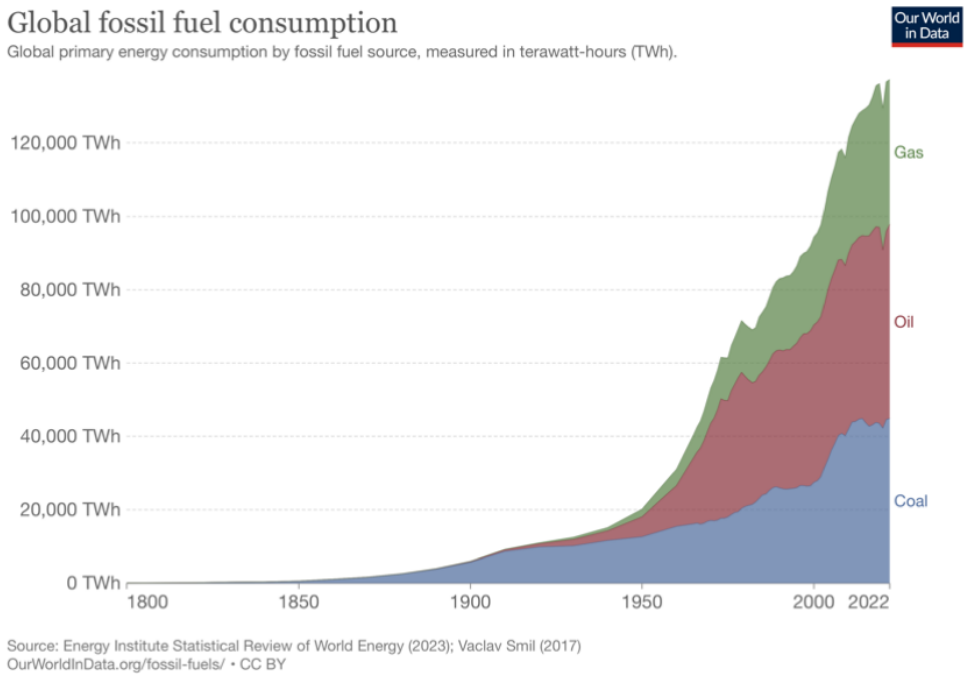


**Figure 1.1:** Global consumption of fossil fuels (coal, oil, gas) from 1800 to 2022. Provided by Ref. 3 with permission from OurWorldInData.org, copyright 2022.

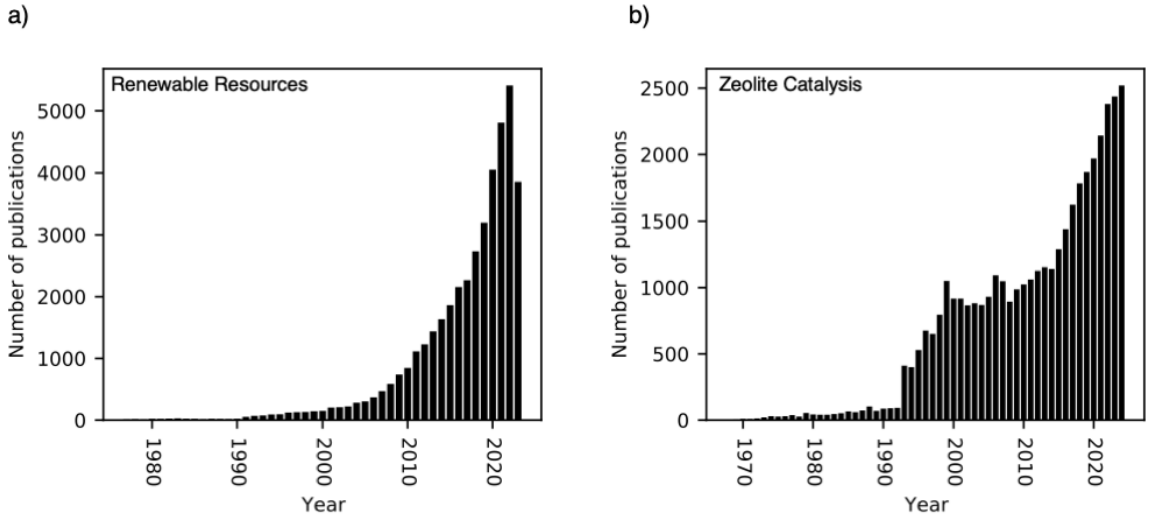


**Figure 1.2:** Publications accessible through the *Web of Science* database between 1977 and 2023, resulting from the search for keywords *Renewable resources* a) and *Zeolite catalys** b).[4]

In this thesis, I investigate zeolite-catalyzed processes computationally, aiming to improve our understanding of zeolites and thus contribute to a more sustainable world.

## 1.2 Zeolites

Zeolites were first described in 1756 when Cronstedt discovered a new material and derived their name from the Greek words "zéō" (boiling) and "lithos" (stone), since his zeolite was losing water. Nowadays, the *Structure Commission of the International Zeolite Association* lists about 250 different zeolites.[12] Zeolites are constructed from tetrahedral $SiO_4$ units (see Fig. 1.3a) which form a microporous framework with a three-dimensional network of pores and channels. Within this structure, the $SiO_4$ units are referred to as T-sites and generally not equivalent. These units can be connected in various ways, leading to frameworks of different pore and channel sizes.[13] Adding organic templates during synthesis allows to direct the process to a specific framework structure.[14–17] Figures 1.3b and 1.3c show the structures of the mordenite framework inverted (MFI) and chabazite (CHA) framework exemplarily.[1]

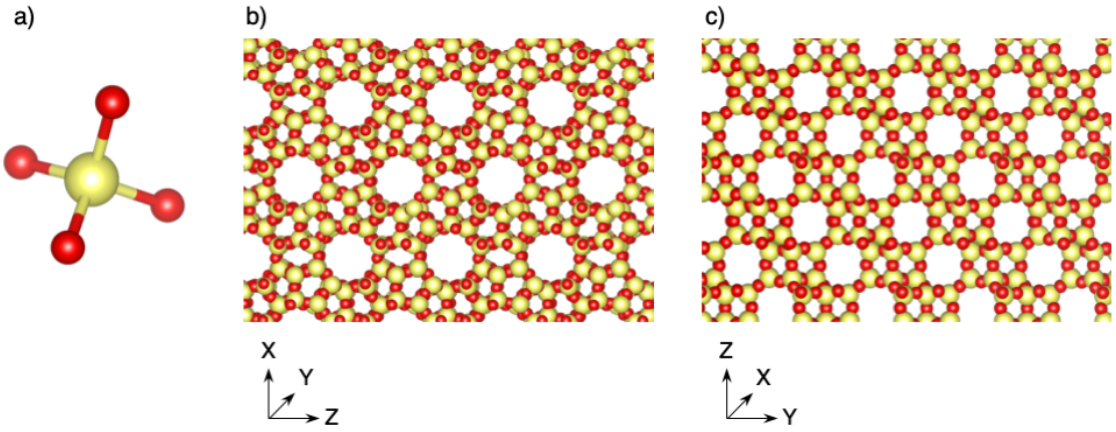


**Figure 1.3:** Tetrahedral $SiO_4$ unit (a) and structures of the MFI (b) and CHA (c) framework. The MFI framework is depicted with view along the ten-ring channels (view along y-axis) and the CHA framework is depicted with view along the eight-ring channels (view along x-axis). Color code: Silicon – yellow, oxygen – red.

In zeolite frameworks, silicon atoms can be substituted with aluminum atoms leading to aluminosilicates. The typical range for Si/Al ratios varies for different zeolites. Considering the CHA framework for instance, the typical range for the Si/Al ratio is between 10 and 54.[19] The maximum fraction of aluminum is 50 % according to Löwenstein's rule.[20] Aluminum substitution requires introducing a cation for charge neutrality, creating a so-called active site. When incorporating a proton as the cation, a Brønsted acid site (see Fig. 1.4) is formed which plays a central role within acidic zeolite catalysts. In the CHA and MFI frameworks, this kind of substitution yields the H-SSZ-13 and H-ZSM-5 zeolites, respectively. While H-ZSM-5 is frequently utilized in industrial processes, H-SSZ-13 is often used for simulations due to its simple structure, reducing computational and modeling effort compared to other zeolites. In so-called aluminophosphate (AlPO) structures, the zeolite's silicon atoms are alternatingly replaced with phosphorus and aluminum atoms. The resulting structure is isoelectronic to the aforementioned aluminosilicate structure. Substituting a phosphor atom with a silicon atom and inserting a proton equivalently leads to Brønsted acid sites within silioaluminophosphate (SAPO) structures. The corresponding zeolite for the CHA framework is H-SAPO-34, which is also often utilized in industry.

[1] All illustrations of structures in this work were made with the Visualization for Electronic and Structural Analysis (VESTA) program.[18]

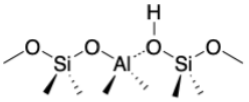


**Figure 1.4:** Brønsted acid site in zeolites.

The active site's centered atom (aluminum for aluminosilicates) has four adjacent oxygen atoms, which are generally not symmetrically equivalent. The acidity of the inserted proton depends on the oxygen atom it is bound to.[21] In addition, substitutions at different T-sites lead to different acid strengths within one zeolite.[21] Incorporating metals instead of protons yields Lewis acid sites.[22] Pure aluminosilicates can also contain Lewis acid sites. However, their structure is still under investigation, where many structural motifs like extra-framework alumina, framework-associated alumina, and external surface Lewis acid sites are discussed.[23,24]

Zeolites can be used for various applications.[25,26] Their special framework structure with specific pore and channel size leads to size and shape selectivity as well as to a large adsorption capacity. As the size selectivity limits the molecules which can pass through a zeolite, it can be used as a molecular sieve.[27] Furthermore, adsorption strengths vary for different molecules in a specific zeolite and also for a specific molecule in different zeolites, rendering them suitable for separation processes.[28] Therefore, zeolites are also discussed for carbon dioxide capturing.[29–31] Another broad application is to soften or purify water, where zeolites are used as ion exchangers.[28] Both Brønsted and Lewis acid sites in zeolites are utilized in heterogeneous catalysis. The catalytic behavior of zeolites can be controlled by many parameters like framework topology, crystal size, or acid site density.[6,13,32,33] These acid sites can catalyze, for example, cracking, isomerization, or alkylation reactions of hydrocarbons. This makes zeolites especially interesting for petrochemical industry and biomass upgrading,[5,6] including the production of acetone or isobutene from acetic acid[11,34–38] obtained from renewable resources.[39–42] In this context, an important catalytic utilization is methanol-to-X processes, where methanol is converted to olefins, gasoline, hydrocarbons, or aromatics.[6]

## 1.3 External Zeolite Surfaces

Due to diffusion limitations in the bulk of zeolites, considerable efforts have been undertaken to synthesize and utilize nano-sized,[43–46] hierarchical,[47–51] and two-dimensional[52–54] zeolites, which have decreased diffusion limitations and enhanced resistance towards catalyst deactivation[45,50,54]. These zeolites have large external surface areas, which facilitate access to the acidic sites in the zeolite bulk. Therefore, such surfaces gained increasing attention.[55–59] As shown in Fig. 1.5 for the (001) surface of the CHA structure, these areas are terminated by silanol groups[55,56].

When investigating reactions of these zeolites, acid sites located at their large external surfaces consequently need to be taken into account. However, computational chemistry mainly focused on the Brønsted acid site inside the zeolite bulk so far. Recently, the group of Chizallet drew attention to external surfaces and established structural models. Using DFT calculations, they found that Brønsted acid sites are stable and present at the (001) surface of H-BEA (Beta polymorph A)[57] and at the (100), (101), and (010) surfaces of H-ZSM-5[58]. Furthermore, they found a water-adsorbed surface site (with

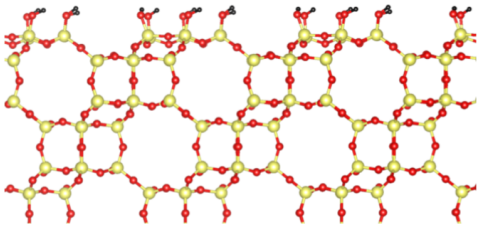

**Figure 1.5:** Structure of the (001) surface of the CHA structure. Color code: Silicon – yellow, oxygen – red, hydrogen – black.

an aluminum additionally bonded to three oxygen atoms of the zeolite) to be even more stable at the surface. At high temperatures, this water can be desorbed, leaving a threefold coordinated aluminum, which is Lewis acidic (see Fig. 1.6). Existence of this threefold coordinated aluminum in zeolites was also evidenced experimentally.[60–63] Thus, both Brønsted and Lewis acid sites exist at the external surface.

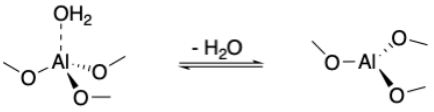


**Figure 1.6:** Water-adsorbed surface Lewis acid site with tetragonal structure and empty surface Lewis acid site with trigonal structure. The active site of the zeolite is depicted only.

While Lewis acid sites are believed to strongly influence catalytic performance, e.g., in hydrogenation,[64] hydrogen transfer between methanol and olefins,[65] or the methanol-to-propylene process,[66] their structure is still subject to ongoing discussions. Many proposals for so-called extra-framework aluminum have been made.[23,24] However, evidence for specific structures is scarce. Surface Lewis acid sites, in contrast, are well-defined and thus ideal models for computations.

## 1.4 Methanol-to-Olefins Processes

*This section is based on the introductory sections of* [Philipp Huber and Philipp N Plessow. A computational investigation of the decomposition of acetic acid in H-SSZ-13 and its role in the initiation of the MTO process. *Catal. Sci. Technol.*, 13(6):1905–1917, 2023.] *and* [Philipp Huber and Philipp N Plessow. The role of decarboxylation reactions during the initiation of the methanol-to-olefins process. *J. Catal.*, 428:115134, 2023.], *where I already summarized relevant aspects of the MTO process and its initiation mechanism.*

An important application of zeolites is the conversion of methanol to a wide range of hydrocarbons within so-called methanol-to-hydrocarbons (MTH) processes.[6,9] MTH processes can be tuned to mainly produce a certain kind of product. For instance, olefins, gasoline, and aromatics are generated in the respective MTO, MTG, and MTA processes. The required methanol can be obtained from either fossil raw materials, like natural gas, crude oil, and coal, or renewable resources, such as biomass[5,67–69] and carbon dioxide[70,71] from industry or air. Thus, MTH processes can be run sustainably and provide an

alternative to utilizing crude oil for the production of hydrocarbons. A large part of my research targets the MTO process, which is schematically shown in Fig. 1.7.

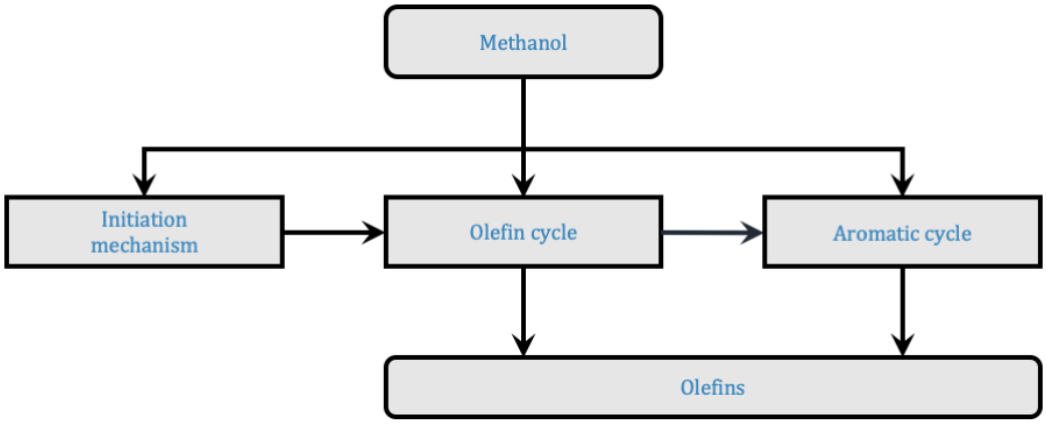


**Figure 1.7:** Scheme of the MTO process.

Typical reaction conditions are approximately 400 °C and atmospheric pressure.[9] Starting the MTO process requires a certain initial concentration of olefins. While impurities can serve as origin of these initial olefins,[72–74] zeolites catalyze the direct conversion of methanol to olefins via carbon-carbon coupling.[75] Subsequently, more olefins are formed autocatalytically by methylation and cracking in the olefin cycle.[6,76–80] Aromatics are also produced, which has two important consequences. First, they act as co-catalyst in the aromatic cycle[6,81–83] comprising the side-chain[84–88] and the paring mechanism[89–93], in which methylation and cracking of aromatic compounds also yield olefins. Second, the bulky aromatic compounds can clog the zeolite's pores, leading to deactivation of the catalyst.[94–96] The aromatics and olefins form the so-called hydrocarbon pool, whereby the co-catalyzed olefin production is called hydrocarbon pool mechanisms.[97] The mechanisms of the MTO process are not yet fully understood and still subject to current investigations. Unravelling these mechanisms is complicated since identifying intermediates experimentally is difficult due to their high reactivity and low pressure.[98] Additionally, these mechanism are heavily intertwined.

This work focuses in particular on the initiation mechanism of the MTO process, i.e., the direct formation of olefins starting from methanol. Many proposals for this mechanism have been made,[9,99,100] with the most important ones listed below (schematically shown in Fig. 1.8):

- **Oxonium ylide mechanism:** Dimethylether (DME) and a surface methoxy species (SMS), which are easily formed from methanol, react to a trimethyl oxonium.[101] After deprotonation, an ylide is formed. Intermolecular reaction with another SMS yields a methylethyloxonium ion, which subsequently reacts to DME and ethene. Intramolecular reaction of the ylide via Stevens-type rearrangement yield ethylmethyl ether. Decomposition releases methanol and ethene. Further studies found this mechanism to be unlikely due to high barriers.[102,103]

- **Carbene mechanism:** Methanol molecules react to carbenes ($CH_2$), which further react with methanol, with DME, or polymerize forming the first carbon-carbon bond.[104–106] Mechanisms involving carbenes also have high barriers.[102]

- **Radical mechanism:** Surface radicals initiate the formation of methyl and methylmethoxy radicals, which couple to olefins.[107] Experiments using radical scavengers suggested this mechanism to be unlikely.[108,109]
- **Methane-formaldehyde mechanism:** Formaldehyde (FA) and methane react to ethanol, which afterwards dehydrates to ethene.[102] Similar mechanisms involve the coupling of a carbonium cation or methoxymethyl cation with methanol or DME.[110,111]
- **Ketene-mediated (or CO-catalyzed) mechanism:** SMS couples with CO to ketene, which subsequently can be methylated and decarbonylated to olefins.[112,113]

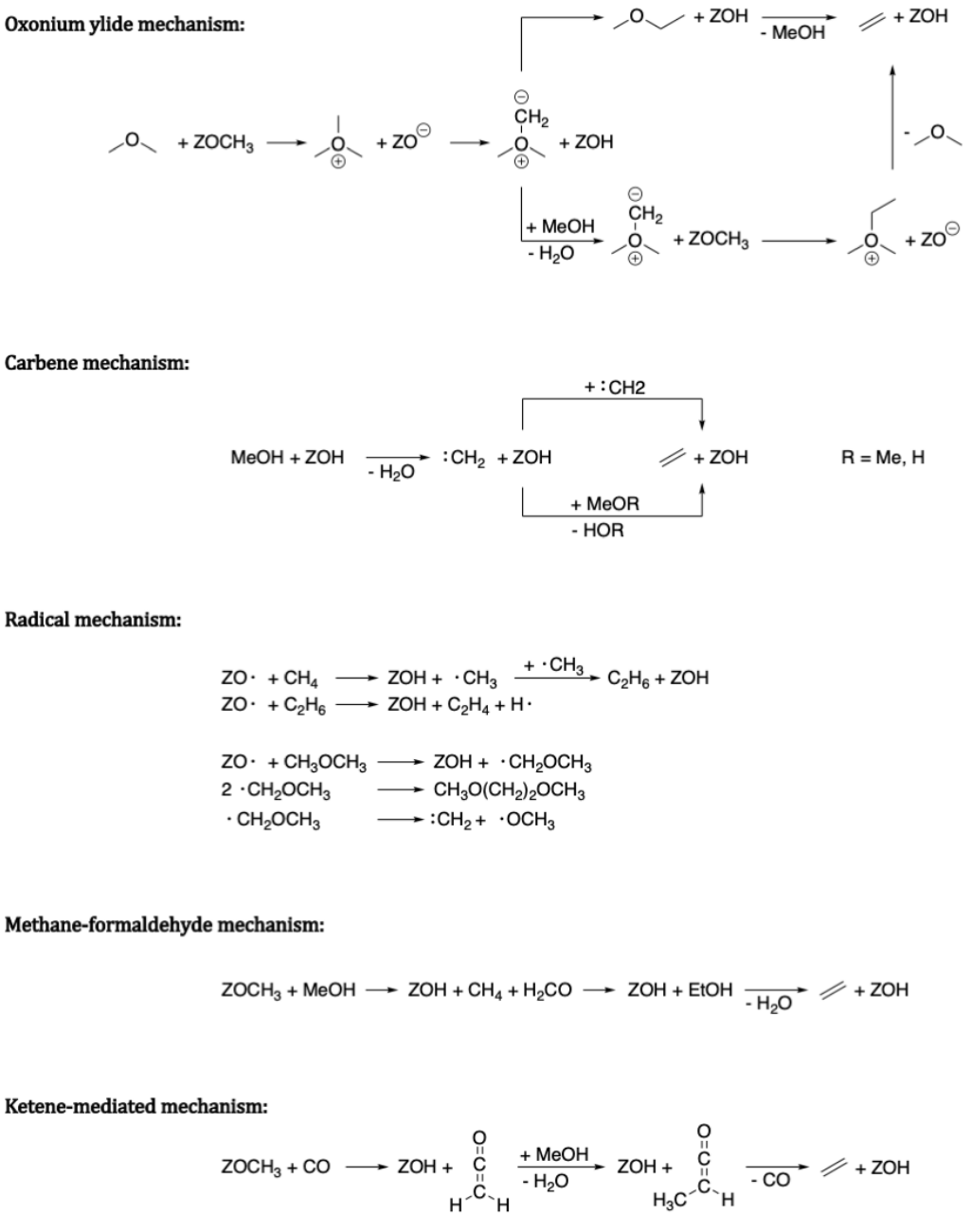


**Figure 1.8:** Schematic overview of proposed initiation mechanisms for the MTO process.

As demonstrated extensively for the H-SSZ-13 zeolite by calculating reaction barriers and examining kinetic simulations, the ketene mechanism has been shown to initiate the MTO process.[113,114] This study was further extended by calculating reaction barriers for H-ZSM-5, H-BEA, and H-SAPO-34, where the ketene mechanism also appeared to be reasonable.[115] This mechanism as computed in these studies[113–115] is sketched in Fig. 1.9.

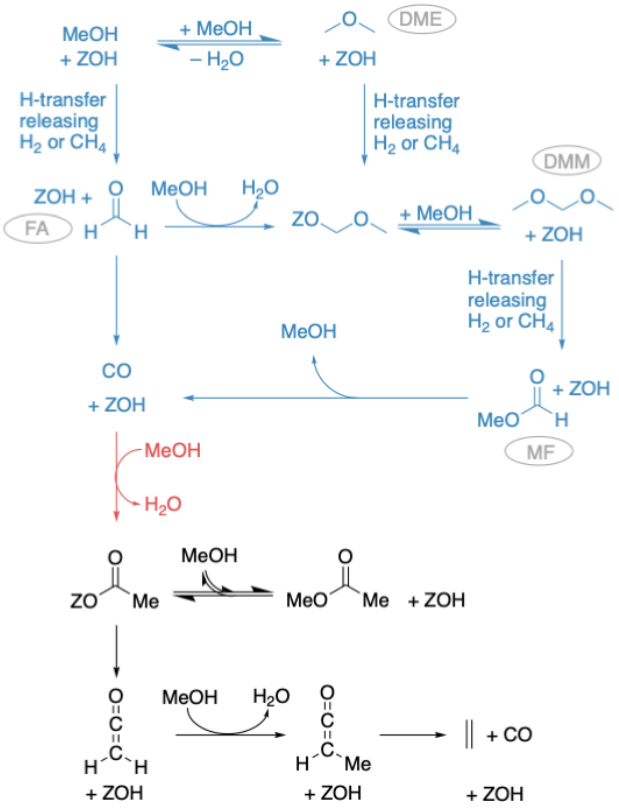


**Figure 1.9:** Simplified scheme of the ketene mechanism as computed by Plessow et al.[113] Color code: Blue – formation of CO, red – C-C coupling via CO and SMS, black – decarbonylation to ethene. Abbreviations referring to adsorbates are printed grey. Hydrogen transfer reactions between adsorbates and the zeolite's proton yield $H_2$, or methylation agents like MeOH, DME, and SMS yield $CH_4$. Reproduced from Ref. 116 with permission of Elsevier.

When methanol enters the zeolite, it is first dehydrated to an SMS and DME. The formation of SMS in zeolites, its reactivity as well as its function in the MTO process have already been extensively studied.[75,117] This also holds for DME, which is formed in a step-wise (also called dissociative) or a concerted (also called associative) mechanism.[118–125] These reactions are discussed in more detail in chapter 3. FA can be formed through hydrogen transfer (HT) reactions between methanol and an SMS or the zeolite's acidic proton, yielding $CH_4$ or $H_2$ as side products. DME can also react via HT with SMS or the zeolite's acidic proton to a surface methylmethoxy (SMM) group and $CH_4$ or $H_2$, respectively. SMM can dissociate from the zeolite's acid site leaving an SMS by releasing FA. Additionally, SMM can also react with methanol to dimethoxymethane (DMM). CO, which acts as co-catalyst in the following mechanism, can be formed via two routes. Either it can be formed from dehydrogenation of FA via HT transfer with the zeolite's acidic proton, or DMM reacts through HT transfer between SMS or the zeolite's acidic proton to methylformate (MF) by releasing $CH_4$ or $H_2$. Afterwards, MF decomposes to methanol and CO. The first carbon-carbon bond is then formed by reaction of CO and an SMS, yielding a zeolite

surface acetate. This acetate can further react with methanol to methyl acetate, a stable intermediate during this mechanism. The acetate can also dissociate from the zeolite forming a ketene, which yields methylketene after methylation by an SMS. The first olefin, ethene, is produced after decarbonylation of methylketene. In Fig. 1.9, only methylation up to methylketene is shown. However, methylketene can be further methylated, yielding propene and isobutene after corresponding decarbonylation reactions.
The detection of many important intermediates of the ketene mechanism further supports its relevance for the initiation of the MTO process. SMS[126–132], DME[133,134], FA[135–138], and CO[136,139,140] are commonly accepted intermediates, which have been observed in many investigations of the MTO process. Methane was also identified in many studies.[135–137,141,142]. Formation of hydrogen is proven[143] but found to be insignificant,[135] indicating that the HT reaction described above more likely involves SMS instead of the zeolite's proton. DMM has been detected in H-SAPO-34, while the existence of SMM could not be confirmed so far.[144] In the same study, at least methanediol, the hydrated species of SMM, was observed, along with zeolite surface acetate and methyl acetate which were also found in H-ZSM-5.[143] Methyl acetate was also detected in H-ZSM-5 using methylal as feed instead of methanol.[145] Zeolite surface acetate was observed in H-MOR using SMS and CO as feed.[146] Methyl formate and zeolite surface acetate were detected after syngas conversion in the bifunctional catalyst $ZnAlO_x$/H-ZSM-5. Even though detection of ketene is more complicated due to its high reactivity, it was found in H-MOR using either $CH_3COCl$[147] or a mixture of CO, DME, and $D_2O$[148] as feed, where it was detected as $H_2DCOO$. In H-ZSM-5, ketene and methylketene were detected at 250 °C and 360 °C, respectively, from conversion of methyl acetate.[149]
In addition to the aforementioned species, carbon dioxide was also identified during the initiation of the MTO process.[97,130,136,137,139,140,142] This formation of $CO_2$ cannot be explained by existing mechanism and is part of my research discussed in section 5.

## 1.5 Scope of this Thesis

Against this backdrop, the relevance of different kinds of active sites in zeolites is still not clear. The proposed motifs of Lewis acid sites remain speculative and reaction mechanisms taking place in zeolites are only partly revealed. While experimental elucidation is often difficult, computational chemistry can help to gain a comprehensive understanding of these processes required for optimization of catalysis.

The relevance of different reaction paths proceeding at specific acid sites can be determined by comparing the heights of their free energy barriers. In this dissertation, I study acid site motifs and reaction mechanisms in acidic zeolites theoretically. In chapter 2, a detailed description of the methods I used is provided. Structures were optimized with periodic density functional theory (DFT). The resulting energies were adjusted by adding a correction term derived from ab-initio computations for cluster models at the CCSD(T) level of theory, which yields highly accurate energy values. Gibbs free energies were calculated using the ideal gas approximation for gaseous states and by considering a partial Hessian for vibrational modes of adsorbed structures. These free energies were used to calculate barriers and reaction rate constants, which were further utilized in kinetic batch reactor simulations. In chapter 3, I investigate Lewis and Brønsted acid site motifs located at the surface of the H-SSZ-13 zeolite. The stability of surface facets and different locations of these acid site motifs are discussed. After establishing a valid model for surface acid sites, their reactivity was investigated by comparing Gibbs free energy

barriers. The dehydration of methanol to DME was used as a probe reaction, which is an important reaction during the MTO process and similar to other reactions in zeolites. In chapter 4, I study the conversion of acetic acid in H-SSZ-13 comprising the ketonic decarboxylation to acetone, subsequent aldol self-condensation of acetone to mesityl oxide, and finally dehydration to isobutene. I determined a reaction network, which is discussed in terms of Gibbs free energy barriers and in terms of a kinetic simulation. In chapter 5, I contribute to a better understanding of the initiation mechanism of the MTO process by discussing several pathways releasing $CO_2$ during the direct formation of olefins. Mainly, the H-SSZ-13 zeolite is discussed by evaluating Gibbs free energy barriers and kinetic simulations. In addition, key reaction steps for the H-SAPO-34 and H-ZSM-5 zeolite are investigated.
Thus, in this dissertation, I deepen the understanding of acid site motifs in zeolites and the reactivity of zeolites with a special focus on dehydration and decarboxylation reactions.

# 2

# Computational Methods

From nuclei and electrons to atoms and further to molecules, solids, and surfaces; physical observables of these systems can be described with quantum mechanics. An important observable is the energy, whereby the energy gradient can be used to optimize chemical structures. From optimized structures, adsorption energies or energy barriers of chemical reactions can be obtained. Adding thermodynamic contributions, free energies are calculated, which are required to compute equilibrium and rate constants for constant pressures and temperatures. Complicated chemical processes can then be simulated with kinetic models. Thus, quantum mechanical concepts can help us understanding and optimizing chemical processes. Since these calculations are not feasible by single computing workstations, high-performance computing clusters are utilized. By connecting many central processor units to computing clusters, time-demanding computations can be speed up by parallelized execution.
In this chapter, the quantum mechanical concepts and further methods are introduced, which are used to compute energies of chemical structures. I will discuss the modeling for structures and how free energies can be calculated from thermodynamic approaches. Furthermore, I will describe how transition state structures are optimized to obtain free energy barriers and how these barriers can be used for kinetic simulations. In section 2.5, I summarize computational details eventually used for these thesis.

## 2.1 Electronic Structure Methods

Two main approaches exist for the computation of energies for given structures: wave-function based methods and density functional theory (DFT). Both methods will be explained in this section, whereby some topics discussed for wave-function based methods are also relevant for DFT.

### 2.1.1 Wave Function Methods

#### Electronic Schrödinger Equation

In quantum mechanics, particles, including electrons and nuclei, can be described with wave functions. These can be determined by solving the Schrödinger equation. For this work, the time-independent non-relativistic form of the Schrödinger equation is sufficient. When solving the Schrödinger equation, the Born-Oppenheimer approximation is usually applied. The key assumption for this approximation is that the nuclei are moving much slower than electrons. Accordingly, the nuclei can be considered to move in an averaged potential of electrons and the electrons are moving in a constant potential of fixed nuclei. This enables the separation of the wave functions of electrons and of nuclei. An electronic wave function $\Psi(\mathbf{r}, \mathbf{R})$ depending on the electronic coordinates $\mathbf{r}$ can be obtained from the electronic Schrödinger equation (Eq. 2.1), including the nuclei positions $\mathbf{R}$ parametrically only for the nucleus-nucleus and nucleus-electron interactions. Energetic and entropic contributions arising from the movement of nuclei are discussed in section 2.3. In computational chemistry the electronic energy and wave function are needed in a first step. How these can be obtained is described below in more detail.

$$\hat{H}\Psi = E\Psi \tag{2.1}$$

$$\hat{H} = \hat{T}_e + \hat{V}_{ee} + \hat{V}_{ne} + \hat{V}_{nn} \tag{2.2}$$

$$\hat{T}_e = -\sum_{i}^{N} \frac{\hbar^2}{2m_e}\nabla_i^2 = -\sum_{i}^{N} \frac{1}{2}\nabla_i^2 \tag{2.3}$$

$$\hat{V}_{ee} = \sum_{i}^{N}\sum_{j>i}^{N} \frac{e^2}{4\pi\epsilon_0|\mathbf{r}_i - \mathbf{r}_j|} = \sum_{i}^{N}\sum_{j>i}^{N} \frac{1}{|\mathbf{r}_i - \mathbf{r}_j|} \tag{2.4}$$

$$\hat{V}_{ne} = -\sum_{i}^{N}\sum_{a}^{N_n} \frac{Z_a e^2}{4\pi\epsilon_0|\mathbf{R}_a - \mathbf{r}_i|} = -\sum_{i}^{N}\sum_{a}^{N_n} \frac{Z_a}{|\mathbf{R}_a - \mathbf{r}_i|} \tag{2.5}$$

$$\hat{V}_{nn} = \sum_{a}^{N_n}\sum_{b>a}^{N_n} \frac{Z_a Z_b e^2}{4\pi\epsilon_0|\mathbf{R}_a - \mathbf{R}_b|} = \sum_{a}^{N_n}\sum_{b>a}^{N_n} \frac{Z_a Z_b}{|\mathbf{R}_a - \mathbf{R}_b|} \tag{2.6}$$

The electronic Hamilton operator $\hat{H}$ comprises the kinetic energy operator of electrons, labeled $\hat{T}_e$, and the potential energy operators for electron-electron, electron-nucleus, and nucleus-nucleus interactions, labeled $\hat{V}_{ee}$, $\hat{V}_{ne}$, and $\hat{V}_{nn}$, respectively. The expressions for these operators are given in Eqs. 2.3-2.6. The operators are also written in atomic units, where $\hbar = m_e = 4\pi\epsilon_0 = e = 1$. $N$ and $N_n$ correspond to the number of electrons and nuclei, $m_e$ is the electron mass, $\boldsymbol{r_i}$ and $\boldsymbol{R_a}$ are the electron and nucleus coordinates, $\epsilon_0$ is the vacuum permittivity, $e$ is the electron charge, and $Z_a$ are the charges of nuclei.

**Slater Determinant**

A many-electron wave function $\Psi(\mathbf{x}_1, \mathbf{x}_2, ...\mathbf{x}_N)$ can be built from single-electron wave functions, so-called orbitals. Electrons posses the quantum mechanic property of a spin ($\alpha$ or $\beta$), which is included in orthonormalized spin orbitals $\phi(\mathbf{x})$. These spin orbitals depend on the electronic coordinates, which are products of a spatial and a spin function (Eq. 2.7).

$$\phi_i(\mathbf{x}) = \begin{cases} \varphi_i(\mathbf{r})\alpha(\omega) \\ \varphi_i(\mathbf{r})\beta(\omega) \end{cases} \tag{2.7}$$

For the many-electron wave function $\Psi$, Slater determinants $\Phi$ are used to fulfill the Pauli principle, which states that the wave function has to be antisymmetric with respect to exchange of any two electron coordinates. The Slater determinant then is constructed from $n$ orthonormal spin orbitals $\phi$ for $N$ electrons (Eq. 2.8). Thus, the wave function is described as a linear combination of all possibilities regarding permutations of electrons within the orbitals. In the Hartree-Fock method (see below), a single Slater determinant $\Phi$ is used only in the Schrödinger equation.

$$\Phi\left(\mathbf{x}_1, \mathbf{x}_2, ..., \mathbf{x}_N\right) = \frac{1}{\sqrt{N!}} \begin{vmatrix} \phi_1(\mathbf{x}_1) & \phi_2(\mathbf{x}_1) & \cdots & \phi_n(\mathbf{x}_1) \\ \phi_1(\mathbf{x}_2) & \phi_2(\mathbf{x}_2) & \cdots & \phi_n(\mathbf{x}_2) \\ \vdots & \vdots & \ddots & \vdots \\ \phi_1(\mathbf{x}_N) & \phi_2(\mathbf{x}_N) & \cdots & \phi_n(\mathbf{x}_N) \end{vmatrix} \tag{2.8}$$

The energy expectation value for a normalized wave function can be obtained from Eq. 2.9. The one-electron operator $\hat{h}_i$ yields non-zero elements $h_i$ only for diagonal elements due to orthogonality of the orbitals $\phi$. (Eq. 2.10). For the electron-electron interaction, two contributions are received. First, the Coulomb integral $K_{ij}$, which describes classical repulsion between two charge distribution (Eq. 2.11). Second, the the exchange integral $J_{ij}$, which has no classical equivalent (Eq. 2.12). Integrals over more than two electrons does not exist because of orthogonality of the orbitals.

$$E = \frac{\langle\Phi|\hat{H}|\Phi\rangle}{\langle\Phi|\Phi\rangle} = \langle\Phi|\hat{H}|\Phi\rangle = \sum_i^N h_i + \sum_i^N \sum_{j>i}^N \left(J_{ij} - K_{ij}\right) + V_{nn} \tag{2.9}$$

$$\begin{aligned} h_i &= \langle\phi_i\left(\mathbf{x}_k\right)|\hat{h}_i\left(\mathbf{x}_k\right)|\phi_i\left(\mathbf{x}_k\right)\rangle \\ &= \langle\phi_i\left(\mathbf{x}_k\right)|\frac{1}{2}\nabla_k^2 - \sum_a^M \frac{Z_a}{|\mathbf{R}_a - \mathbf{r}_k|}|\phi_i\left(\mathbf{x}_k\right)\rangle \end{aligned} \tag{2.10}$$

$$\begin{aligned} J_{ij} &= \langle\phi_i\left(\mathbf{x}_k\right)\phi_j\left(\mathbf{x}_l\right)|\hat{J}_i\left(\mathbf{x}_k\right)|\phi_i\left(\mathbf{x}_k\right)\phi_j\left(\mathbf{x}_l\right)\rangle \\ &= \langle\phi_i\left(\mathbf{x}_k\right)\phi_j\left(\mathbf{x}_l\right)|\mathbf{r}_{kl}^{-1}|\phi_i\left(\mathbf{x}_k\right)\phi_j\left(\mathbf{x}_l\right)\rangle \end{aligned} \tag{2.11}$$

$$\begin{aligned} K_{ij} &= \langle\phi_i\left(\mathbf{x}_k\right)\phi_j\left(\mathbf{x}_l\right)|\hat{K}_i\left(\mathbf{x}_k\right)|\phi_i\left(\mathbf{x}_k\right)\phi_j\left(\mathbf{x}_l\right)\rangle \\ &= \langle\phi_i\left(\mathbf{x}_k\right)\phi_j\left(\mathbf{x}_l\right)|\mathbf{r}_{kl}^{-1}|\phi_j\left(\mathbf{x}_k\right)\phi_i\left(\mathbf{x}_l\right)\rangle \end{aligned} \tag{2.12}$$

**Hartree-Fock Method**

The ground state energy (Eq. 2.9) of a system can now be obtained by variation of the wave function (Eq. 2.13). The variational principle states that the true ground state energy for the exact ground state wave function is lower or equal than the optimized energy and thus true ground state energy can be approximated by minimization.

$$\langle \delta\Phi | \hat{H} | \Phi \rangle = 0 \tag{2.13}$$

For the variation, the Lagrange method is used with the constraint of orthonormal orbitals. Minimization leads to the Hartree-Fock (HF) equations with the Fock operator $\hat{F}_i$. An unitary transformation of the HF equations leads to the canonical Fock expression with the canonical spin orbitals $\phi'$ and corresponding spin orbital energies $\epsilon_i$ (elements of the Lagrangian multiplier, which is a diagonal matrix).

$$\hat{F}_i(\mathbf{x}_k) |\phi'_i\rangle = \epsilon_i |\phi'_j\rangle \tag{2.14}$$

$$\hat{F}_i(\mathbf{x}_k) = \hat{h}_i(\mathbf{x}_k) + \sum_j^N \left( \hat{J}_j(\mathbf{x}_k) - \hat{K}_j(\mathbf{x}_k) \right) \tag{2.15}$$

For solving a specific HF equation, knowledge of all other orbitals is required, since Coulomb and exchange contributions depend on the other electrons. Therefore, the HF equations can only be solved iteratively, whereby the electron-electron interaction is based on the current orbitals. This procedure requires the assumption that each electron is moving in a static potential of all other electrons (mean field approximation). The molecular orbitals can be expanded in a set of atomic basis functions. For molecules, Gaussian functions are commonly used. Molecular spin orbitals are then expressed as a linear combination of atomic spin orbitals $\chi$ (LCAO) with a basis size $M$ using expansion coefficients $C_{\alpha i}$ (Eq. 2.16). The basis functions are generally not orthonormal.

$$\phi_i = \sum_\alpha^M C_{\alpha i} \chi_\alpha \tag{2.16}$$

The HF equations (Eq. 2.14) are then rewritten in terms of the LCAO yielding the Roothaan-Hall equation, below shown in matrix notation (after multiplication with $\langle \phi'_i |$) with the Fock matrix $\mathbf{F}$ and the overlap matrix $\mathbf{S}$.

$$\mathbf{FC} = \mathbf{SC}\boldsymbol{\epsilon} \tag{2.17}$$

$$F_{\alpha\beta} = \langle \chi_\alpha | \hat{F} | \chi_\beta \rangle \tag{2.18}$$

$$S_{\alpha\beta} = \langle \chi_\alpha | \chi_\beta \rangle \tag{2.19}$$

The one-electron contributions of the Fock matrix can be described by a core-Hamiltonian matrix $\mathbf{H}$, a density matrix $\mathbf{D}$, and the two-electron integrals $\mathbf{G}$ (Eqs. 2.20-2.23).

$$\mathbf{F} = \mathbf{H} + \mathbf{G} \tag{2.20}$$

$$H_{\alpha\beta} = \langle \chi_\alpha(\mathbf{x}_k) | \hat{h}(\mathbf{x}_k) | \chi_\beta(\mathbf{x}_k) \rangle \tag{2.21}$$

$$G_{\alpha\beta} = \sum_{\gamma\delta} D_{\gamma\delta} \left( \langle \chi_\alpha(\mathbf{x}_k)\chi_\gamma(\mathbf{x}_l) | \mathbf{r}_{kl}^{-1} | \chi_\beta(\mathbf{x}_k)\chi_\delta(\mathbf{x}_l) \rangle - \langle \chi_\alpha(\mathbf{x}_k)\chi_\gamma(\mathbf{x}_l) | \mathbf{r}_{kl}^{-1} | \chi_\delta(\mathbf{x}_k)\chi_\beta(\mathbf{x}_l) \rangle \right) \tag{2.22}$$

$$D_{\gamma\delta} = \sum_{j}^{N} C_{\gamma j} C_{\delta j} \tag{2.23}$$

The Roothaan-Hall equation have to be solved to obtain the energy. For this, the Fock matrix is diagonalized which requires all values for $C_{\alpha i}$. Thus, these equations also have to be solved iteratively by the self-consistent-field procedure starting with an initial guess for $C_{\alpha i}$ leading to an initial density matrix. Afterwards a Fock matrix is formed from **H**, **G**, and **D**. Then the Fock matrix is diagonalized to obtain new values for $C_{\alpha i}$. These coefficients are used to calculate a new density matrix, which initiates the next iteration and the procedure is repeated until convergence is reached. The final expression for the electronic energy is given by Eq. 2.24.

$$E = \sum_{\alpha\beta}^{M} D_{\alpha\beta} h_{\alpha\beta} + \frac{1}{2} \sum_{\alpha\beta\gamma\delta}^{M} \left( D_{\alpha\beta} D_{\gamma\delta} - D_{\alpha\delta} D_{\gamma\beta} \right) \langle \chi_\alpha \chi_\gamma | \mathbf{r}_{kl}^{-1} | \chi_\beta \chi_\delta \rangle + V_{nn} \tag{2.24}$$

The energy only depends on occupied molecular orbitals while also $M-N$ unoccupied (virtual) molecular orbitals are calculated. For the one-electron contributions $M^2$ and for the two-electron contributions $M^4$ integrals have to be evaluated. Thus, the time effort of the HF method scales in principle with the fourth power with respect to the size of the basis set (in practice, pre-screening of integrals can reduce the scaling). However, the accuracy of this procedure increases with the size of the basis set. The computational effort can be reduced to $M^3$ by the resolution of the identity approximation using an auxiliary basis set (**P** and **Q**). Instead of four-index integrals, three-index integrals are calculated.[150–152]

$$(\chi_\alpha \chi_\gamma | \chi_\beta \chi_\delta) \approx \sum_{PQ} (\chi_\alpha \chi_\gamma | \mathbf{P}) (\mathbf{P}|\mathbf{Q})^{-1} (\mathbf{Q} | \chi_\beta \chi_\delta) \tag{2.25}$$

When constructing a Slater determinant, the spin orbitals can be treated in a restricted and an unrestricted fashion. In the restricted Hartee-Fock (RHF) method the spatial function is the same for both $\alpha$ and $\beta$ spin while these are in the unrestricted Hartee-Fock (UHF) method not the same. For this work, only the RHF method was applied using closed-shells only, i.e., all occupied molecular orbitals are doubly occupied.

### Post-Hartree-Fock Methods

The HF method treats the electron-electron interaction via an average potential by the mean field approximation. If a large basis is used, this method can cover up to 99 % of the total energy. However, when describing chemical properties within a suitable accuracy, the missing percent is required, which

is called electron correlation energy. The electron correlation can be accounted for by use of more than one Slater-determinant.

$$\Psi = a_0\Phi_{\mathrm{HF}} + \sum_{n=1} a_n\Phi_n \tag{2.26}$$

For $\Phi_n$, excited Slater determinants are used. Two correlation methods will be discussed in the following; the coupled cluster theory and the Møller-Plesset perturbation theory [153].

**Møller Plesset perturbation theory**: In the Møller Plesset (MP) perturbation theory, the HF solution is assumed to be close to the real quantum chemical system. Thus, many-body perturbation theory can be used to calculate the difference between the HF and the real solution. For this, the Hamilton operator consists of two parts, which are a reference $\hat{H}_0$ and a perturbation $\hat{H}'$ part (Eq. 2.27). A parameter $\lambda$ is used to describe the degree of perturbation. For the reference, the HF Hamilton operator is used.

$$\hat{H}_{\mathrm{MP}} = \hat{H}_0 + \lambda\hat{H}' \tag{2.27}$$

$$\hat{H}' = \hat{V}_{ee} - 2\langle\hat{V}_{ee}\rangle \tag{2.28}$$

The perturbed Schrödinger equation depicted in Eq. 2.29 yields the perturbed ground state energy $W$ (Eq. 2.30) from the wave function $\Psi$ (Eq. 2.31).

$$\hat{H}_{\mathrm{MP}}\Psi = W\Psi \tag{2.29}$$

$$W = \lambda^0 W_0 + \lambda^1 W_1 + \lambda^2 W_2 + \cdots + \lambda^n W_n \tag{2.30}$$

$$\Psi = \lambda^0\Psi_0 + \lambda^1\Psi_1 + \lambda^2\Psi_2 + \cdots + \lambda^n\Psi_n \tag{2.31}$$

The indices $n$ for $W$ and $\Psi$ correspond to the order of correction. The wave function is intermediately normalized with $\langle\Psi_0|\Psi_0\rangle = 1$ and $\langle\Psi_0|\Psi_{i\neq 0}\rangle = 0$. Inserting Eq. 2.30 and 2.31 in Eq. 2.29 and separating the terms with $\lambda^n$ for different $n$, which can be solved separately, yields Eq. 2.32. The energy values $W_n$ are then obtained by projection of Eq. 2.32 to $\langle\Psi_0|$, while the energy $W_n$ depends on the previous solution $\Psi_{n-1}$ (Eq. 2.33).

$$\hat{H}_0\,|\Psi_n\rangle + \hat{H}'\,|\Psi_{n-1}\rangle = \sum_{i=0}^{n} W_i\,|\Psi_{n-i}\rangle \tag{2.32}$$

$$W_n = \langle\Psi_0|\hat{H}'|\Psi_{n-1}\rangle \tag{2.33}$$

In the Rayleigh-Schrödinger perturbation theory, $\Psi_n$ can be expanded in the basis of the known unperturbed wave functions $\Phi$ (Eq. 2.34). The coefficient $c_i$ can be determined by inserting Eq. 2.34 to Eq. 2.32 and projection to $\langle\Psi_{i\neq 0}|$.

$$\Psi_n = \sum_i c_i\Phi_i \tag{2.34}$$

Using for $\hat{H}_0$ the Fock operator yields the sum over molecule orbital energies for $W_0$, which counts electron-electron energy $V_{ee}$ twice. For $W_1$, the value for $-V_{ee}$ is obtained, thus the first-order correction yields the HF result. When including the correlations energy, at least second order MP (MP2) has to be considered. The formula for the second order correction is shown in Eq. 2.35, where $a$ and $b$ are indices for virtual orbitals of the excited state.

$$W_2 = \sum_{i<j}^{occ} \sum_{a<b}^{vir} \frac{\langle \phi_i \phi_j | \phi_a \phi_b \rangle - \langle \phi_i \phi_j | \phi_b \phi_a \rangle}{\epsilon_a + \epsilon_b - \epsilon_i - \epsilon_j} \tag{2.35}$$

Here, the denominator is the energy difference of the ground state end the doubly excited state. MP2 in principle scales with $M^5$ due to transformation of integrals from atomic to molecular orbitals and thus provides a relative efficient method to account for the correlation energy with a typically percentage of $80 - 90$.[154]

**Coupled Cluster Theory**: While MP methods compute the correlation energy by an approximate inclusion of excited states through perturbation theory, the coupled cluster (CC) method in principle includes all excitation levels explicitly. Excited states can be obtained through the excitation operator $\hat{T}$ (Eq. 2.36) from the HF reference state. Equations 2.37 and 2.38 show the single and double excitations with the amplitudes $t$.

$$\hat{T} = \hat{T}_1 + \hat{T}_2 + \cdots + \hat{T}_N \tag{2.36}$$

$$\hat{T}_1 \Phi_0 = \sum_{i}^{occ} \sum_{a}^{vir} t_i^a \Phi_i^a \tag{2.37}$$

$$\hat{T}_2 \Phi_0 = \sum_{i<j}^{occ} \sum_{a<b}^{vir} t_{ij}^{ab} \Phi_{ij}^{ab} \tag{2.38}$$

In the CC method, the exponential operator (Eq. 2.39) is used to compute the CC energy $E_{\mathrm{CC}}$ as shown in Eq. 2.40. This leads to connected (like $\hat{T}_2$) and disconnected (like $\hat{T}_1^2$) terms. The amplitudes can be obtained by projecting the Schrödinger equation on excited states.

$$e^{\hat{T}} = \sum_{k=0}^{\infty} \frac{1}{k!} \hat{T}^k \tag{2.39}$$

$$\begin{aligned} E_{CC} &= \langle \Phi_0 | \hat{H} e^{\hat{T}} | \Phi_0 \rangle \\ &= E_0 + \sum_{i<j}^{occ} \sum_{a<b}^{vir} t_{ij}^{ab} \left( t_{ij}^{ab} + t_i^a t_j^b - t_i^b t_j^a \right) \left( \langle \phi_i \phi_j | \phi_a \phi_b \rangle - \langle \phi_i \phi_j | \phi_b \phi_a \rangle \right) \end{aligned} \tag{2.40}$$

Since inclusion of the complete excitation operator $\hat{T}$ is computational not feasible, it is truncated to excitations of a certain degree. CCSD for example, includes singles and doubles excitations only, i.e. $\hat{T} = \hat{T}_1 + \hat{T}_2$, which has a computational effort that scales with $M^6$. Higher excitations can be included via perturbation theory. For instance, CCSD(T) includes contributions of triples with MP4 resulting in a scaling of $M^7$. The CCSD(T) method is often called the "gold-standard of quantum chemistry", because it is able to achieve chemical accuracy of $\sim 4\,\mathrm{kJ/mol}$ by still being computational feasible for many chemical systems. For CC, the domain based local pair natural orbital (DLPNO) method can be applied to reduce computational effort.[155] For this, the correlation energy of pairs of electrons is calculated within a truncated domain. Since electron correlation decreases with the distance of electrons, the computational effort can be reduced by largely maintaining accuracy.

### 2.1.2 Density Functional Theory

Density functional theory (DFT) provides an alternative to wave-function based methods for modeling chemical systems. It was established by Hohenberg and Kohn, who proved that the electronic ground state is determined completely by the electron density $\rho$. While the HF method depends on 3N variables, $\rho$ only depends on three variables leading to efficient computing. Within the Born-Oppenheimer approximation, the electronic energy $E_{\mathrm{DFT}}[\rho]$ is the sum of the kinetic energy of electrons $T[\rho]$, attraction between nuclei and electrons $E_{ne}[\rho]$, and electron-electron repulsion $E_{ee}[\rho]$. $E_{ee}$ can be divided to two terms, the Coulomb ($J[\rho]$) and the exchange ($K[\rho]$) part. However, orbital free density functional methods yield poor results for most systems due to a insufficient description of $T[\rho]$. The Kohn-Sham theory therefore introduces orbitals again to calculate the kinetic energy $T_S[\rho]$ from a Slater determinant. In doing so, DFT has the same computational scaling as the HF method, but usually reaches more accurate results, depending on the specific density functional. For this, an electron density is defined from a set of auxiliary one-electron functions (Eq. 2.41). The expression for the DFT energy is given in Eq. 2.42.

$$\rho = \sum_{i}^{N} |\phi_i|^2 \tag{2.41}$$

$$E_{\mathrm{DFT}}[\rho] = T_{\mathrm{S}}[\rho] + E_{ne}[\rho] + J[\rho] + E_{\mathrm{XC}}[\rho] \tag{2.42}$$

The exchange-correlation energy functional $E_{\mathrm{XC}}[\rho]$ accounts for the difference between the kinetic energy of non-interacting and interacting electrons (kinetic correlation energy) as well as for the difference of the full electron-electron interaction and the Coulomb energy. Comparison between the exact energy and the DFT energy yields the corresponding expression for $E_{\mathrm{XC}}[\rho]$ (Eq. 2.43).

$$E_{XC}[\rho] = (T[\rho] - T_S[\rho]) + (E_{ee}[\rho] - J[\rho]) \tag{2.43}$$

Finding an appropriate functional $E_{XC}[\rho]$ is the key problem in DFT. Different approaches exist to define the exchange-correlation functional. With increasing complexity and computational effort, these approaches achieve higher positions in the so-called Jacob's ladder, which is a hierarchical construction to illustrate the level of theory. At the bottom rung is the local density approximation (LDA), where

the functional treats the density as a uniform electron gas. The next step is including derivatives for the density in the generalized gradient approximation (GGA) methods. Higher rungs are the meta-GGA methods, which include higher order derivatives and the hybrid methods, which include HF exchange energy. In this work, I mainly employed the PBE functional[156], which is GGA functional parameterized to fulfill energetically-relevant physical conditions. Dispersion energy arising from London forces are poorly described by PBE,[157] but can be treated by adding a dispersion correction to the DFT energy. For PBE-D3, a dispersion correction, comprising two-body and three-body interactions, is considered, which efficiently includes dispersion energies up to a deviation of 10 % compared to CCSD(T).[158] When eventually computing the DFT energy, it can be determined with the self-consistent-field procedure via Lagrangian multiplier as described for the HF method. For this, Kohn-Sham equations (Eq. 2.44) are solved, which is equivalent to solving HF equations.

$$\mathbf{h}_{KS}\mathbf{C} = \mathbf{SC}\boldsymbol{\epsilon} \tag{2.44}$$

$$\hat{h}_{KS} = \frac{1}{2}\nabla^2 + \hat{V}_{eff}\left(\mathbf{r}\right) \tag{2.45}$$

$$\hat{V}_{eff}\left(\mathbf{r}\right) = \hat{V}_{ne}\left(\mathbf{r}\right) + \int \frac{\rho\left(\mathbf{r}'\right)}{|\mathbf{r}-\mathbf{r}'|} + \hat{V}_{XC}\left(\mathbf{r}\right) \tag{2.46}$$

The effective potential $\hat{V}_{eff}\left(\mathbf{r}\right)$ in the Kohn-Sham operator $\hat{h}_{KS}$ comprises the nuclei-electron potential, the Coulomb repulsion from electrons, and the exchange-correlation potential. Functionals depending on the density are evaluated numerically on grid points, which have to be chosen dense enough to achieve accurate results.

## 2.2 Structure Models

The methods described so far in section 2.1.1 can be applied for molecules using Gaussian basis sets. When computing periodic systems, some further considerations have to be taken into account. In section 2.2.1, I will discuss modeling for periodic systems with plane waves. In section 2.2.2, I will describe a hierarchical model approach, which improves periodic DFT energies by adding a correction term obtained from high-level methods at cluster models.

### 2.2.1 Periodic Systems

Periodic systems, like crystals and surfaces, obtain the property of translational symmetry. These systems are described by a unit cell, which fulfills the periodic boundary conditions (PBC). Translation of the unit cell builds the infinite periodic structure. In accordance to the PBC, Bloch's theorem states that an one-electron wave function is defined by a periodic function $u_{\mathbf{k}}\left(\mathbf{r}\right)$ and a plane wave $exp(i\mathbf{kr})$ (Eq. 2.47).

$$\psi_{nk}(\mathbf{r}) = u_{nk}(\mathbf{r})\, e^{i\mathbf{kr}} \tag{2.47}$$

$\mathbf{k}$ is the wave vector and $\mathbf{r}$ are the electronic coordinates. $u_{\mathbf{k}}(\mathbf{r})$ is represented by lattice translation with the lattice vector $\mathbf{R}$ (Eq. 2.48).

$$u_{nk}(\mathbf{r} + \mathbf{R}) = u_{nk}(\mathbf{r}) \tag{2.48}$$

$u_{\mathbf{k}}(\mathbf{r})$ can be expanded in plane waves using the reciprocal lattice vector $\mathbf{G}$ and expansion coefficients $c_{lnk}$ (Eq. 2.49).

$$u_{nk}(\mathbf{r})\, e^{i\mathbf{kr}} = \sum_{\mathbf{G}} c_{nk} e^{i(\mathbf{k}+\mathbf{G})\mathbf{r}} \tag{2.49}$$

The expansion coefficients $c_{lnk}$ can then be optimized during the self-consistent field procedure and an electronic energy is calculated from the optimized plane-waves. In practice, only plane waves up to a certain threshold (cut-off) are included as shown in Eq. 2.50.

$$E_{\mathrm{cut-off}} = \frac{\hbar^2}{2m}|\mathbf{G}_{max}|^2 \qquad \text{with} \qquad |\mathbf{G}+\mathbf{k}| < \mathbf{G}_{max} \tag{2.50}$$

Physical observables, like the density and energy, are then calculated by treating $\psi_{\mathbf{k}}(\mathbf{r})$ on a mesh of k-points (k-point sampling) instead of integrating over the reciprocal space. For the k-point sampling, only the first Brillouin zone (BZ) is considered, which is the most compact presentation of a cell within the reciprocal space. The Γ-point approximation only uses the center of the BZ for the k-point sampling, which is sufficient for large unit cells, as present for zeolites. The description of the region close to nuclei is difficult using plane wave due to high curvatures of the electron wave function requiring a high value for $E_{\mathrm{cut-off}}$ in computations. The projector augmented wave approach[159] addresses this problem by defining augmentation spheres around nuclei. The all electron wave function is then constructed from a linearly transformation of pseudo wave functions. The wave function is described inside the spheres by partial waves and outside the spheres (interstitial region) by smooth plane waves.

### 2.2.2 Hierarchical Models

One important ingredient of this work is computing reliable free energy barriers to discuss the relevance of reaction mechanisms in zeolites. Structures were optimized using periodic DFT with the PBE-D3 functional. However, DFT energies fail to describe these energy barriers,[160,161] while applying high-level methods is computational not feasible for periodic systems. The group of Sauer established a methodology using hierarchical cluster models to deal with that problem.[160,162–165] For this approach, a cluster model is cut out from the structure optimized through DFT with periodic boundary conditions (PBC). The cluster model has to be small enough to be computational feasible with high-level methods, but large enough to represent the former structure. The cluster model should include the active site, adsorbates (if present), and a part of the framework surrounding the adsorbates. Si-F or Si-H groups can

be used to saturate the terminations of the cutout, whereby I used Si-H groups with fixed bond lengths of 148.9 pm. The cluster models for H-SSZ-13 and H-ZSM-5, which I used in this work, are shown in Fig. 2.1 Energies from high-level methods are then obtained for these cluster models with fixed structure as single-point energies. The final cluster-model corrected energy is calculated from the DFT energy by adding a correction term, which is the difference between the high-level method obtained from the cluster model and the low-level (here DFT) method obtained from the cluster model, as shown in Eq. 2.51.

$$E = E_{\mathrm{DFT}}^{\mathrm{PBC}} + E_{\mathrm{high-level}}^{\mathrm{CM}} - E_{\mathrm{DFT}}^{\mathrm{CM}} \tag{2.51}$$

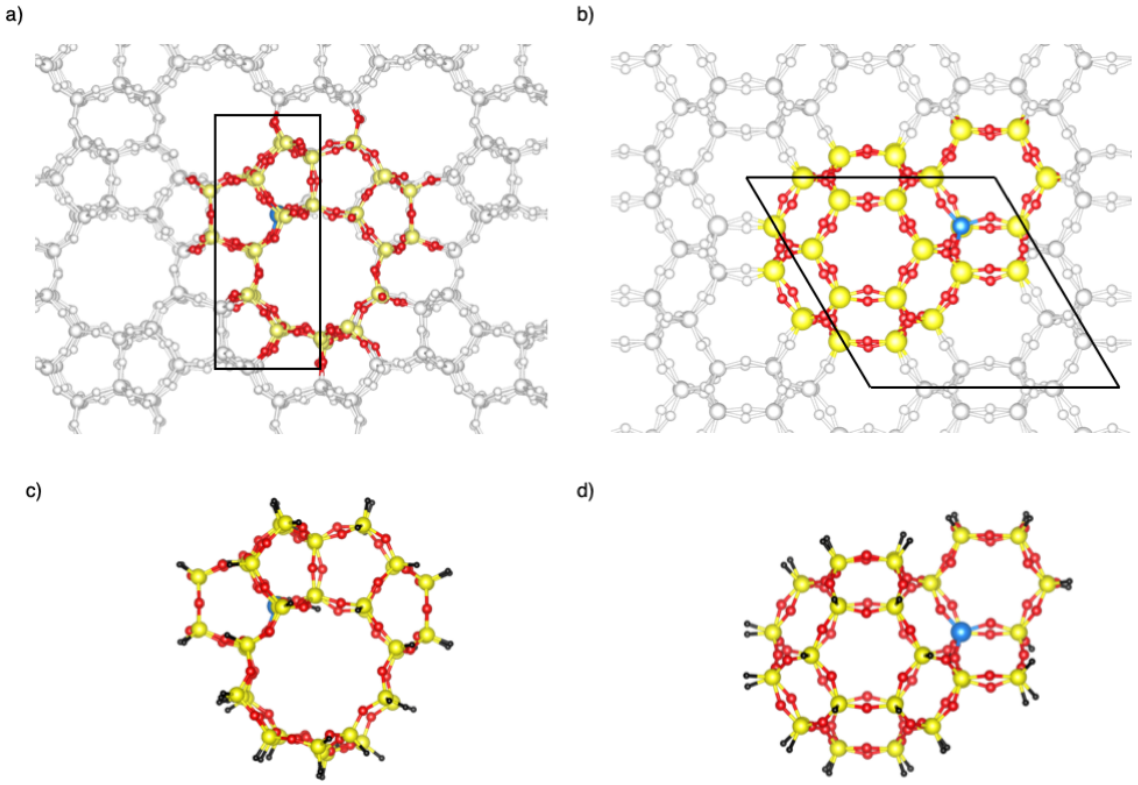


**Figure 2.1:** Periodic and cluster-model structures of H-ZSM-5 a) and c) and of H-SSZ-13 b) and d). The cutouts from the periodic structures for the cluster models are depicted in color and the unit cells are indicated with black frames. Color code: Silicon – yellow, oxygen – red, aluminum – blue –, remaining framework – grey. Reproduced from Ref. 125 with permission from Elsevier.

This approach was further investigated by usage of a second tier of cluster models,[160] and by utilization of different levels of theory.[113,166] In principal this approach is able to achieve chemical accuracy ($\pm 4$ kJ/mol) for energy barriers ,[160] while periodic DFT energy barriers using the PBE-D3 functional were found to be lower than the cluster-model corrected energy barriers by a mean absolute error of more than 40 kJ/mol.[166]

## 2.3 Thermodynamics

Investigation of chemical reactions requires thermodynamic contributions in addition to the energy from electronic structure theory leading to free energies. For the calculation of free energies, the partition

functions are needed. The partition function of the canonical ensemble $q$ of an ideal gas can be written as shown in Eq. 2.52, when neglecting the contribution of excited electronic states, which are not considered in my thesis. Thus, $q$ only comprises rotational, translational, and vibrational degrees of freedom (Eq. 2.53-2.56), which can be deduced within the rigid rotator, free translator, and harmonic oscillator approximation, respectively. Note, the partition function for rotation distinguishes for linear and non-linear molecules.

$$q = q_{\text{rot}} \cdot q_{\text{trans}} \cdot q_{\text{vib}} \tag{2.52}$$

$$q_{\text{rot}}^{\text{linear}} = \frac{8\pi^2 k_b T}{h^2} \tag{2.53}$$

$$q_{\text{rot}}^{\text{non-linear}} = \left(\frac{8\pi^2 k_B T}{h^2}\right)^{3/2} \cdot \frac{\left(I_A I_B I_C \pi\right)^{1/2}}{\sigma} \tag{2.54}$$

$$q_{\text{trans}} = \frac{V\left(2\pi M k_B T\right)^{3/2}}{h^3} \tag{2.55}$$

$$q_{\text{vib}} = \Pi_i \frac{exp\left(-h\nu_i/2k_B T\right)}{1 - exp\left(-h\nu_i/k_B T\right)} \tag{2.56}$$

$k_b$ is the Boltzmann constant, $h$ is the Plank constant, $T$ is the temperature, $M$ is the molecular mass, $V$ is the volume of 1 mol ideal gas, $\sigma$ is the symmetry number, $I$ are moments of inertia, and $\nu$ are the vibration frequencies. The entropy $S$ (Eq. 2.57) and heat capacity $C_p$ (Eq. 2.58) are calculated from the molar partition function $Q$ (Eq. 2.59).

$$S\left(T,p\right) = -k_B ln(Q) - \frac{1}{T}\frac{\partial ln(Q)}{\partial(1/(K_B T))} - k_B ln\left(\frac{p}{p^\circ}\right) \tag{2.57}$$

$$C_p\left(T,p\right) = -k_B T^2 \frac{\partial^2 ln\left(Q\right)}{\partial^2 T} + k_B \tag{2.58}$$

$$Q = \frac{q_A^N}{N_A!} \tag{2.59}$$

$N_A$ is the Avogadro constant. With these relations, the enthalpy $H$ (Eq.. 2.60) and Gibbs free energy $G$ (Eq. 2.61) can be calculated with additionally using the electronic energy $E$ and the zero-point vibration energy $E_{\text{ZPVE}}$.

$$H\left(T\right) = E + E_{\text{ZPVE}} + \int_0^T C_p dT \tag{2.60}$$

$$G\left(T,p\right) = H\left(T\right) - TS\left(T,p\right) \tag{2.61}$$

For adsorbed molecules and solids, rotational and translational degrees of freedom are assumed to be negligible. The internal energy $U$ (Eq. 2.62) of such systems therefore only considers the harmonic vibrations for the parturition function. The Helmholtz free energy $F$ (Eq. 2.63) deduced from $U$ approximately can be equated with $G$.

$$U(T) = E + E_{ZPVE} + k_B T^2 \frac{\partial ln(Q)}{\partial T} \tag{2.62}$$

$$F(T) = U(T) - TS(T) \approx G(T, p) \tag{2.63}$$

## 2.4 Kinetics

Transition state theory enables the calculation of a reaction constant. For this, a potential energy surface (PES) is separated in an educt and a product region separated by the transition state separatrix, which has one dimension less than regions of the PES. Several assumptions are made by still maintaining an accurate description of the transition state with a representative rate constant. The states of the reactants in the PES can be described with a Boltzmann distribution. Classical concepts are used for the treatment of the rate constant, thus quantum tunneling through a barrier is neglected, which is a reasonable approximation at high temperatures. It is assumed that all educts reaching the transition state, will pass through it to the products without recrossing. For the harmonic transition state theory, the transition state of the reaction corresponds to the first order saddle point, which has the lowest possible energy between educts and products. Since transition states are located at this saddle point, they have one negative hessian eigenvalue leading to one imaginary frequency. Additionally, the regions of the PES around the reactant and the transition state are assumed to be harmonic and can thus be represented by a Taylor expansion. Considering these assumptions, the reaction constant $k$ can be expressed as the Eyring equation (Eq. 2.64).

$$k = \frac{k_b T}{h} exp\left(\frac{-\Delta G^{\ddagger}}{k_b T}\right) \tag{2.64}$$

$k_b$ is the Boltzmann constant, $h$ is the Plank constant, $T$ is the temperature, and $\Delta G^{\ddagger}$ is the free energy barrier, The free energy barrier is the free energy difference between the transition state structure and the reactant structure. The search of transition states structures, is more complicated than the optimization of local minima for reactants. For reactants, structures have to be relaxed step-wise downhill in the PES. For transition states, structures are moved uphill in the PES with respect to the reaction coordinates and downhill with respect to all other degrees of freedom. Since the reaction coordinate is not obvious, transition state optimization is challenging.

Four methods were used in this work for transition state searches and will be discussed in more detail. A simple method to get an estimate for the reaction path and the position of a transition state on the PES is a constraint optimization. The reaction coordinate can be written as internal coordinates corresponding to bond lengths. Optimizing several states (points at the PES) along the reaction coordinate with fixed bond lengths yields a one dimensional path within the PES. The maximum point corresponds approximately to the transition state. The Automated relaxed potential energy surface scans (ARPESS) method[167] enables the computation of transition states by scanning along the reaction coordinate in a more systematic way. The reaction coordinate is written as a linear combination $a$ of fixed bond lengths $b_i$ with the weighting $w_i$ (see Eq. 2.65).

$$a = \sum_i w_i \cdot b_i \tag{2.65}$$

This method requires an initial guess for the transition state. A constraint geometry optimization is then carried out to maximize the electronic energy with respect to $a$ and to minimize all other coordinates. The nudged energy band (NEB) method[168,169] requires states for educts and products. States (images) between educts and products are created and connected via a spring interaction emulating an elastic band. The minimum energy path (MEP) along these states is optimized including an approximate transition state located at the maximum of the MEP. The dimer method[170] requires an initial guess for the transition state structure. Next, two close states (dimer) of the PES are created, for example by a short distortion of the imaginary frequency of the initial guess. This dimer is then moved uphill in the PES along the lowest imaginary frequency.

After finding a transition state with the above discussed methods, it was reoptimized it with the ARPESS method and it was verified to have only one imaginary frequency. Distortion of the transition state along its imaginary frequency was checked to end up in the desired product and educt states.

Having eventually computed free energy barriers and reaction constants, microkinetic models can be constructed to simulate chemical processes. For this, reaction rates $r$ are calculated from reaction constants $k$.

$$r = k \cdot \Pi_i c_i^{a_i} \tag{2.66}$$

Here, $c_i$ are the concentrations of reactant species (alternatively e.g. pressures can be used) and $a_i$ are the corresponding reaction orders. In my investigations, I applied an ideal kinetic batch reactor model, which starts with an initial concentration of educts without continuous feed or outlet. An ideal mixing is assumed, which avoids temperature and concentration gradients. Additionally, interactions of reactants and the reactor are neglected. Since adsorption processes are usually much faster than chemical reactions, they generally have not been considered here explicitly. Starting with initial concentrations, a reaction mechanism, which consist of a network of elementary reaction steps, can be simulated by computing the distribution of the species considered in the reaction network for a time progress. For defined time steps, new reaction rates and new concentrations are iteratively computed.

## 2.5 Computational Details for this Thesis

In this sections, I provide a summary and additional details of the methodology eventually used in this work.

I investigated the H-SSZ-13, H-SAPO-34 and H-ZSM-5 zeotypes. For H-SSZ-13 and H-SAPO-34, which both crystallize in the CHA structure, the lattice constants are $a = b = 13.625\,\text{Å}$ and $c = 15.067\,\text{Å}$ for H-SSZ-13 and $a = b = 13.875\,\text{Å}$ and $c = 15.017\,\text{Å}$ for H-SAPO-34 as used in previous studies.[113,115] Corresponding Si/Al and (Al+P)/Si ratios are 35. The H-ZSM-5 zeolite crystallizing in the MFI framework has lattice constants of $a = 20.340\,\text{Å}$, $b = 19.988\,\text{Å}$, and $c = 13.492\,\text{Å}$ and a Si/Al ration of 96 as also used in previous work.[115] The H-ZSM-5 zeolite has twelve different T-sites, whereby I only considered the T12-site as active site. Zeotypes of the CHA framework in contrast, only have one unique T-site. Cluster models have 46 and 52 T-sites for the CHA and MFI framework, respectively. These are terminated by Si-H groups with a fixed bond length of 148.9 pm. In section 3, I investigate surface structures of

H-SSZ-13. I especially investigated two different structures of the (001) facet and one structure of the (101) facet. The Si/Al ratios for the (001) facets are 29 and 35. The Si/Al ratio for the (101) facet is 71. For the (001) termination, two BASs, labeled BAS1(001) and BAS2(001), and two LASs, labeled LAS1(001) and LAS2(001), were studied. For the (101) termination, two BASs, labeled BAS1(101) and BAS2(101), and one LAS, labeled LAS1(101), were studied. For BASs, four symmetrically different O-atoms exist within the active site. The numbering of these O-atoms is shown in Fig. 2.2 for bulk and surface structures of H-SSZ-13.

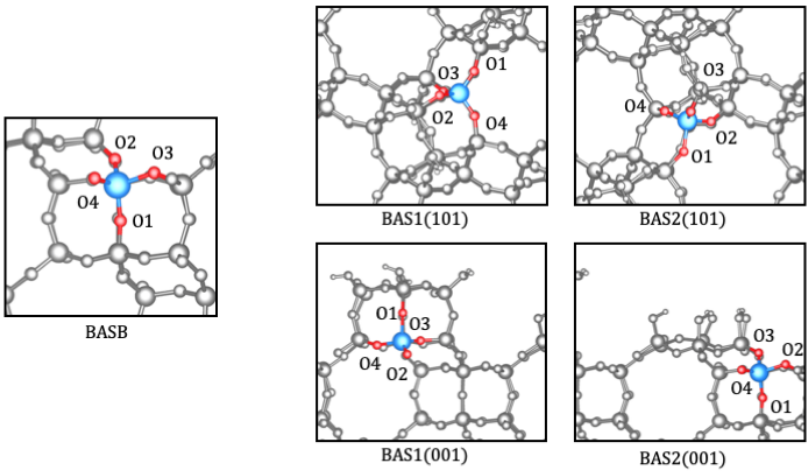


**Figure 2.2:** Numbering of oxygen atoms within the active site of the H-SSZ-13 bulk and surface structures. Color code: Silicon – yellow, oxygen – red, hydrogen – black, nitrogen – green, carbon – brown, remaining framework – grey. Reproduced from Ref.[125] with permission from ACS.

Further details to these surface structures can be found in the corresponding chapter. For the optimization of structures, periodic DFT with the PBE-D3[156,158] functional was used with a convergence criterion for atomic forces of 0.001 eV/Å. Gaseous structure were also optimized with periodic DFT, which is valid when adding enough vacuum space between the periodic repetitions of the molecules. These periodic calculations were carried out with the Vienna Ab Initio Simulation Package (VASP, version 5.4.1.)[159,171–174] applying an energy cut-off of $E_{\mathrm{cut-off}} = 400\,\mathrm{eV}$. Transition states were searched with several methods, but in the end optimized with the ARPESS[167] method. Transition state structures then were verified by having only one imaginary frequency leading to educt and product structures after distortion. For the calculation of free energies, the harmonic oscillator approximation has been used for vibrational degrees of freedom. A partial Hessian has been considered only for zeolite and zeolite adsorbed structures. This Hessian includes adsorbed molecules and the active site of the zeolite comprising the Al-atom and the four adjacent Si-O groups. For the SAPO structure, the active site comprises the Si-atom and adjacent Al-O groups. Small frequencies below 12 eV were changed to this value to avoid errors of the harmonic approximation.[77] Rotational and translational degrees of freedom additionally have been considered for gaseous structures within the rigid-rotator and free-translator approximation. Free energy are calculated at 1 bar and corrected by the cluster-model approach (cf. section 2.2.2) as shown in Eq. 2.67.

$$G = E^{\mathrm{PBC}}_{\mathrm{PBE-D3}} + \Delta E^{\mathrm{CM}} + \Delta G^{\mathrm{PBC}}_{\mathrm{harm}} \tag{2.67}$$

$\Delta G^{\mathrm{PBC}}_{\mathrm{harm}}$ is the Gibbs free energy contribution and the cluster-model correction $\Delta E^{\mathrm{CM}}$ is at the CCSD(T) level of theory (cf. Eq. 2.68). This cluster-model correction term comprises several single-point calculations. For the CCSD(T) energy $E_{\mathrm{CCSD(T)/DZ}}$, the cc-pVDZ basis set[175] was used. A correction term $\Delta E^{\mathrm{CM}}_{\mathrm{MP2/CBS}}$ has been added for a complete basis set (CBS) extrapolation. This CBS extrapolation was carried out separately for the HF and MP2 limit using the three-point exponential fit[176] with the cc-pVXZ (X=D,T,Q)[175] basis set and the $X^{-3}$ fit[177] with the cc-pVXZ (X=D,T) basis set, respectively. For the correlation methods, the DLPNO approximation[178,179] was employed. These HF, MP2, and CCSD(T) calculations were carried out with the ORCA program package,[180] whereby the "TightPNO" setting was employed for the correlation methods and the RIJCOSX approximation[150] with the X6 grid was used for the HF method. The DFT reference for the cluster-model correction $E^{\mathrm{CM}}_{\mathrm{PBE-D3}}$ was used with the def2-TZVPP basis set[181] and the RI approximation[151] as implemented in the Turbomole program package[182]. Eventually, $\Delta E^{\mathrm{CM}}$ has been calculated from Eq. 2.68 as also employed in other studies.[84,183,184]

$$\Delta E^{\mathrm{CM}} = \Delta E^{\mathrm{CM}}_{\mathrm{CCSD(T)/DZ}} + \Delta E^{\mathrm{CM}}_{\mathrm{MP2/CBS}} - E^{\mathrm{CM}}_{\mathrm{PBE-D3}} \tag{2.68}$$

If not mentioned otherwise, Gibbs free energies are calculated in this work as described in Eq. 2.67. Barriers are calculated within the energetic span model,[185] which considers the preceding most stable state as reference for a transition state.

# 3

# Surface Acid Sites of H-SSZ-13

*This chapter is based on* [Philipp Huber, Felix Studt, and Philipp N Plessow. Reactivity of Surface Lewis and Brønsted Acid Sites in Zeolite Catalysis: A Computational Case Study of DME Synthesis Using H-SSZ-13. *J. Phys. Chem. C*, 126(13):5896–5905, 2022].

As outlined in section 1.3, the reactivity of zeolite surfaces is a relevant topic for zeolites with small crystal sizes or hierarchical-structured zeolites, which both have large surface areas. Corresponding investigations were carried out sparsely so far but interest on surface acid sites increased recently.[59] Therefore, I established surface models of the SSZ-13 zeolite to investigate the surface reactivity, where I used the methanol dehydration as a probe reaction. Brønsted as well as Lewis acid sites exist on zeolite surfaces, thus in addition to further insight into zeolite surface reactivity, also further insights into Lewis acid sites in zeolites will be given. In section 3.1, I discuss the construction of purely-siliceous surface models and the stability of these surfaces. In section 3.2, I characterize surface acid sites and investigate their stability in comparison to the acid site located in the bulk of the zeolite. Finally, I look into the reactivity of surface acid sites in section 3.3. If not mentioned otherwise, periodic DFT energies corrected by ab initio calculations at cluster models at the CCSD(T) level of theory are used (cf. section 2.5).

## 3.1 Stability of Pure-Siliceous Surfaces

Before starting an investigation of H-SSZ-13 surface reactivity, appropriate models with reasonable surface orientation have to be found. The crystal structure and shape of H-SSZ-13 and other zeolites

crystallizing in the chabazite framework are already well-known. For instance, He et al. synthesized cubic SAPO-34 crystals with sizes of $1-2\,\mu$m.[47] Wu et al. obtained H-SSZ-13 crystals below 50 nm with cubic shape by investigating hierarchical structures.[51] For increasing crystal sizes, the cubic shape becomes more pronounced. They also synthesized conventional H-SSZ-13 with cubic crystals of $10-20\,\mu$m. Sommer et al. also obtained almost cubic-shaped H-SSZ-13 crystals of $10-15\,\mu$m.[186] The surface orientations of H-SSZ-13 are sparsely investigated, however, Ghorbarkar et al. synthesized an almost cubic H-SSZ-13 zeolite, where they explicitly assigned the (101) facet.[187]

For construction of the surfaces, repetitions to the unit cells have been applied and the structures were cut along the desired facet. Many terminations could be considered, however, the termination was chosen such that as few as possible Si-O-Si bonds had to be broken. In line with experimental findings,[55,56] broken Si-O-Si bonds were then saturated as silanol groups (SiOH). Following this procedure, modeling surface areas is equivalent with dividing the bulk structure in one direction by hydration. Finally, vacuum was added orthogonal to the surface areas to avoid interactions between periodic images. Usually, low-index facets are the most stable. Permutations of the numbers $\bar{1}$, 0, and 1 yield 13 different Miller indices, while for the CHA framework, some of these indices correspond to the same structure as shown in Table 3.1.

**Table 3.1:** Miller indices listed within a column are equivalent and correspond to the same CHA surface structure (with arbitrary labeling).

| Structure 1 | Structure 2 | Structure 3 | Structure 4 | Structure 5 | Structure 6 |
|---|---|---|---|---|---|
| (101) | (100) | (011) | (111) | (110) | (001) |
| ($\bar{1}$11) | (010) | (1$\bar{1}$1) | (11$\bar{1}$) | - | - |
| (0$\bar{1}$1) | ($\bar{1}$10) | ($\bar{1}$01) | - | - | - |

For selecting appropriate surface models, I further calculated the surface free energies $\gamma$ of non-equivalent surface structures presented above using Eq. 3.1. Saturation of surface terminations with silanol groups requires reaction with water molecules when surface structures are compared to the bulk reference. These water molecules have to be considered for the surface free energy.

$$\gamma = E_{\mathrm{Surf}} - 0.5 \cdot n\,(\mathrm{SiOH}) \cdot G\,(\mathrm{H_2O}) - n\,(T) \cdot E_T \tag{3.1}$$

$E_{\mathrm{Surf}}$ is the DFT energy from a surface structure, $n\,(\mathrm{SiOH})$ is the number of silanol groups, $G\,(\mathrm{H_2O})$ is the free energy of gaseous water considering only translational and rotational contributions (since vibrational contributions here have not been considered for the zeolite structure), $n\,(T)$ is the number of T-sites, and $E_T$ is the corresponding bulk energy per T-site. $E_T$ was obtained by extrapolating energies of surface structures with the same facet but different widths orthogonal to the surface versus their number of T-sites. The slope of the extrapolation then provides an energy per T-site independent of the surface termination compared to taking the energy per T-site from a single structure. Hence, a suitable bulk reference energy is obtained by the product of this single T-site energy and the number of T-site of a specific surface structure. Table 3.2 compares the surface area, number of silanol groups, and the number of T-sites for the different structures.

In Fig. 3.1a, the surface free energies versus temperature for the surface structures is shown. At $0\,K$, all surface structures have very similar surface free energies while for increasing temperature, surface free

**Table 3.2:** Surface area and number of silanol groups $n$ (SiOH) are given for the different facets. Both values corresponds to one surface only (bottom or top termination, which are equivalent) within a specific surface structure with two surfaces. Additionally, the number of T-sites for surface structures with different widths orthogonal to the surface termination are given.

| | (100) | (110) | (001) | (101) | (011) | (111) |
|---|---|---|---|---|---|---|
| Surface area in Å$^2$ | 205 | 356 | 161 | 261 | 261 | 390 |
| $n$ (SiOH) | 8 | 12 | 6 | 6 | 10 | 16 |
| $n(T)$ size 1 | 72 | 72 | 30 | 72 | 76 | 63 |
| $n(T)$ size 2 | 108 | 144 | 36 | 108 | 124 | 123 |
| $n(T)$ size 3 | 180 | 180 | 72 | 180 | 196 | 243 |
| $n(T)$ size 4 | - | - | 108 | - | - | - |

energies are spreading. These surface free energies mainly depend on the entropic contribution of water, which is needed for hydrating the Si-O-Si bonds to yield silanol groups. This dependency is visualized in Fig. 3.1b, where the surface free energies are plotted against the number of silanol groups per area, which show a linear behavior. Thus, surface free energies are increasing with increasing temperature due to increasing entropy. The (101) surface, which has the lowest value for silanol groups per area, becomes clearly the most stable structure with increasing temperature.

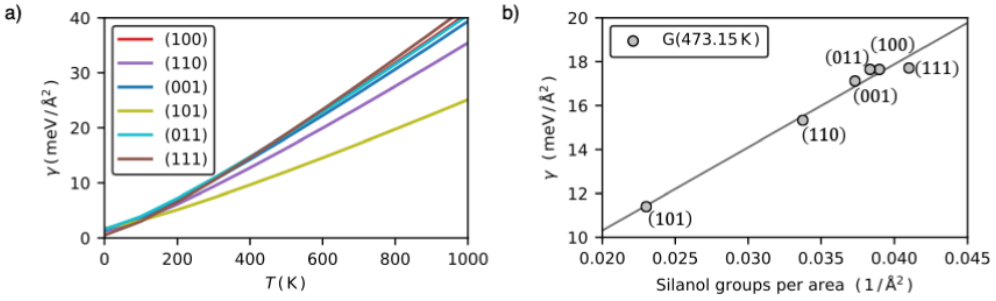


**Figure 3.1:** Surface free energies versus temperature a) and versus number of silanol groups per area at 200 °C b). Reproduced from Ref. 125 with permission from ACS.

A Wulff construction using the surface free energies for all presented facets is shown in Fig. 3.2a. The obtained crystal shape does not fit to experimental observed shapes. When neglecting the (110) and $(\bar{1}\bar{1}0)$ facets, an almost cubic crystal is obtained in accordance with experimental observed crystal shapes (Fig. 3.2b)[47,51,186,187] The surfaces are terminated with the (101) facet and equivalent facets. Since the (101) surface was also explicitly assigned in an experiment,[187] it is a reasonable surface structure to be further investigated. Additionally, I studied the (001) surface structure, which was already subject of theoretical studies,[188] to capture the influence of the specific surface orientation. Construction of a crystal shape using the (001), (110), and $(\bar{1}10)$ surface yield a rectangular cuboid shape (Fig. 3.2b), which was also observed experimentally.[189]

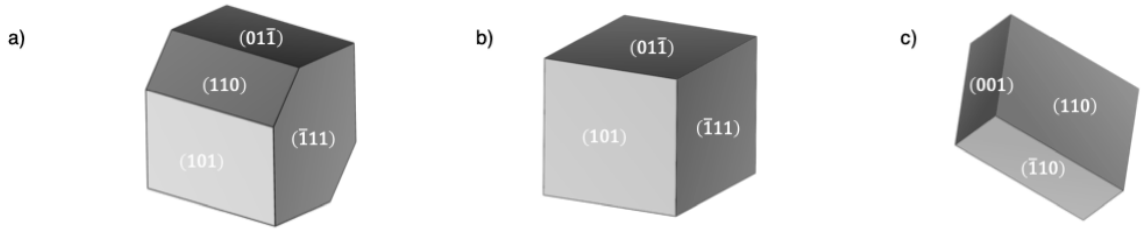


**Figure 3.2:** Constructions of crystal shapes considering different facets. Wulff construction using all low-index facets with permutations of the numbers $\bar{1}$, 0, and 1 a) and by neglecting the (110) and ($\bar{1}\bar{1}$0) facets b). Crystal construction by only considering the (001), (110), and ($\bar{1}$10) facets c). Reproduced from Ref. 125 with permission from ACS.

## 3.2 Stability of Zeolite Surface Acid Sites

In the previous section, the stability of purely-siliceous surface structures was investigated. Substitution of a silicon atom by an aluminum atom and inserting a proton yields an Brønsted acid site (BAS). Such a substitution at a silanol group yields a Lewis acid site (LAS) after desorption of water. Both acid sites will be discussed now for the (101) and (001) surface. The purely-siliceous structures are shown in Fig. 3.3, whereby periodic as well as cluster-models structures are given. The surface structures are shown in Fig. 3.3a-c and the bulk structure is shown in Fig. 3.3d. In the periodic bulk structure, two staggered double-six rings of CHA framework can be seen from a side view.[1] In the cluster-model structure of the bulk, two eight-membered rings of the CHA framework can be seen. The termination of the (101) surface leaves the double-six ring intact, while the eight-membered rings are cut in half orthogonal to the surface (cf. Fig. 3.3c). One LAS, labeled LAS1(101), and two BASs, labeled BAS1(101) and BAS2(101), were investigated for this structure. For the (001) surface, two terminations were considered. First, a termination leaving the double-six ring intact (cf. Fig. 3.3a) and second, a termination cutting the double-six ring in half (cf. Fig. 3.3b). The structure used for the second (001) terminations contains less T-sites and has a smaller width orthogonal to the surface termination compared to the structure used for the first (001) terminations. For the larger (001) structure, one LAS, labeled LAS1(001), and two BASs, labeled BAS1(001) and BAS2(001), weree investigated. For the smaller (001) structure, one LAS, labeled LAS2(001), was investigated. These surface acid sites will be compared to the BAS within the zeolite bulk (BASB). Fig. 3.4 shows possible location of the acid sites within a larger structure model for these surface orientations.

LASs and BASs can be characterized by infrared spectroscopy using probe molecules, which show specific differences for vibrations between adsorption on different acid sites.[56] For example, the 19b vibration mode of pyridine[190,191] is blue-shifted compared to the gas-phase vibration by $5 - 20\,\mathrm{cm}^{-1}$ for adsorption at LASs and by $90 - 100\,\mathrm{cm}^{-1}$ for adsorption at BASs.[192–194] Thus, a difference of $70 - 105\,\mathrm{cm}^{-1}$ exists between both types of acid sites. The different shifts result from different bonds to the acid sites. Pyridine forms a Lewis adduct at LASs and pyridinium ions at BASs as depicted in Fig. 3.5. I obtained blue-shifts of $16 - 17\mathrm{cm}^{-1}$ and $114 - 125\mathrm{cm}^{-1}$ for the 19b vibration of pyridine by adsorption at LASs and BASs, respectively (see Table 3.3). Hence, the computations for pyridine adsorption at BASs and LASs are in accordance with experiments, whereby blue-shifts for pyridine at LASs are slightly higher than in

[1] A double-six ring contains two rings (one above each other) of six Si-atoms in each case, while the side view in Fig. 3.3d reveals only six Si-atoms of each ring.

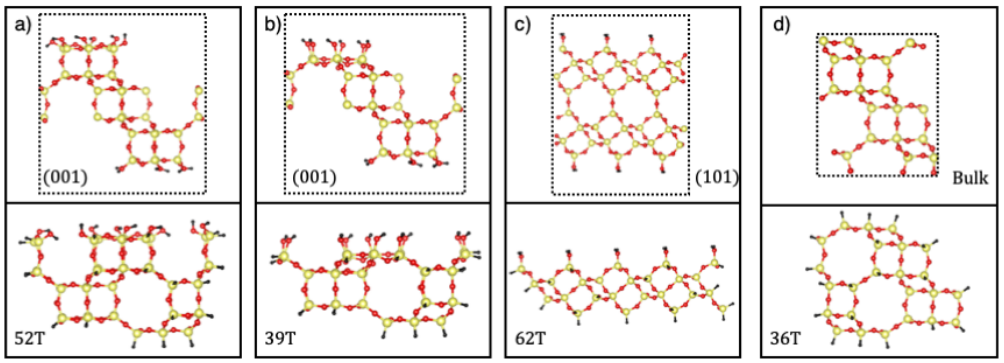


**Figure 3.3:** Purely-siliceous surface structure showing two structures for (001) orientation with different terminations a,b) and one structure for (001) orientation c). Purely-siliceous bulk structure d). Periodic as well as cluster-model structures are shown. The unit cell is approximately indicated. Color code: Silicon – yellow, oxygen – red, hydrogen – black.

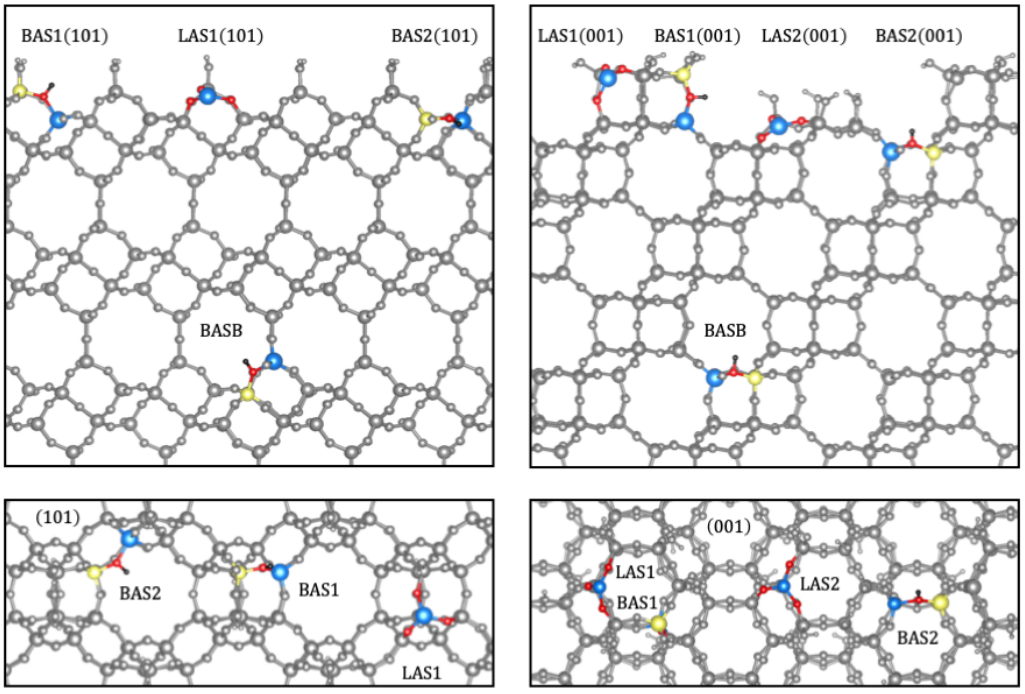


**Figure 3.4:** Overview of locations of the acid site within an extended zeolite surface model. Left: Side view (top) and top view (bottom) of the (101) surface. Right: Side view (top) and top view (bottom) of the (001) surface. Color code: Silicon – yellow, oxygen – red, hydrogen – black, remaining framework – grey. Reproduced from Ref. 125 with permission from ACS.

experiments. The difference for pyridine adsorption between both types of acid sites of $96 - 109\,\mathrm{cm}^{-1}$ quantitatively reproduce experimental results.

After having introduced acid sites to the surface structures, their stabilities will be analyzed. Since water is often present during zeolite synthesis and catalytic processes, its adsorption has to be taken into account when considering surface acid site stabilities. For BASs, adsorption at all four oxygen atom adjacent to the aluminum was computed. The numbering for these oxygen atoms is shown in Fig. 2.2 for surface structures as well as for the bulk structure. The stabilities were calculated with Eq. 3.2, where

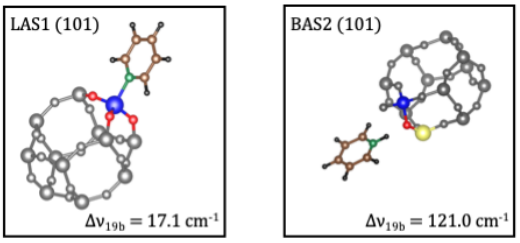


**Figure 3.5:** Adsorbed pyridine at LAS1(101) and BAS1(101). Only the double-six ring of the zeolite is shown. The shift of the 19b vibration referenced to gaseous pyridine is depicted. Color code: Silicon – yellow, oxygen – red, hydrogen – black, nitrogen – green, carbon – brown, remaining framework – grey. Reproduced from Ref. 125 with permission from ACS.

**Table 3.3:** Computed vibrational harmonic frequencies of the 19b mode computed for gaseous and adsorbed pyridine and corresponding vibrational shifts to gaseous pyridine. Reproduced from Ref. 125 with permission from ACS.

| System | 19b frequency ($cm^{-1}$) |
|---|---|
| gas phase | 1427.0 (exp: 1440) [195] |
| LAS1(101) | 1444.1 ($\Delta\nu = 17.1$) |
| LAS1(001) | 1444.8 ($\Delta\nu = 17.8$) |
| LAS2(101) | 1443.6 ($\Delta\nu = 16.6$) |
| BAS1(101) | 1552.2 ($\Delta\nu = 125.2$) |
| BAS2(101) | 1548.0 ($\Delta\nu = 121.0$) |
| BAS1(001) | 1552.0 ($\Delta\nu = 125.0$) |
| BAS2(001) | 1543.2 ($\Delta\nu = 116.2$) |
| BASB | 1540.8 ($\Delta\nu = 113.8$) |

an aluminum substitution in the bulk structure is compared to an aluminum substitution in the surface structure. For this, a state of a siliceous surface and an aluminum substituted bulk is compared to a state of an aluminum substituted surface and a siliceous bulk. The states used to calculate the stabilities of LASs are sketched in Fig. 3.6.

$$\Delta G = \left(G^{\mathrm{Al}}_{\mathrm{Surf}} + G^{\mathrm{Si}}_{\mathrm{Bulk}}\right) - \left(G^{\mathrm{Si}}_{\mathrm{Surf}} + G^{\mathrm{Al}}_{\mathrm{Bulk}}\right) + m \cdot G\left(\mathrm{H_2O}\right) \tag{3.2}$$

$G^{\mathrm{Al}}_{\mathrm{Surf}}$ and $G^{\mathrm{Al}}_{\mathrm{Bulk}}$ are the free energies of the clean or water-adsorbed (depending on which is more stable) aluminum-substituted acid sites for surface and bulk structures, respectively. $G^{\mathrm{Si}}_{\mathrm{Surf}}$ and $G^{\mathrm{Si}}_{\mathrm{Bulk}}$ are the free energies of the corresponding siliceous structures without aluminum substitution and without water adsorbed. $G\left(\mathrm{H_2O}\right)$ is the free energy of gaseous water and $m$ is the stoichiometric amount of water required to balance the reaction. Clean LASs have generally one more water present in the gas phase than clean BASs to fulfill the stoichiometry.

In Fig. 3.7, the stabilities of surface acid sites referenced to the BAS in the bulk are depicted as a function of the temperature. The surface BASs have similar stabilities as BASB. Up to temperatures of about 500 K, the water-adsorbed BASs are more stable than the water-desorbed states and the surface BASs differ by less than 6 kJ/mol to the BASB. After water desorption, the difference between BAS1(101) and BASB increases to 15 kJ/mol, while the other surface BASs still differ by less than 6 kJ/mol to the BASB. The corresponding mean absolute deviation of the maximum differences is 7 kJ/mol. Due to the additional water molecule in the gas phase for LASs, their stabilities depend stronger on the temperature. At low

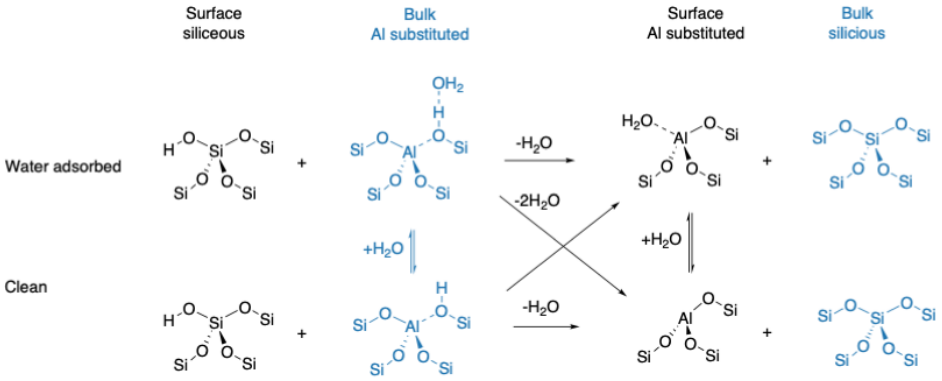


**Figure 3.6:** Calculated states for stability analysis of surface LASs considering the clean acid site as well as water adsorptions. Reproduced from Ref. 125 with permission from ACS.

temperatures, the LASs are significantly less stable than BASs. LAS2(101) becomes more stable at about 250 K and LAS1(101) and LAS1(001) become more stable at about 450 K than all BASs. Furthermore, water-adsorption is more favorable than the desorbed state up to about 900 K. Generally, LASs are more stable than BASs above temperatures of about 150 °C when considering water adsorption. Hence, formation of LASs is thermodynamically likely during zeolite synthesis where such temperatures[15] are often reached. This is in line with previous computational studies, which found surface LASs also to be reasonable in other zeolites.[57,58] The existence of LASs is not necessarily controlled by thermodynamics, but it is mainly controlled by the synthesis conditions, however, triangular LASs have been detected experimentally.[60–63]

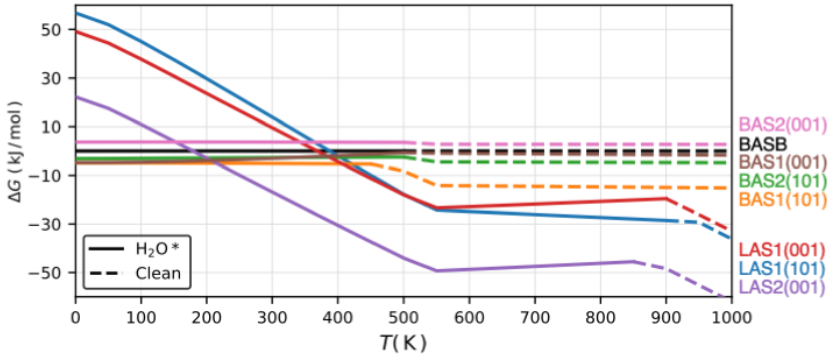


**Figure 3.7:** Free energies of surface acid sites compared to the BAS in the bulk ($\Delta G\,(\mathrm{BASB}) = 0$)). Water-adsorbed and desorbed acid sites are considered, the states lower in free energy are depicted. Adsorptions at the oxygen with the lowest Gibbs free energy at 400 °C was considered only. Reproduced from Ref. 125 with permission from ACS.

Next, I study adsorption free energies ($G_{\mathrm{ads}}$) for water, pyridine, methanol, and dimethyl ether. Pyridine is used to characterize acid sites (see above) and methanol and DME will be subject to section 3.3, where methanol dehydration will be discussed. For BASs, all oxygen atoms within the active site have been considered. All corresponding free energies at 0 K, 200 °C, and 400 °C are listed in Tables A.1 and A.2. Adsorption free energies at 0 K (listed in Table 3.4) are equivalent to zero-point vibrational-energy corrected adsorption energies. 200 °C and 400 °C are typical temperatures for methanol dehydration[75,134] and methanol-to-olefins process[9], respectively. In Fig. 3.8, these values are visualized using only the

adsorption at the most favorable position of the four different oxygen atoms for BASs. First, adsorption at BASs will be discussed. Values for $G_{ads}$ are similar for adsorption of a specific molecule at different BASs and different temperatures with the highest variation of 14 kJ/mol for pyridine at 0 K. Values for $G_{ads}$ are also similar for water, DME, and methanol at a specific BAS, while these are much lower for pyridine. At 0 K, generally an ordering for $G_{ads}$ of $H_2O$ < MeOH ≈ DME < pyridine from weakest to strongest adsorption. The corresponding values vary from −67 kJ/mol to −80 kJ/mol, from −82 kJ/mol to −91 kJ/mol, from −79 kJ/mol to −90 kJ/mol, and from −165 kJ/mol to −177 kJ/mol for $H_2O$, MeOH, DME, and pyridine, respectively. $G_{ads}$ increases with increasing temperature. At 200 °C, adsorption is still favorable, but becomes positive at 400 °C for $H_2O$, MeOH, and DME with values for $G_{ads}$ from 11 kJ/mol to 28 kJ/mol while losing a systematic ordering between these three molecules present at 0 K. For pyridine, $G_{ads}$ is still negative with values between −54 kJ/mol to −68 kJ/mol. Adsorption free energies at LASs are significantly lower than at BASs. At 400 °, $G_{ads}$ is for all adsorbates still negative. For LASs the ordering $H_2O$ < MeOH < DME < pyridine from weakest to strongest adsorption holds generally for all depicted temperatures. The only exception is LAS2(001), where MeOH adsorption is more favorable than DME adsorption. While the differences for $G_{ads}$ for adsorption of $H_2O$ and MeOH are small at different LASs (≤ 10 kJ/mol) , these differences are larger for DME and pyridine (≤ 26 kJ/mol), whereby they are also larger than for BASs. Adsorption free energies are at 0 K between −126 kJ/mol ($H_2O$ at LAS1(101)) and −205 kJ/mol (pyridine at LAS1(001)) and at 400 °C between −31 kJ/mol ($H_2O$ at LAS2(001)) and −88 kJ/mol (pyridine at LAS1(001)).

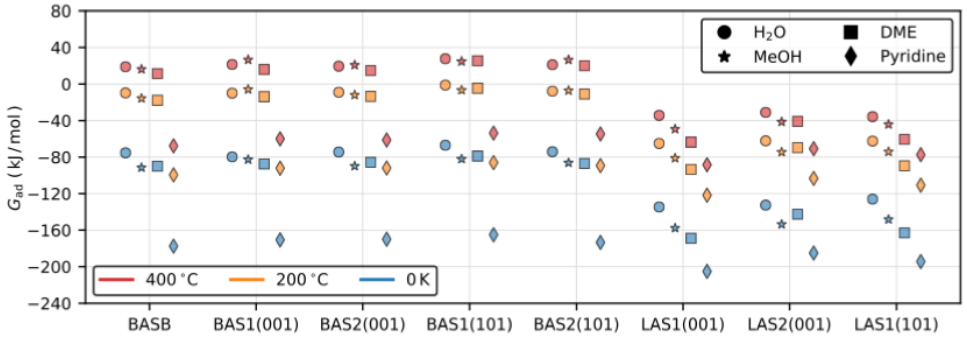


**Figure 3.8:** Adsorption free energies at 0 K, 200 °C, and 400 °C of water, methanol, DME, and pyridine at all acid sites. Reproduced from Ref. 125 with permission from ACS.

**Table 3.4:** Computed zero-point vibrational-energy corrected adsorption energies $E_{ads}$ for $H_2O$, methanol, DME, and pyridine in kJ/mol. Reproduced from Ref. 125 with permission from ACS.

| | $H_2O$* | MeOH* | DME* | Pyridine* |
|---|---|---|---|---|
| LAS1(101) | -126 | -148 | -163 | -194 |
| LAS1(001) | -135 | -158 | -169 | -205 |
| LAS2(001) | -133 | -154 | -143 | -185 |
| BAS1(101) | -67 | -82 | -79 | -165 |
| BAS2(101) | -74 | -86 | -87 | -173 |
| BAS1(001) | -80 | -83 | -88 | -171 |
| BAS2(001) | -74 | -90 | -84 | -170 |
| BASB | -75 | -91 | -90 | -177 |

## 3.3 Methanol Dehydration at Zeolite Surface Lewis and Brønsted Acid Sites

I investigated the dehydration of methanol to DME on surface acid sites to evaluate their role in zeolite catalyzed processes. Methanol dehydration is an extensively studied reaction, both theoretically [118,119,121–124,196] as well as experimentally [123,134,197]. It is an important step within the methanol-to-olefins dehydration and has many similarities to other reactions, like methylation of aromatics or olefins. [161,164,183,198–201] Additionally, DME is an important chemical for the industry and also discussed as an alternative fuel. [202] Thus, the methanol dehydration is a well understood and important reaction and therefore it is an appropriate probe reaction to test the reactivity of surface acid sites. Two mechanisms exist for the DME formation from methanol at BASs, the concerted (also called associative or direct) and the step-wise (also called dissociative) mechanism. In the step-wise mechanism (Fig. 3.9a), a methanol molecule becomes protonated first and rotates afterwards to react to an SMS releasing water (TS-s1). Next, the SMS reacts with the second methanol to protonated DME by transferring the methyl group (TS-s2). Protonation reactions of DME and methanol have not been computed explicitly for this study, since corresponding barriers are expected to be negligible. For methanol protonation, this has been proven previously. [203] In the concerted mechanism (Fig. 3.9b), two co-adsorbed methanol molecules react directly with each other through an $S_N2$ type reaction (TS-cB). For this, a methyl group is transferred from protonated methanol to another methanol molecule yielding protonated DME and water. For LASs, an equqivalent mechanism (Fig. 3.9c) was investigated. A methanol adsorbs as a Lewis adduct to the LAS and reacts concertedly with another methanol analogously to the concerted mechanism at BASs. Protonated DME and a negatively charged Al-OH group are formed. The latter is isoelectronic to a silanol group. A proton shift yields DME and water, whereby water is also bonded as a Lewis adduct and has to be released to recover the acid site.

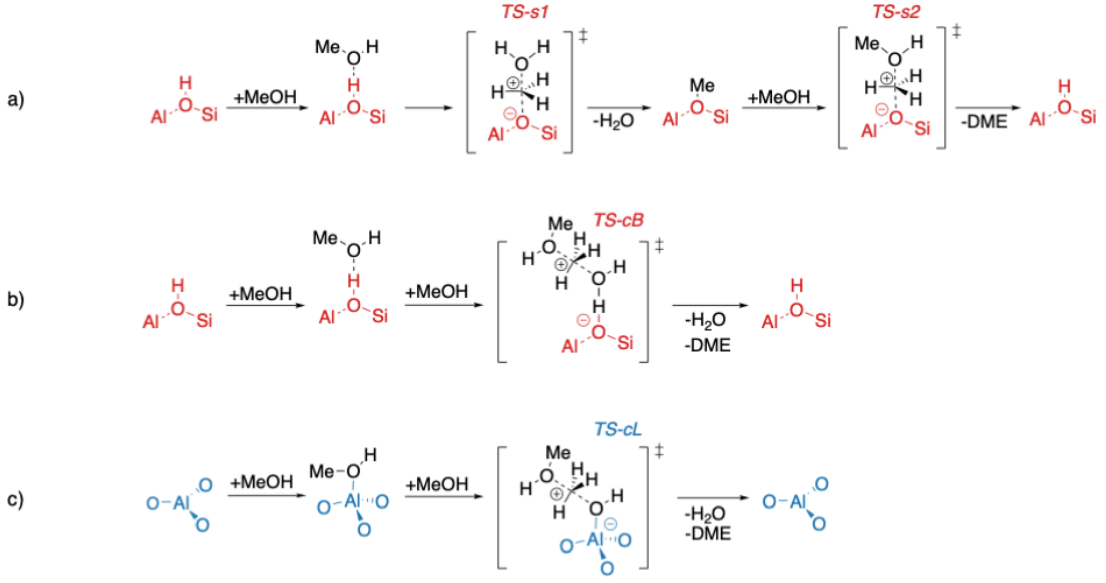


**Figure 3.9:** Step-wise (a) and concerted (b) mechanism for methanol dehydration at BASs, and corresponding mechanism at LASs (c). Reproduced from Ref. 125 with permission from ACS.

Fig. 3.10 shows all four transition state structures exemplary for the (101) surface (BAS2(101) and LAS1(101)). TS-cB and TS-cL generally look similar, but in TS-cB, the methanol molecules are bound loosely to the framework with hydrogen bonds, while in TS-cL, the oxygen atom of one methanol molecule is strongly bonded during the whole reaction in a Lewis adduct. With a bond length of 180 pm for the Al-O bond in the strongly adsorbed methanol at LAS1(101), this distance is similar to the other three Al-O bonds of the active site, which have an average length of 174 pm. The water molecule remaining at the end of the reaction at the active site is also strongly bound with an Al-O distance of 194 pm. The adsorption free energies have been discussed in section 3.2. In TS-s1 and TS-s2, the distances between the methyl group and the reaction partners almost equal with 199 pm and 200 pm in TS-s1 and 199 pm and 201 pm in TS-s2, respectively.

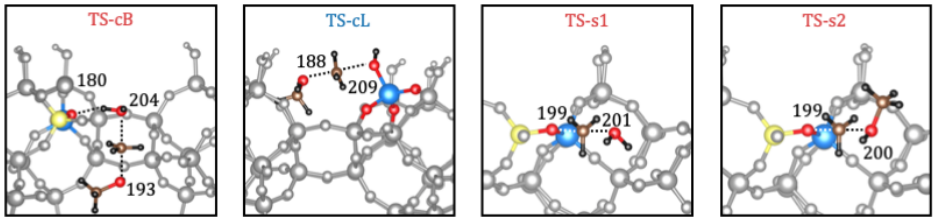


**Figure 3.10:** Transition state structures at BAS2(101) and LAS1(101). Reproduced from Ref. 125 with permission from ACS.

In Table 3.5 barriers for all acid sited are listed at 200 °C and 400 °C for the concerted and step-wise mechanism. For TS-s1 and TS-s2, reactions at all four oxygen atoms within the active sites have been considered for the location of SMS. Only the reaction at the oxygen with the the lowest free energy is depicted. For the reactions at the other oxygen atoms, see Tables A.3 and A.4. As reference state for reaction barriers, generally the most stable previous state was chosen. At 200 °C, this is adsorbed methanol for barriers of TS-cB, TS-cL, and TS-s1. Depending on the active site, MeOH or SMS is more stable. For consistency, SMS is chosen as reference state for the barriers of TS-s2. At 400 °C, reference state for barriers of TS-cL still is adsorbed methanol and of TS-s2 it still is SMS. For barriers of TS-cB and TS-s1, the reference state becomes the desorbed acid site and gaseous methanol.

**Table 3.5:** Barriers in kJ/mol for concerted and step-wise DME formation for all acid sites. At 200 °C, reference states are single-adsorbed MeOH for TS-s1, TS-cB, and TS-cL and SMS for TS-s2. At 400 °C, reference states are single-adsorbed MeOH for TS-cL, the clean acid site for TS-cB and TS-s1, and SMS for TS-s2. Reproduced from Ref. 125 with permission from ACS.

| | concerted | | step-wise | | | |
|---|---|---|---|---|---|---|
| | TS-cB / TS-cL | | TS-s1 | | TS-s2 | |
| | 200 °C | 400 °C | 200 °C | 400 °C | 200 °C | 400 °C |
| BASB | 162 | 211 | 139 | 158 | 129 | 163 |
| BAS1(001) | 158 | 224 | 136 | 164 | 128 | 162 |
| BAS2(001) | 151 | 204 | 128 | 152 | 123 | 158 |
| BAS1(101) | 165 | 226 | 153 | 181 | 141 | 176 |
| BAS2(101) | 155 | 216 | 148 | 177 | 136 | 169 |
| LAS1(001) | 164 | 200 | - | - | - | - |
| LAS2(001) | 162 | 194 | - | - | - | - |
| LAS1(101) | 157 | 192 | - | - | - | - |

Fig. 3.11 shows the Gibbs free energy diagram for the step-wise mechanism at 200 °C for all BASs. For calculating barriers, reference states are single-adsorbed MeOH for TS-s1, and SMS for TS-s2 at 200 °C. In addition to the adsorption energies discussed in the previous section, the transition-state energies are similar, too. The maximum difference for DME and methanol adsorption free energies between surface BASs and BASB is 13 kJ/mol. The maximum difference for barriers between surface BASs and BASB is 14 kJ/mol. The corresponding mean absolute deviations are 9 kJ/mol and 7 kJ/mol for TS-s1 and TS-s2, respectively. At 200 °C, TS-s1 has a higher barrier than TS-s2 by 9 kJ/mol on average and is therefore rate-determining for the step-wise mechanism. Only for BAS2(001), TS-s1 has a lower barrier than TS-s2, when referenced to adsorbed methanol instead of SMS, which has a higher free energy than adsorbed methanol in this case. This changes at 400 °C, where at different BASs, TS-s1 or TS-s2 have the higher barrier, but all in all are similar. When comparing reactions at different oxygen atoms within a specific active site (see Tables A.3 and A.4), the difference for the barriers can be considerably large. At 200 °C the range of reaction barriers for TS-s1 varies up to about 50 kJ/mol for different oxygen atoms for a specific active site. For TS-s2, these differences are smaller with values up to about 20 kJ/mol (which still a large). Thus, the reactions will take place at specific oxygen atoms, while other oxygen atoms have a negligible role for the overall reaction rate.

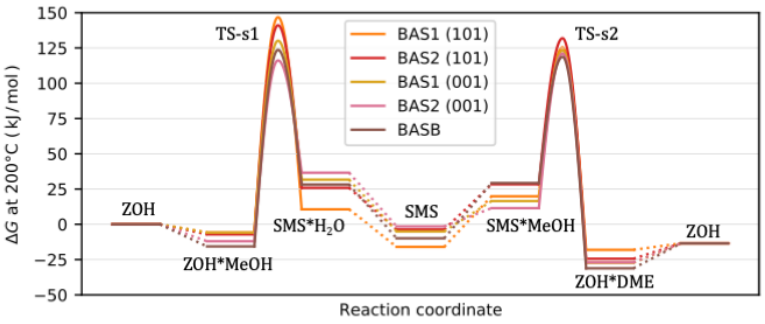


**Figure 3.11:** Gibbs free energy diagram at 200 °C for step-wise DME formation at BASs. Reproduced from Ref. 125 with permission from ACS.

Fig. 3.12 shows the Gibbs free energy diagram for the concerted mechanisms at 200 °C for all BASs and LASs. Again, all states are similar in their free energies within a given type of acid site (BAS or LAS). The free energies for the reaction at LASs is systematically shifted to lower values for all states compared to the states BASs, but apart from that, the diagram is similar. For LAS1(101) and BAS2(101) these differences in free energies are about 60 kJ/mol. When calculating barriers within the energy span model, thus, referencing the transition state to the previous state lowest in free energy, the barriers for both, BASs and LASs, also are similar. The maximum difference in reaction barriers from surface acid sites to the bulk acid site is 11 kJ/mol and the corresponding mean absolute deviation of these differences is 6 kJ/mol including BASs as well as LASs. When comparing the concerted barriers at 200 °C and 400 °C, the barriers for BASs increase faster than for LASs. The barriers for TS-cB and TS-cL increase on average by 58 kJ/mol and 34 kJ/mol, respectively. At 400 °C these barriers are lower at LASs than at BASs. Since adsorptions at LASs are stronger than at BASs, at 400 °C the previous most stable state for TS-cL still is adsorbed methanol, while TS-cB is referenced to the desorbed state, which is more stable. Thus, at higher temperatures, when BASs are desorbed and LASs still have methanol adsorbed, the barriers for TS-cB depend more strongly on the temperature than the barriers for TS-cL due to different entropic contributions resulting from an additional desorbed methanol molecule for BASs. Therefore, barriers for

TS-cB increase faster with the temperature than barriers for TS-cL until the desorbed reference state is also more favorable for LASs. Desorbed methanol will be more favorable only above about 700 °C for LASs, while it is already more favorable for BASs at about 240 °C to 300 °C.

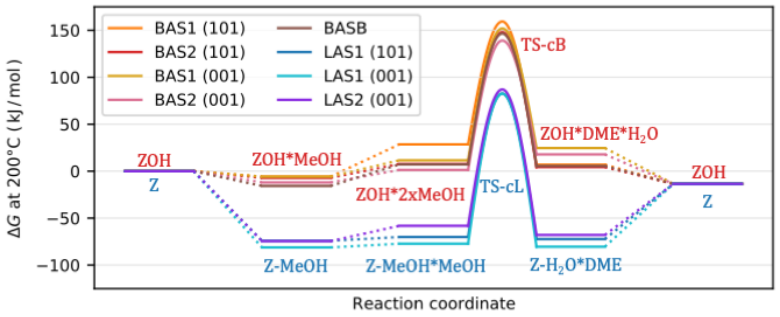


**Figure 3.12:** Gibbs free energy diagram at 200 °C for concerted DME formation at BASs and LASs. Reproduced from Ref. 125 with permission from ACS.

Furthermore, the barriers for TS-cB are higher by 7 kJ/mol to 23 kJ/mol (absolute mean deviation: 17 kJ/mol) than for TS-s1 at 200 °C and therefore the step-wise reaction will be the dominating reaction. At 400 °C, this difference increases to values of 39 kJ/mol to 60 kJ/mol (absolute mean deviation: 50 kJ/mol). This conclusion is in line with earlier kinetic work, where the step-wise mechanism is favored versus the concerted mechanism due to higher entropic penalty.[123,124,196] Arvidson et al. found in their kinetic study for the H-SSZ-13 zeolite (bulk acid site) a crossover from the concerted to the step-wise mechanism at about 600 K, while their calculated barriers at 200 °C are similar for both mechanisms.[196]

As already discussed above, adsorptions are at LASs significantly stronger than at BASs. For recovering the catalyst function, adsorbates have to be removed from the active sites. Hence, catalyst poisoning (catalyst deactivation caused by strong adsorptions) becomes an important subject for LASs. The water formed as a by-product during DME formation is strongly bound as a Lewis-adduct to the acid site. Therefore, recovery from water poisoning will be discussed in the following. The adsorption energy of water at LASs has a high value of about 130 kJ/mol (cf. Table 3.4). I studied two mechanisms for recovery of water-adsorbed LASs (see Fig. 3.13a): First, the transition of this coordinatively-bound water to a loosely-bound water, which has a hydrogen bond to a silanol group at the surface termination. This loosely-bound water can be easily desorbed afterwards. Second, the reaction from the coordinatively-bound water molecule with a methanol molecule to an coordinatively-bound methanol molecule and a loosely-bound water molecule. This mechanism is comparable to the second step-wise reaction (TS-s1) as the coordinatively-bound methanol molecule can be interpreted as an SMS. In Fig 3.13b and c, the Gibbs free energy diagram and transition state structures are exemplarily shown for LAS1(101).

In Table 3.6, the corresponding barriers are shown for all transition states at 200 °C. The barrier for TS-r1 is substantially lower than for TS-r2. While the reaction for TS-r1 will take place easily with barriers between 104 kJ/mol to 116 kJ/mol, the reaction for TS-r2 has slightly higher barriers than TS-cL with values of 157 kJ/mol to 174 kJ/mol. Thus, the second mechanism is less relevant.

Considering TS-r2, which resembles the SMS formation at BASs, a step-wise mechanism can be formulated for LASs (cf. Fig. 3.14a and b). Water-adsorbed LASs are already known to behave like BASs.[58] This state has a four-fold coordinated aluminum, which is equivalent to a BASs, where the bridging hydroxyl group (Al-OH-Si) is exchanged by the water molecule (Al-$OH_2$). This adsorbed water molecule

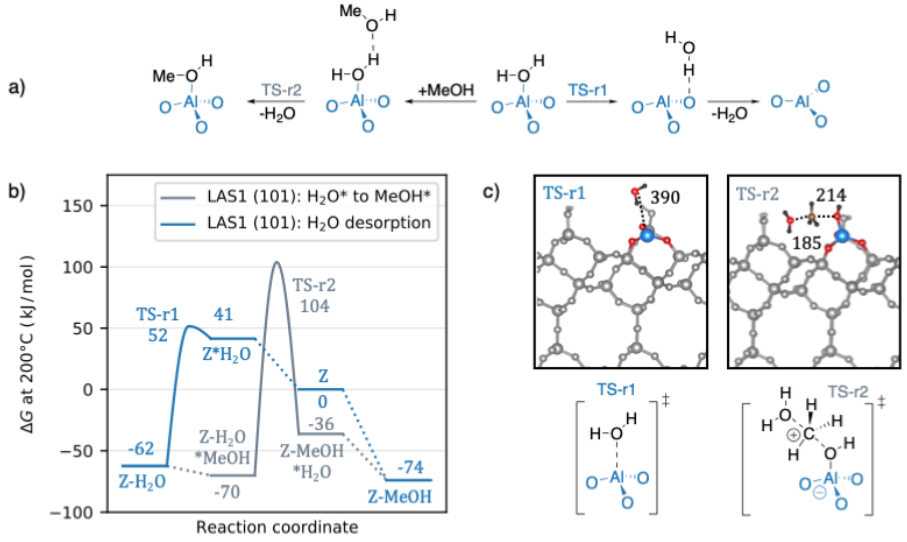


**Figure 3.13:** Mechanism a), Gibbs free energy profile b), and transition state structures c) for Lewis acid side recovery. Reproduced from Ref. 125 with permission from ACS.

**Table 3.6:** Barriers in kJ/mol for recovery of the LAS at 200 °C. Reference states are coordinatively-bound water for TS-r1 and coordinatively-bound with coadsorbed methanol for TS-r2. The Barrier for TS-r2 at LAS2(001) is also referenced to coordinatively-bound water, which is 2 kJ/mol more favorable than the co-adsorbed state.

| | TS-r1 | TS-r2 |
|---|---|---|
| LAS1(001) | 104 | 157 |
| LAS2(001) | 116 | 174 |
| LAS1(101) | 114 | 174 |

then protonates a methanol molecule and via TS-r2 a coordinatively-bound methanol molecule is formed. The resulting state is analogous to an SMS and thus, the reaction is comparable to the SMS formation via TS-s1. Correspondingly, the following reaction via TS-cL is analogous to the reaction via TS-s2. However, barriers for TS-r2 are considerably higher than for TS-s1, due to adsorption of an additional molecule from the gas phase leading to an entropical penalty. The barrier for TS-r2 is also higher than for TS-cL. Since the above explained mechanism for the concerted mechanism at LASs does not require TS-r2 and water can be removed more easily by TS-r1, this step-wise mechanism is unfavorable for LASs. Starting from either a water-adsorbed or an empty LAS, the concerted mechanism will dominate over this step-wise mechanism.

At surface LASs, SMS can also be formed at the three oxygen atoms within the active site (see Fig. 3.15. After water adsorption an proton can be transferred from that water to an adjacent oxygen atom. The active center of the formed BAS has an terminating HO group at the aluminum instead of repetitive -O-Si-O- groups compared to a fully framework-embedded BAS. After methanol adsorption, an SMS can be formed releasing water. However, this SMS formation has a higher barrier which is higher by 48 kJ/mol than the concerted DME formation at LAS1(101) as shown in Fig. 3.15. Hence, mechanisms including such SMS groups are not relevant for DME formation.

Comparing PBE-D3 barriers and cluster-model corrected energies, the first are significantly lower. The PBE-D3 level of theory underestimates barriers (referenced to the clean site) by 40 kJ/mol and 20 kJ/mol

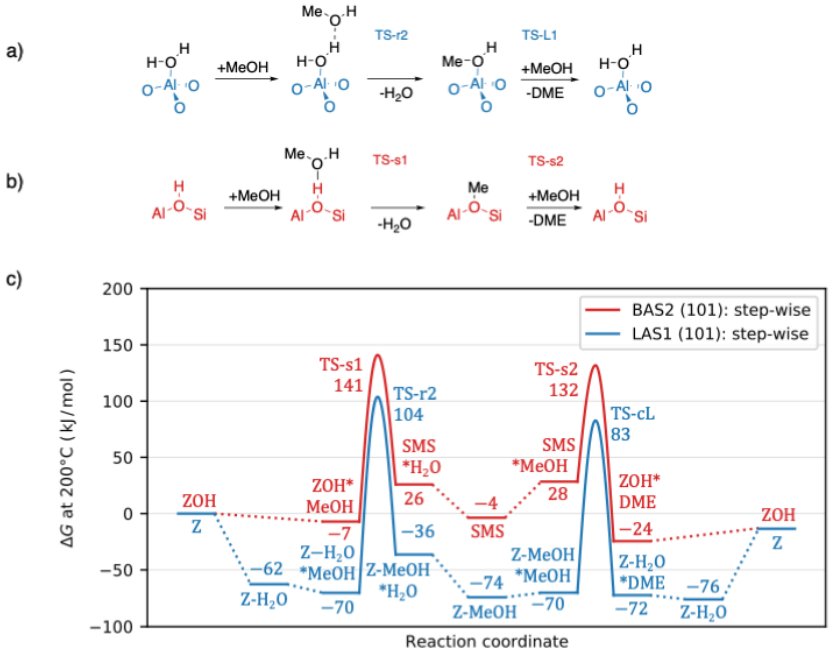


**Figure 3.14:** Step-wise mechanism at BASs a) and LASs b) and corresponding Gibbs free energy profile at 200 °C for LAS1(101) and BAS2(101) c). Reproduced from Ref. 125 with permission from ACS.

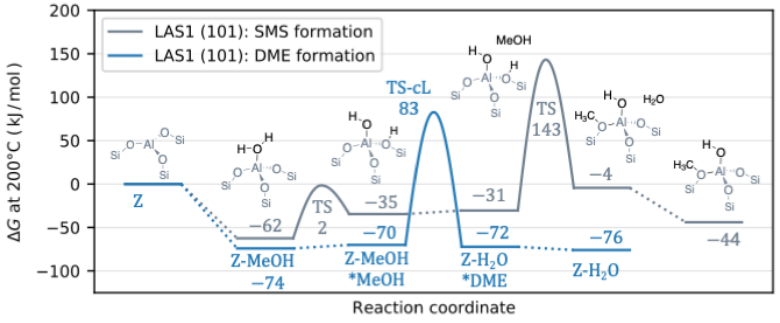


**Figure 3.15:** SMS formation at 200 °C for LAS1(101). Reproduced from Ref. 125 with permission from ACS.

for the concerted and step-wise mechanism, respectively (see Table A.5 and A.6). For TS-cB, the deviation is higher than for TS-cL with mean values of 44 kJ/mol, and 27 kJ/mol, respectively. However, this value increases for TS-cL, when the corresponding barrier is referenced to the methanol-adsorbed state instead of the desorbed acid site. For BASs the methanol adsorption is corrected by about 20 kJ/mol, while it is −3 kJ/mol to −13 kJ/mol for LASs.

## 3.4 Summary and Conclusion

The primary factor determining the stability of zeolite surfaces is the number of silanol groups per surface area. Investigating further surface acid sites of the (101) and (001) facet, I found surface BASs to be similarly stable as the BAS located inside the zeolite bulk. Additionally, I found water-adsorbed surface

LASs to be more stable than BASs at temperatures exceeding about 250 K to 450 K (depending on the specific acid site). Thus, the formation of LASs is thermodynamically likely for synthesis temperatures reaching about 150 °C. Desorption of water from LASs will easily proceed, for which I computed low barriers for the transition between coordinatively-bound to hydrogen-bound species. For step-wise and concerted DME formation, which I used as probe reactions to test the reactivity of surface acid sites, surface BASs have similar reaction barriers as the BAS inside the zeolite bulk. DME formation at LASs resembles the concerted DME formation at BASs in mechanism and in reaction barriers of about 160 kJ/mol at 200 °C. While free energies for states of LAS-catalyzed reactions are systematically shifted to lower values compared to BAS-catalyzed reactions, barriers are similar when referenced to the previous most stable state. However, the step-wise mechanism at BASs has slightly lower barriers at 200 °C. Thus, LASs have a subordinate role for methanol dehydration to DME, but might be important for reactions dominated by concerted mechanisms, provided that active site poisoning is a minor issue: Considering a specific reaction at BASs where the adsorbed state of reactants is less favorable than the desorbed state, the barrier is referenced to latter state. For a corresponding reaction at LASs, the transition state is still stabilized compared to that of BASs. Consequently, a lower barrier is obtained for LAS than for BAS.

# 4

# Reactivity of Acetic Acid in H-SSZ-13

*This chapter is based on* [Philipp Huber and Philipp N Plessow. A computational investigation of the decomposition of acetic acid in H-SSZ-13 and its role in the initiation of the MTO process. *Catal. Sci. Technol.*, 13(6):1905–1917, 2023].

Acetic acid can be converted to acetone or isobutene, for which zeolites[11,34–38,204,205] as well as metal oxides[206–213] have been investigated as catalysts. At present, acetone is mainly produced from the cumene process, which requires fossil resources.[214,215] Since acetic acid can be obtained from renewable resources, this provides a sustainable alternative for acetone and isobutene production. The mechanism taking place in zeolites is still not clarified. A first proposal for the reaction mechanism from acetic acid to acetone was made by Paschke and Neunhoeffer in 1939.[216] They claimed an H-atom in $\alpha$-position to the keto group of carboxylic acids to play a decisive role, since carboxylic acids with a tertiary C-atom next to the carboxy group do not form ketons. Subsequently, they proposed the coupling of two acetic acid molecules to a $\beta$-ketoacid, which is 3-oxobutanoic acid in this case. Decarboxylation afterwards yields acetone and carbon dioxide. A schematic formula of this ketonic decarboxylation of acetic acid is depicted in Fig. 4.1.

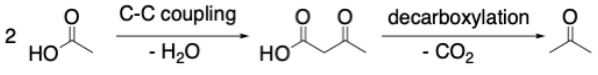


**Figure 4.1:** Schematic reaction equation for the ketonic decarboxylation of acetic acid to acetone. Reproduced from Ref. 217 with permission of RSC.

Resasco and coworkers also investigated the ketonic decarboxylation for several catalysts including metal oxides as well as zeolites.[205] They proposed a mechanism where a zeolite surface acetate couples with acetic acid, while also acylium cations and ketenes might be reasonable intermediates.[34,218] This acetate can be formed from dehydration of acetic acid. Crossly and coworkers studied ketonic decarboxylation in H-ZSM-5, where they detected zeolite surface acetate.[204] They suggested a mechanism comprising the coupling of this surface acetate with acetic acid occurring in an enol-like structure during the transition state. Additionally, they suggested that the carbon-carbon coupling rather than the preceding dehydration of acetic acid to the acetate is the rate-determining step. Due to its high reactivity, 3-oxobutanoic acid has not been detected explicitly so far,[219] but in H-ZSM-5[145] and H-SAPO-11[220], acetone was detected during the ketonic decarboxylation of acetic acid.

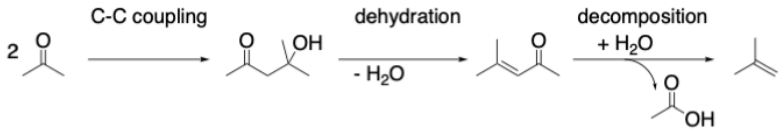


**Figure 4.2:** Schematic reaction equation for the conversing of acetone to isobutene via mesityl oxide. Reproduced from Ref. 217 with permission of RSC.

Aldol self-condensation of acetone to mesityl oxide via diacetone alcohol and subsequent decomposition yields isobutene as depicted in Fig. 4.2. Several experimental investigations have been performed on this subject.[38,221–228] Yan et al. found acetone and isobutene as the main products from acetic acid conversion on several rare-earth modified Beta zeolites at 450 °C.[38] For Y/Beta, they investigated a temperature range between 300 °C and 500 °C with an increasing amount of isobutene yield at higher temperatures and highest acetone yield at 350 °C and 400 °C. Additionally, they identified diacetone alcohol and mesityl oxide as intermediates. In H-ZSM-5, diacetone alcohol, mesityl oxide, and isobutene have been found as products from acetone conversion at 100 °C[224] and between 150 °C and 250 °C[225]. After heating from 0 °C to 240 °C, conversion of acetone in H-SAPO-34 first leads to diacetone alcohol, mesityl oxide, and in the end to isobutene and acetic acid.[226] Herrmann and Iglesia studied this mechanism experimentally for the FER, TON, MFI, BEA, FAU, and MCM-41 zeolites[227,228] as well as theoretically for the H-ZSM-5 zeolite[228] (acetone to mesityl oxide) and for the gas-phase reaction[227] (mesityl oxide to isobutene). For the aldol-conversion of acetone and its enol in H-ZSM-5, they computed significantly higher free energy barriers than for the following dehydration reaction. Hence, they found carbon-carbon coupling to be the rate-determining step.[228] For the reaction from mesityl oxide to isobutene, they computed a reaction path for a radical mechanism at the CCSD level of theory.[227] However, they found high free energy barriers for this radical mechanism, which therefore is unlikely to take place.

In this chapter, I present mechanisms in the H-SSZ-13 zeolite for the conversion of acetic acid to acetone in section 4.1 as well as a mechanism for the subsequent conversion to isobutene in section 4.2. For this, Gibbs free energy reaction paths at 400 °C were computed. Periodic DFT energies are corrected by ab initio calculations of cluster models at the CCSD(T) level of theory (cf. section 2.5). In section 4.3, I investigate these mechanisms in a kinetic batch reactor simulation and in section 4.4, I shortly discuss corresponding mechanisms catalyzed by surface Lewis acid sites instead of catalyzed by Brønsted acid site inside the bulk.

## 4.1 Ketonic Decarboxylation of Acetic Acid to Acetone

Acetic acid can react to other C2 compounds as depicted in Fig. 4.3. Keto-enol tautomerization of acetic acid yields 1,1-dihydroxyethene, which has been proposed to be important for the C-C coupling.[204,205] Dehydration of an acetic acid molecule produces a zeolite surfaces acetate, which was also suggested as a reactant for the C-C coupling.[204,205] Dissociation from the surface yields an acylium cation, which can be subsequently deprotonated to give a ketene.[112–114,148,229–231] These C2-derivatives can couple with each other to 3-oxobutanoic acid. Coupling between two carbon atoms requires a nucleophilic and an electrophilic carbon atom. Acetic acid and the zeolite surface acetate have an electrophilic carbon atom, 1,1-dihydroxyethene has a nucleophilic carbon atom, and ketene has both, an electrophilic and a nucleophilic carbon atom. Several possibilities how these C2-derivatives can react with each other to 3-oxobutanoic acid exist, which I will discuss in the following.

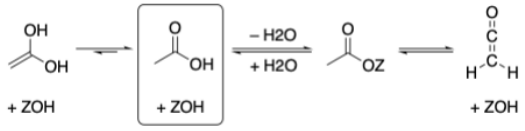


**Figure 4.3:** Conversions between C2 derivatives, which have been considered for C-C coupling reactions. Reproduced from Ref. 217 with permission of RSC.

Fig. 4.4a shows the mechanism comprising the reaction between ketene and acetic acid and between two ketenes. The corresponding Gibbs free energy diagram is shown in Fig. 4.4b and some important transition state structures are depicted in Fig. 4.4c. For intermediates, desorbed as well as adsorbed states have been computed, but only the state lower in free energy is depicted in the Gibbs free energy diagrams. The adsorption free energy of acetic acid is positive with a value of 7 kJ/mol. First, acetic acid (A1) dehydrates to a zeolite surface acetate (A2) with a barrier of $\Delta G^{\ddagger} = 149\,\mathrm{kJ/mol}$ at O1 (see Fig. 2.2 for the numbering of oxygen atoms in H-SSZ-13). This barrier was also calculated at O3, which is slightly higher with $\Delta G^{\ddagger} = 153\,\mathrm{kJ/mol}$. The dissociation from the zeolite has a Gibbs free energy of $\Delta G = 69\,\mathrm{kJ/mol}$ referenced to gaseous acetic acid and therefore is smaller than the corresponding value for the acylium ion (A3, $\Delta G = 87\,\mathrm{kJ/mol}$). Considering DFT free energy values only, this backward barrier is $\Delta G^{\ddagger}_{\mathrm{DFT}} = 1\,\mathrm{kJ/mol}$; however, cluster-model corrections decrease the value for TS(A2-A3) and increase the value for A3. The following deprotonation to ketene (C1) has a small barrier of $\Delta G^{\ddagger} = 93\,\mathrm{kJ/mol}$ and thus can be easily formed. Gaseous ketene is by 41 kJ/mol less stable than the gaseous acetic acid reference. The adsorption free energy of ketene is high with $\Delta \mathrm{G_{ads}} = 41\,\mathrm{kJ/mol}$. Forming a second ketene, the state C2 with two gaseous ketene molecules, two gaseous water molecules, and the empty zeolite has a Gibbs free energy of 81 kJ/mol relative to the reference state and the corresponding state with co-adsorbed ketenes has a Gibbs free energy of 190 kJ/mol. These ketenes can react with each other, initiated by protonation of one ketene to an acylium cation. The nucleophilic carbon atom of the other ketene attacks the electrophilic carbon atom of the transient acylium cation, yielding acetylketene (C3) with a barrier of 202 kJ/mol. Hence, the barrier only is $\Delta G^{\ddagger} = 12\,\mathrm{kJ/mol}$, when referenced to the co-adsorbed state. Having also a high C-C distance of 327 pm in the transition state, this emphasizes the high reactivity of ketenes. Furthermore, the height of the barrier is mainly due to the high Gibbs free energy of two ketene (and two water) molecules compared to two acetic acid molecules. Acetylketene can subsequently be hydrated to 3-hydroxybut-2-enoic acid (C4). The

uncatalyzed gas-phase reaction has a lower barrier than the zeolite-catalyzed reaction with values of $\Delta G^{\ddagger} = 147\,\mathrm{kJ/mol}$ and $\Delta G^{\ddagger} = 185\,\mathrm{kJ/mol}$, respectively, due to the entropic contributions. At 0 K, the barrier for the catalyzed reaction is by 105 kJ/mol lower than that of the gas-phase reaction.. Finally, keto-enol tautomerization yields 3-oxobutanoic acid proceeding in two steps. First, the carbon atom next to the carboxyl group becomes protonated in TS(C4-C5) and second, the hydroxyl group becomes deprotonated in TS(C5-E1) with barriers of $\Delta G^{\ddagger} = 139\,\mathrm{kJ/mol}$ and $\Delta G^{\ddagger} = 116\,\mathrm{kJ/mol}$, respectively. The Gibbs free energy of 3-oxobutanoic acid is by 51 kJ/mol higher than the acetic acid reference. Acetic acid can also react directly with ketene to 3-oxobutanoic acid via TS(A1-E1) with a barrier of $\Delta G^{\ddagger} = 214\,\mathrm{kJ/mol}$, which is 12 kJ/mol higher than the barrier for TS(C2-C3).

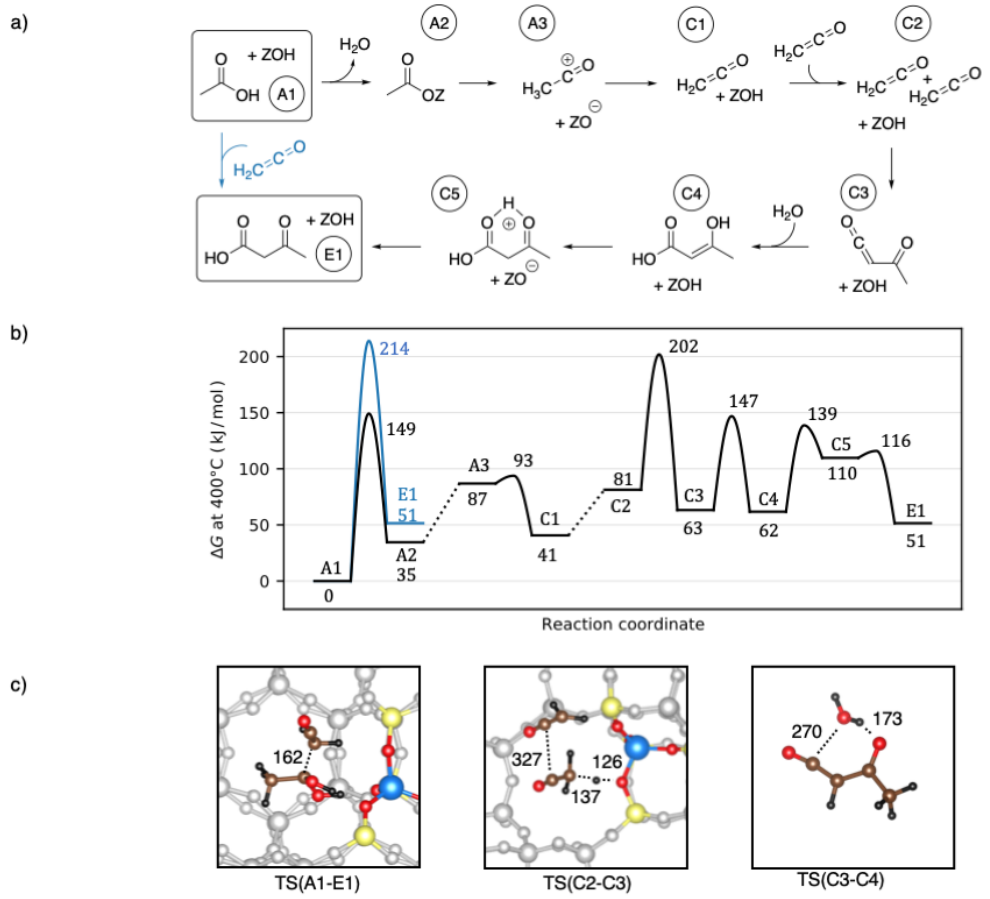


**Figure 4.4:** Mechanism a) and Gibbs free energy diagram at 400 °C b) for the reaction from acetic acid to 3-oxobutanoic acid via coupling between two ketene molecules and via coupling of one ketene and one acetic acid molecule. Reference state is gaseous acetic acid. Transition state structures of the C-C coupling reactions between two ketene molecules c) left and between one ketene and one acetic acid molecule c) middle. Subsequent dehydration reaction c) right. Atomic distances in pm. Reproduced from Ref. 217 with permission of RSC.

Two ketene molecules can also react with each other, forming diketene (Fig. 4.5), which can further react to 3-oxobutanoic acid. This coupling can proceed directly in the gas phase via TS(C2-D4) with a high barrier of $\Delta G^{\ddagger} = 291\,\mathrm{kJ/mol}$. The zeolite-catalyzed reaction takes place in two steps. The two corresponding carbon atoms couple with each other with a barrier of $\Delta G^{\ddagger} = 251\,\mathrm{kJ/mol}$ via TS(C2-D1) and next, the four-membered ring is built by bond formation between another carbon and an oxygen atom with a barrier of $\Delta G^{\ddagger} = 208\,\mathrm{kJ/mol}$ via TS(D2-D4). Thus, the zeolite-catalyzed diketene formation has lower barriers than the gas-phase reaction, but the barrier of $\Delta G^{\ddagger} = 251\,\mathrm{kJ/mol}$ still is high compared

to barriers discussed before in Fig. 4.4. D1 can also react with the zeolite to a zeolite-bound ester (D2) with a barrier of $\Delta G^{\ddagger} = 226\,\mathrm{kJ/mol}$, which further becomes hydrated to 3-hydroxybut-3-enoic acid (D3) with a barrier of $\Delta G^{\ddagger} = 237\,\mathrm{kJ/mol}$. Further dehydration and cyclization yield diketene with a barrier of $\Delta G^{\ddagger} = 272\,\mathrm{kJ/mol}$. D3 can also react in a keto-enol tautomerization to 3-oxobutanoic acid with a barrier of $\Delta G^{\ddagger} = 173\,\mathrm{kJ/mol}$. Diketene can further react to acetylketene. This comprises protonation to D5 with a barrier of $\Delta G^{\ddagger} = 196\,\mathrm{kJ/mol}$, ring opening to D6 with a barrier becoming smaller than D5 after applying the cluster-model correction, and deprotonation to acetylekete with a barrier of $\Delta G^{\ddagger} = 180\,\mathrm{kJ/mol}$. The DFT Gibbs free energy of TS(D5-D6) is 11 kJ/mol higher than D5, after adding the correction term TS(D5-D6) becomes 16 kJ/mol smaller. Acetylketene can react to 3-hydroxybut-3-enoic acid as described above for Fig. 4.4. Note that all mechanism presented here are heavily intertwined. Formation of 3-hydroxybut-3-enoic acid can also be considered via reaction of two ketene molecules through TS(C2-D4) or TS(D1-C4) with subsequent hydration of D4 through the backward reaction of TS(D3-D4) to D3, which tautomerizes to 3-hydroxybut-3-enoic acid. Additionally, diketene can be formed from acetylketene (generated from reaction paths depicted in Fig. 4.4) through the corresponding backward reactions shown in Fig. 4.5. Nevertheless, all reaction paths to 3-hydroxybut-3-enoic acid, which include the formation of diketene, have a rate-determining step with a barrier of at least $\Delta G^{\ddagger} = 251\,\mathrm{kJ/mol}$. This is significantly higher than barriers for other reaction paths to 3-hydroxybut-3-enoic acid and thus, diketene does not play any role for the ketonic decarboxylation of acetic acid in H-SSZ-13 at 400 °C.

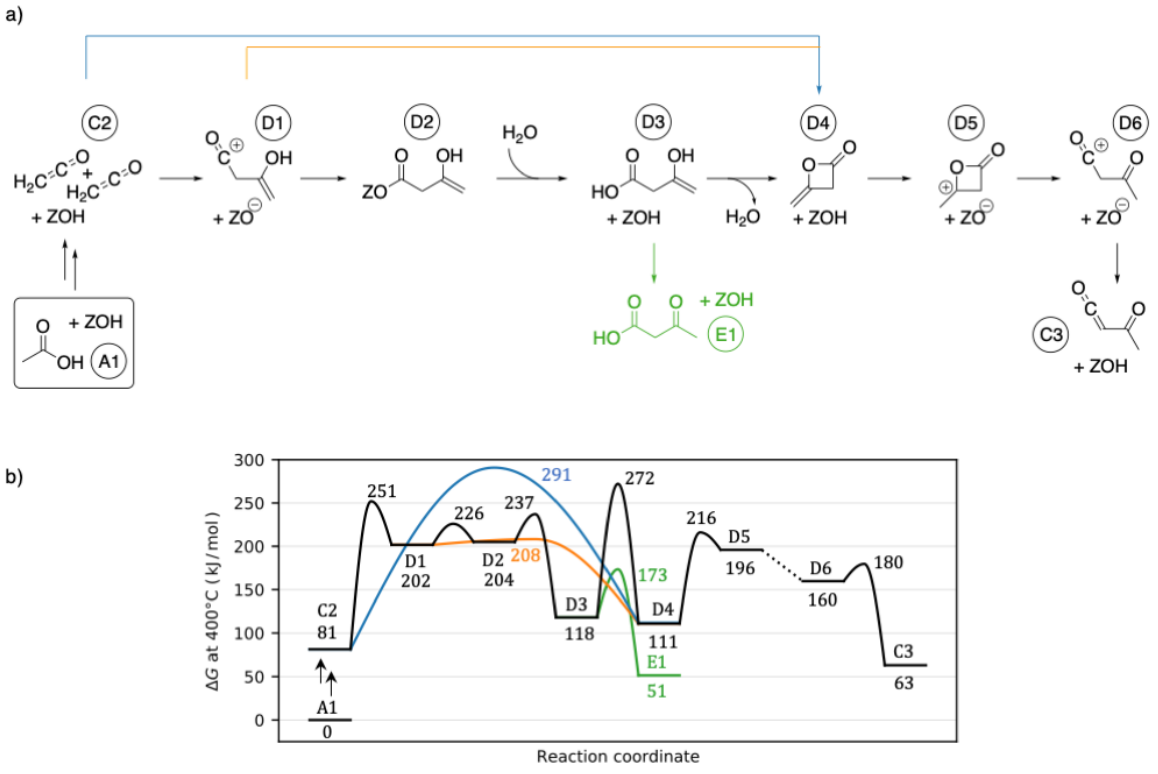


**Figure 4.5:** Mechanism a) and Gibbs free energy diagram at 400 °C b) for additional reactions including the formation of diketene. Reference state is gaseous acetic acid. Reproduced from Ref. 217 with permission of RSC.

In addition to the already described paths from acetylketene to 3-oxobutanoic acid, some more possibilities are shown in Fig. 4.6. Starting from protonated acetylketene (D6), it can react to a zeolite surface

ester (D7) with a DFT free energy difference of 3 kJ/mol between TS(D6-D7) and D6. After adding the cluster-model corrections, TS(D6-D7) becomes lower by 1 kJ/mol than D6. Protonation of this ester yields C5 again with a barrier of $\Delta G^{\ddagger} = 209$ kJ/mol. D6 can also be directly hydrated to C5 with a barrier of $\Delta G^{\ddagger} = 197$ kJ/mol. Another hydration reaction yields a 3-oxobutanoic acid, which is protonated at the acid group (D8). The DFT energy of TS(D6-D8) is by 25 kJ/mol higher than that of D8 and after adding thermodynamic contributions, the DFT free energy of TS(D6-D8) becomes 5 kJ/mol smaller than that of D8. The cluster-model correction increases the free energy difference by 10 kJ/mol. Next, D8 becomes deprotonated to E1 with a barrier of $\Delta G^{\ddagger} = 211$ kJ/mol. All mechanisms presented in Fig. 4.6 have higher barriers for rate-determining steps than the reaction from acetylketene to 3-oxobutanoic acid shown in Fig. 4.4.

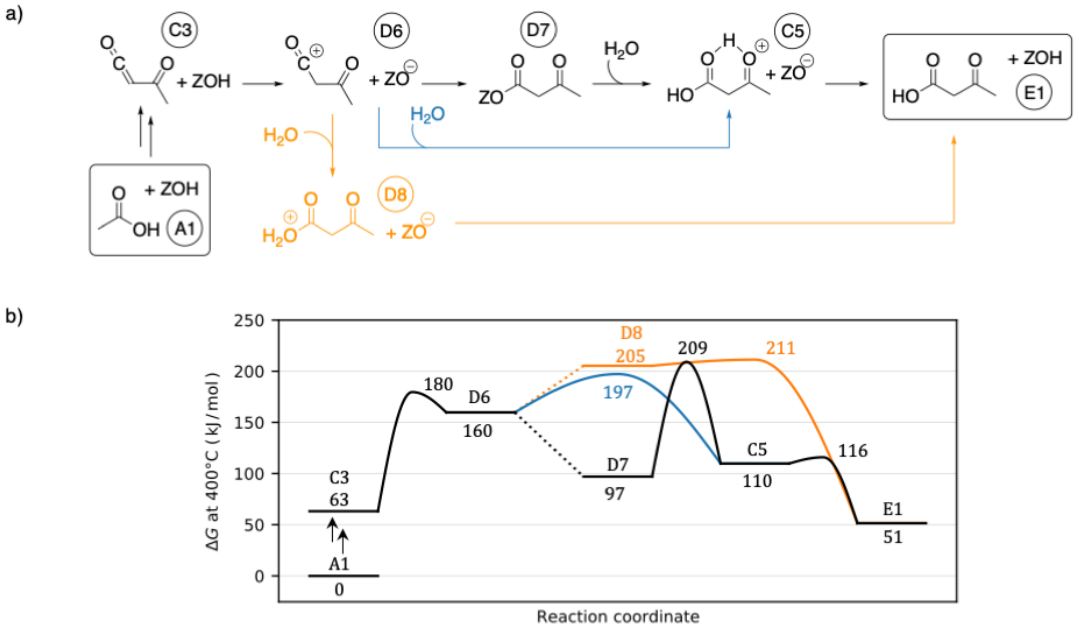


**Figure 4.6:** Mechanism a) and Gibbs free energy diagram at 400 °C b) for additional hydration reactions from the C-C coupled molecule to 3-oxobutanoic acid. Reference state is gaseous acetic acid. Reproduced from Ref. 217 with permission of RSC.

The mechanisms considering C-C coupling with the enol of acetic acid are shown in Fig. 4.7a with the corresponding Gibbs free energy diagram in Fig. 4.7b. The enol 1,1-dihydroxyethene (B1) is by 118 kJ/mol less stable than acetic acid and is formed with a barrier of $\Delta G^{\ddagger} = 189$ kJ/mol. The following reaction between the electrophilic C-atom of acetic acid and the nucleophilic C-atom of the enol to dihydroxymethyl propionic acid (B2) has a high barrier of $\Delta G^{\ddagger} = 244$ kJ/mol. Protonation and dehydration with barriers of $\Delta G^{\ddagger} = 217$ kJ/mol and $\Delta G^{\ddagger} = 242$ kJ/mol yields C5. These barriers are similar to those of the preceding C-C coupling. Reactions of C5 have already been discussed above. 1,1-dihydroxyethene can also react with a zeolite surface acetate, yielding directly 3-oxobutanoic acid. The corresponding reactants (B4) also have a high difference of 153 kJ/mol to the acetic acid reference. The C-C coupling reaction between both has also a high barrier of $\Delta G^{\ddagger} = 259$ kJ/mol. 1,1-dihydroxyethene is a very reactive species, which can be taken from the low intrinsic barriers (referenced to the preceding co-adsorbed state) of $\Delta G^{\ddagger} = 59$ kJ/mol and $\Delta G^{\ddagger} = 52$ kJ/mol for TS(B1-B2) and TS(B4-E1), respectively, as well as from C-C distances during the transition state (Fig. 4.7c) of 470 pm and 322 pm, respectively. Note that, for intermediates in the Gibbs free energy diagrams, the value for the adsorbed or the desorbed

state is shown, depending on which is lower in free energy. This mostly is the state of the empty zeolite and desorbed molecules. In any case, barriers within the energy span product are high for mechanisms comprising 1,1-dihydroxyethene and thus, these are unlikely for the ketonic decarboxylation of acetic acid.

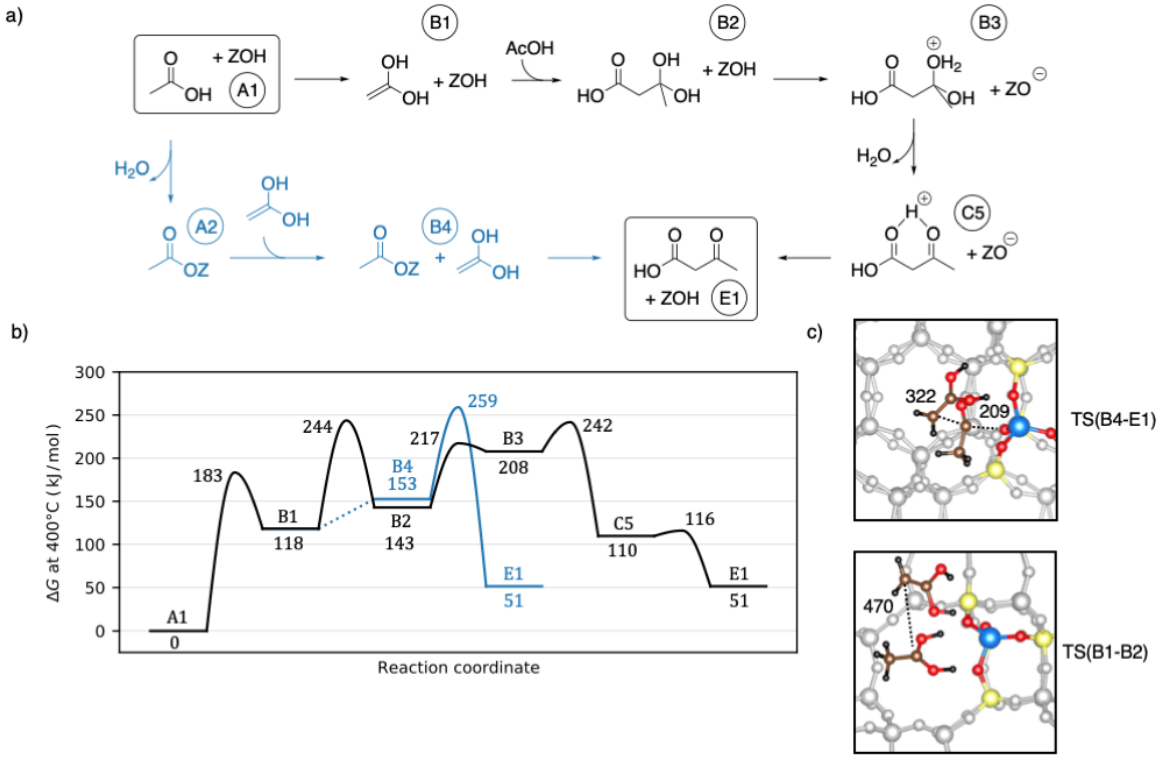


**Figure 4.7:** Mechanism a) and Gibbs free energy diagram at 400 °C b) for the reaction from acetic acid to 3-oxobutanoic acid via coupling reactions involving 1,1-dihydroxyethene. Reference state is gaseous acetic acid. Transition state structures of the C-C coupling reactions between 1,1-dihydroxyethene and a zeolite surface acetate c) top and between 1,1-dihydroxyethene and acetic acid c) bottom. Atomic distances in pm. Reproduced from Ref. 217 with permission of RSC.

In Fig. 4.8, the C-C coupling of a zeolite surface acetate with a ketene is shown. All states in Fig. 4.8a and b have already been discussed above, except this C-C coupling of the zeolite surface acetate and ketene to acetylketene, TS(A2-C3), with a barrier of $\Delta G^{\ddagger} = 197\,\mathrm{kJ/mol}$. The nucleophilic C-atom of ketene attacks thereby the electrophilic C-atom of the acetate with a C-C distance of 288 pm and a C-O distance of 236 pm in the transition state (Fig. 4.8c). A transient acylium ion is formed in the transition state, as it is also the case for TS(C2-C3). Thus, both reactions are similar, differing in the origin of the acylium ion, which is protonation of ketene in TS(C2-C3) and dissociation between the zeolite and the acetyl group in TS(A2-C3). The barriers are also similar with TS(C2-C3) being only 5 kJ/mol higher. The barrier for TS(A2-C3) is lower than for all other C-C coupling reactions presented above and Fig. 4.8 shows the most favorable path from acetic acid to 3-oxobutanoic acid.

So far, many possibilities for the reaction of two C2 derivatives to 3-oxobutanoic acid have been shown. The following decarboxylation of this $\beta$-ketoacid to 2-propenol (E2) proceeds easily with a barrier of $\Delta G^{\ddagger} = 155\,\mathrm{kJ/mol}$ (Fig. 4.9a and b). The reaction starts with protonation of the $\beta$-keto group and subsequently, the acidic proton of the carboxyl group shifts to the zeolite while the distance between the C-atom of the former carboxyl group and the C-atom in former $\alpha$ position increases. In the transition

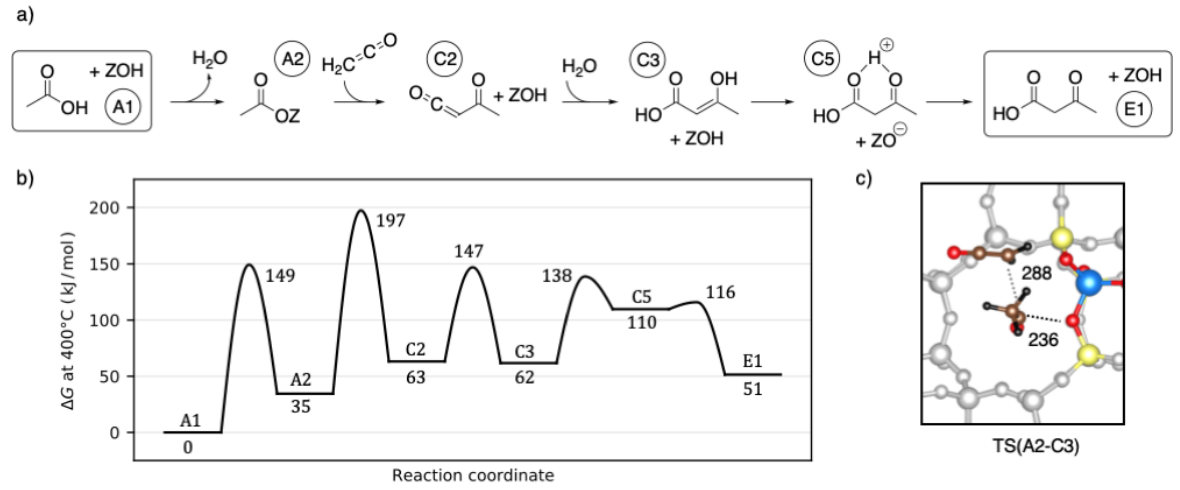


**Figure 4.8:** Mechanism a) and Gibbs free energy diagram at 400 °C b) for the reaction from acetic acid to 3-oxobutanoic acid via coupling between a ketene molecule and a zeolite surface acetate. Reference state is gaseous acetic acid. Transition state structure of the C-C coupling reaction c). Atomic distances in pm. Reproduced from Ref. 217 with permission of RSC.

state, the C-C distance is 218 pm (Fig. 4.9c). The state of 2-propenol is by 66 kJ/mol lower in free energy than 3-oxobutanoic acid. Keto-enol tautomerization yields acetone (E3) with a low barrier of $\Delta G^{\ddagger} = 72\,\mathrm{kJ/mol}$. Acetone is the state lowest in free energy so far with differences of $\Delta G = 67\,\mathrm{kJ/mol}$ and $\Delta G = 67\,\mathrm{kJ/mol}$ referenced to acetic acid and to 3-oxobutanoic acid, respectively.

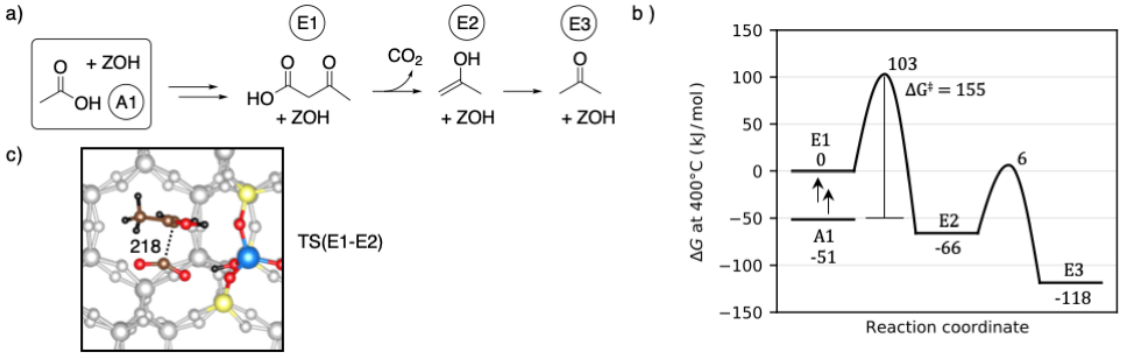


**Figure 4.9:** Mechanism a) and Gibbs free energy diagram at 400 °C b) for the decarboxylation of 3-oxobutanoic acid to acetone. Reference state is adsorbed 3-oxobutanoic acid. Transition state structure of the decarboxylation reaction c). Atomic distances in pm. Reproduced from Ref. 217 with permission of RSC.

Summarizing, the most favorable path for the formation of 3-oxobutanoic acid from acetic acid via coupling of two C2 compounds has a barrier of $\Delta G^{\ddagger} = 197\,\mathrm{kJ/mol}$ for the rate-determining step. The decarboxylation path to acetone has a significantly lower barrier for the rate-determining step of $\Delta G^{\ddagger} = 155\,\mathrm{kJ/mol}$. Thus, the $\beta$-ketoacid can be considered as a rather unstable intermediate and will immediately react further to acetone.

## 4.2 Aldol Self-Condensation of Acetone to Isobutene

The mechanism I computed for the aldol self-condensation of acetone and further reactions to isobutene is depicted in Fig. 4.10a with the corresponding Gibbs free energy diagram in Fig. 4.10b. The reference state of two gaseous acetone molecules and the empty zeolite is by 134 kJ/mol lower in Gibbs free energy than the state of acetic acid. The state of gaseous acetone and gaseous 2-propenol is higher by 53 kJ/mol. In TS(E4-E5), acetone gets protonated and the electrophilic carbon reacts with the nucleophilic carbon of 2-propenol. The barrier is $\Delta G^{\ddagger} = 167\,\mathrm{kJ/mol}$ and the C-C distance in the transition state is 251 pm (Fig. 4.10c). Subsequent deprotonation with a barrier of $\Delta G^{\ddagger} = 181\,\mathrm{kJ/mol}$ yields the enol of diacetone alcohol (E6). Protonation (TS(E6-E7)) and dehydration (TS(E7-E8)) leads to mesityl oxide with barriers of $\Delta G^{\ddagger} = 183\,\mathrm{kJ/mol}$ and $\Delta G^{\ddagger} = 185\,\mathrm{kJ/mol}$. Thus, the rate-determining step for the formation of mesityl oxide is the dehydration reaction (transition state structure: Fig. 4.10c), while the barrier for C-C coupling is by 18 kJ/mol lower and TS(E5-E6) and TS(E6-E7) have almost the same barrier as TS(E7-E8). I additionally investigated the dehydration of diacetone alcohol instead of its enol; however, this reaction has a higher barrier of $\Delta G^{\ddagger} = 196\,\mathrm{kJ/mol}$. The state of mesityl oxide is quite stable and only 15 kJ/mol higher than the state of two acetone molecules. The decomposition of mesityl oxide is initiated by protonation of its secondary C-atom (TS(E8-E9): Fig. 4.10c) with a barrier of $\Delta G^{\ddagger} = 153\,\mathrm{kJ/mol}$. The actual decomposition to isobutene and a zeolite surface acetate (E10) has an intrinsic DFT free energy barrier of $\Delta G^{\ddagger}_{DFT} = 33\,\mathrm{kJ/mol}$ referenced to E9. After adding the cluster-model correction term, the Gibbs free energy of TS(E9-E10) is lower by 24 kJ/mol than E9, which is drastically destabilized. Hence, this barrier becomes irrelevant. The Gibbs free energy of the final state of isobutene and the zeolite surface acetate is by 23 kJ/mol higher than the reference state of acetone, but becomes further stabilized by hydration of the acetate to acetic acid. This shifts the Gibbs free energy 12 kJ/mol below the state of acetone.

Herrmann and Iglesia also computed the aldol self-condensation of acetone, but in the H-ZSM-5 zeolite using another methodology.[228] They used DFT with the RPBE+D3 functional and calculated thermodynamic contributions at 200 °C, whereby they replaced contributions of small frequencies from adsorbed structures by translational and rotational contributions of the corresponding gaseous molecules. This leads to a lower entropic penalty of adsorbed states compared to the methodology used here. They found the C-C coupling reaction to be the rate-determining step instead of the dehydration reaction. When considering free energies (cluster-model corrected) at 200 °C, TS(E7-E8) is higher than TS(E3-E4) by 16 kJ/mol; when considering DFT (PBE-D3) free energies at 200 °C, TS(E7-E8) is higher than TS(E3-E4) by 34 kJ/mol. However, since another methodology as well as another zeolite were applied by Herrmann and Iglesia, comparing both results is difficult.

Summarizing, in H-SSZ-13 the barrier for decomposition of mesityl oxide is smaller than the barriers for conversion of acetone to mesityl oxide at 400 °C. Furthermore, the subsequent conversion of acetone to mesityl oxide has higher barriers than the preceding decarboxylation reaction, but lower barriers than the formation of 3-oxobutanoic acid. Thus, acetone, which has also a low value in the Gibbs free energy profile, is a stable intermediate, while mesityl oxide easily reacts further to isobutene. The final state of isobutene and acetic acid is the lowest state in the Gibbs free energy profile, leading to a thermodynamic driving force towards isobutene formation.

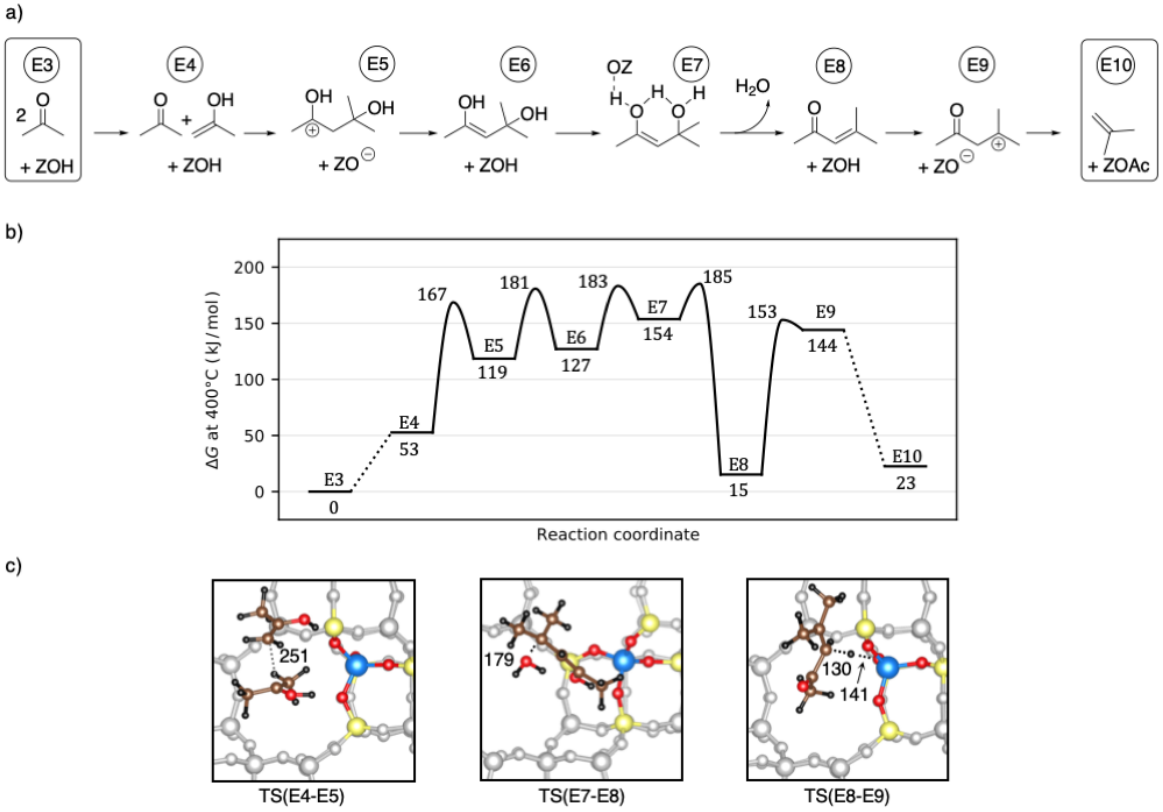


**Figure 4.10:** Mechanism a) and Gibbs free energy diagram at 400 °C b) for the decomposition of acetone to isobutene via mesityl oxide. Reference state is gaseous acetone. Transition state structures for the C-C coupling during the aldol self-condensation c) left, for the dehydration to mesityl oxide c) middle, and for the protonation of mesityl oxide c) right. Atomic distances in pm. Reproduced from Ref. 217 with permission of RSC.

## 4.3 Kinetic Simulation for Acetic Acid Conversion

In the previous sections, the thermodynamics for the ketonic decarboxylation and further aldol condensation of acetone to isobutene have been discussed. While evaluation of the heights of barriers within the corresponding Gibbs free energy profile allows qualitative conclusions, kinetic modeling enables more quantitative statements to be made about this process. Therefore, I performed a simulation for a batch reactor by calculating rate constants of all reactions discussed in sections 4.1 and 4.2. The barriers used in the simulation are listed in Table A.7. I used an initial pressure of 1 bar acetic acid, a temperature of 400 °C, and an acid site concentration of 17.9 mol m$^{-3}$. The corresponding simulation is shown in Fig. 4.11. 3-oxobutanoic acid is immediately formed, but directly decarboxylates without reaching a considerable pressure. The maximum amount of 3-oxobutanoic acid formed is $10^{-6}$ bar after 0.3 s. Within 15 s, the pressure of $CO_2$ strongly increases to about 0.4 bar and then further increases more slowly to about 0.63 bar after 4 min. The pressure of acetone reaches a maximum of 0.31 bar after 9 s and then slowly decays again to 0.09 bar after 4 min, and therefore appears as a stable intermediate. The pressure of acetic acid first decreases fast to 0.30 bar until the maximum pressure of acetone is reached and afterwards it also decreases slowly to 0.08 bar. The pressure of isobutene slowly increases during the whole simulation, converging to the equilibrium while reaching 0.25 bar after 4 min. The pressure of water behaves almost equally to the pressure of carbon dioxide, but is slightly higher. This small difference is

due to the amount of water released from dehydration of mesityl oxide. This water is consumed again after decomposition of mesityl oxide for hydration of the zeolite surface acetate. Thus the difference between the pressures of water and $CO_2$ corresponds to the amount of mesityl oxide present. However, the maximum pressure of mesityl oxide within 4 min is $4 \cdot 10^{-4}$ bar only. This simulation is in agreement with experimental findings.[38,145,220] For example, the group of Lercher detected acetone and $CO_2$ before $C_{2-4}$ olefins were formed during conversion of acetic acid in H-ZSM-5.[145]

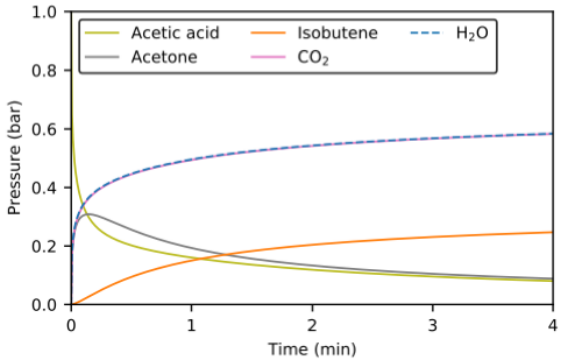


**Figure 4.11:** Kinetic batch reactor simulation for the conversion of acetic acid to isobutene at 400 °C and a feed of 1 bar acetic acid. Adsorption free barriers have not been considered explicitly, but the state lower in free energy, either the adsorbed or the gaseous state, has been taken as product or educt reference for an elementary step. Reproduced from Ref. 217 with permission of RSC.

The relevance of the different reaction paths presented in section 4.1 for the coupling of two C2 compounds can be evaluated by considering the flows through key reaction channels. The main contributions are the reaction path comprising the coupling of ketene with a zeolite surface acetate to acetylketene (TS(A2-C3)) with a percentage of 73.2 % and the reaction path comprising the coupling of two ketene molecules to acetylketene (TS(C2-C3)) with a percentage of 25.8. Additional, the coupling of acetic acid with ketene (TS(A1-E1)) also has a small contribution with 0.9 %. Contributions of other paths are negligible.

**Table 4.1:** Total conversion through key reaction channels for coupling of two C2 compounds during the batch reactor simulation (Fig. 4.11). Reproduced from Ref. 217 with permission of RSC.

| Reaction | pressure (bar) | Percentage (%) |
|---|---|---|
| TS(A2-C3) | 0.44 | 73.2 |
| TS(C2-C3) | 0.15 | 25.8 |
| TS(C2-D4) | 0.00 | 0.0 |
| TS(C2-D3) | 0.00 | 0.0 |
| TS(A1-E1) | 0.01 | 0.9 |
| TS(B1-B2) | 0.00 | 0.0 |
| TS(B4-E1) | 0.00 | 0.0 |

## 4.4 Role of Zeolite Surface Acid Sites

In section 1.3, I discuss the relevance of zeolite surfaces, Lewis acid sites (LASs) in zeolites, and especially LASs located at zeolite surfaces, which I further investigate in chapter 3 for the SSZ-13 surface. Here, I investigate such LAS-catalyzed reactions using the LAS1(101) site (see corresponding sections for details) for key reaction steps of the acetic acid conversion discussed in the previous section. In Fig. 4.12, the

studied reactions are shown. The corresponding mechanism often differs between both acid sites. For LAS-catalyzed reactions, an O-atom of a reactant is bound to the active site as a Lewis adduct. The adsorbed acetic acid is then equivalent to a zeolite surface acetate. Thus, reactions involving such acetates at Brønsted acid sites correspond to the reaction with acetic acid involved at Lewis acid sites. Additionally, a proton is often shifted during the reaction from an adsorbate O-atom to an O-atom of the acid site. Corresponding protonation reactions are neglected. Reactions involving the cationic intermediate from coupling to ketenes (D1) at the Brønsted acid site instead involve only a similar molecule (D1*) at the Lewis acid site due to the absence of an additional proton from the Brønsted acid site. The aldol self-condensation of acetone at the Brønsted-acid-site catalyzed reaction (E5-E6) yields the protonated enol of diacetone alcohol, while the Lewis-acid-site catalyzed reaction (E4-E6*) yields deprotonated diacetone alcohol (aldol adduct). The subsequent dehydration reaction to mesityl oxide was computed by considering diacetone alcohol (E7*) as well as its enol as reactants (E7). The decomposition of mesityl oxide to isobutene involves necessarily a protonation step, which is not possible at Lewis acid sites. For this, an additional water adsorption was considered as a proton source.

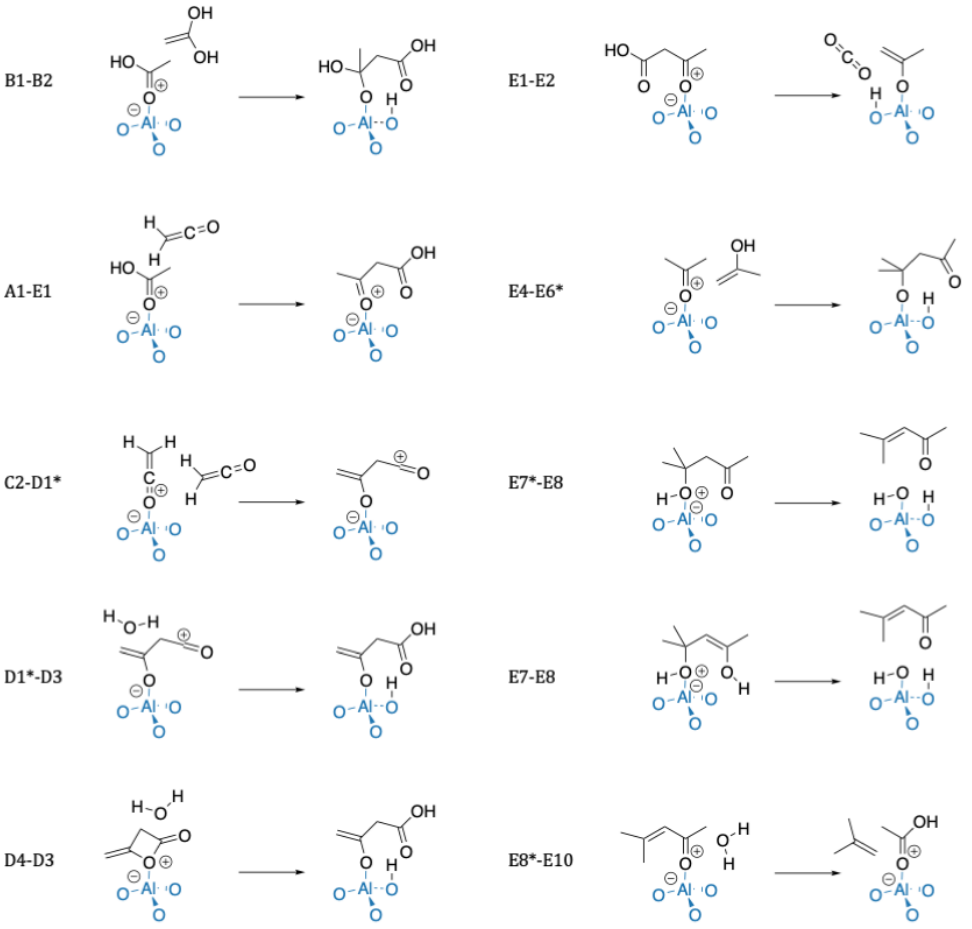


**Figure 4.12:** Mechanisms at the Lewis acid site located at the (101) facet. Reproduced from Reproduced from Ref. 217 with permission of RSC.

Fig. 4.2 compares the barriers for both acid sites. For the reactions at the Brønsted acid site, the label for the comparable reaction at the Lewis acid site is used. The barriers at LAS1(101) are higher, except of TS(D4-D3), TS(E1-E2), and TS(E7-E8), which have slightly lower barriers. The barrier for TS(E8*-E10) is by 152 kJ/mol higher at LAS1(101) than the corresponding barrier at Brønsted acid site

due to the entropic penalty of an additional water adsorption. Generally, the surface Lewis acid site has a rather insignificant role for the investigated reactions.

**Table 4.2:** Gibbs free energy barrier for surface Lewis acid site catalyzed reaction and corresponding reaction catalyzed by the Brønsted acid site localyzed inside the bulk at 400 °C. Values are given in kJ/mol. Reproduced from Ref. 217 with permission of RSC.

| Reaction | LAS1(101) | Brønsted acid site |
|---|---|---|
| B1-B2 | 270 | 243 |
| A1-E1 | 230 | 214 |
| C2-D1* | 261 | 252 |
| D1*-D3 | 254 | 237 |
| D4-D3 | 260 | 272 |
| E1-E2 | 141 | 155 |
| E4-E6* | 177 | 169 |
| E7*-E8 | 215 | 196 |
| E7-E8 | 177 | 185 |
| E8*-E10 | 305 | 153 |

## 4.5 Summary and Conclusion

I have investigated several possible reaction pathways for the conversion of acetic acid in H-SSZ-13 at 400 °C to isobutene, comprising the ketonic decarboxylation of acetic acid to 3-oxobutanoic acid, its decarboxylation to acetone, the aldol self-condensation of acetone to mesityl oxide, and the subsequent decomposition to isobutene. The C-C coupling of two acetic acid molecules proceeds most likely via a zeolite surface acetate and ketene with a barrier $\Delta G^{\ddagger} = 197\,\mathrm{kJ/mol}$, which is the highest barrier during the whole process. I additionally studied the role of a surface Lewis acid site for this process, but found a minor role for it. I performed a kinetic simulation using a batch reactor model, which reflects experimental studies (for other zeolites than H-SSZ-13). Most of the acetic acid is consumed fast and acetone is transitionally formed as a stable intermediate while subsequent isobutene formation proceeds more slowly. Thus, H-SSZ-13 in principle is capable to produce acetone or isobutene from acetic acid.

# 5

# Initiation of the Methanol-to-Olefins Process

*This chapter is based* on [Philipp Huber and Philipp N Plessow. The role of decarboxylation reactions during the initiation of the methanol-to-olefins process. *J. Catal.*, 428:115134, 2023]. *Additionally, content of* [Philipp Huber and Philipp N Plessow. A computational investigation of the decomposition of acetic acid in H-SSZ-13 and its role in the initiation of the MTO process. *Catal. Sci. Technol.*, 13(6):1905–1917, 2023] *is used for section 5.3.*

The zeolite-catalyzed methanol-to-olefins (MTO) process efficiently converts methanol to light olefins and can run in a sustainable fashion, since methanol can be obtained from renewable resources.[6,9] Thus, the MTO process provides an alternative to the utilization of fossil resources. The reaction network of this process is heavily intertwined and still not completely understood. In this chapter, the initiation mechanism of the MTO process is discussed, i.e., the formation of the first olefins via direct C-C coupling, which initiates the autocatalytic olefin cycle. For this, I will focus on mechanisms which include decarboxylation reactions, since the formation of $CO_2$ during the MTO process[97,130,136,137,139,140,142] cannot be explained so far. A detailed overview of the MTO process and its initiation mechanism is given in section 1.4. In section 5.1, I present a mechanism including the formation and decarboxylation of $\beta$-lactones to olefins and compare it to a previously computed mechanism comprising the decarbonylation of ketenes to olefins.[113] In section 5.2, I study an initiation mechanism comprising the formation of acrylic acid and subsequent decarboxylation to ethene. In these sections, only Gibbs free energy barriers are discussed, while kinetic simulations for a batch reactor model are evaluated in section 5.3 For this, the ketonic decarboxylation of acetic acid presented in chapter 4 is also considered. In section 5.4, I compare barriers for key reaction steps in H-SSZ-13, H-SAPO-34, and H-ZSM-5. Finally, a deactivation

mechanism proceeding through acrylic acid is discussed in section 5.5. For the free energies computed in this chapter, the methodology as outlined in section 2.5 was used. Periodic DFT energies corrected by ab initio calculations at cluster models at the CCSD(T) level of theory are used.

## 5.1 Decarboxylation of $\beta$-Lactones versus Decarbonylation of Ketenes in H-SSZ-13

Ketene and formaldehyde (FA) have often been proposed to play a crucial role in the initiation of the MTO process.[9,98,113,114,136,142,149,232] Both species are formed as reactive intermediates during the early stages of the process. While FA and ketene are especially important for the methane-formaldehyde and ketene mechanisms, respectively, coupling of FA with ketene has also been proposed as a possible initiation reaction.[136] Here, I study the coupling of ketene species with FA to $\beta$-lactones, which can decarboxylate to olefins and thus initiate the MTO process. Starting from ketene species, these reactions can be appropriately compared to the previous computed ketene mechanism, where olefins are formed from decarbonylation of ketenes.[113] This decarbonylation mechanism has been recomputed using the methodology presented in this work (CCSD(T) level of theory).

Before presenting this mechanism, I point to the interconversion of ketene derivatives in zeolites. Figures 5.1a and 5.1b show the mechanism and Gibbs free energy diagram for the interconversion of these derivatives. The acidic zeolite can protonate ketene as well as methylated ketene species to acylium cations. These unstable ions react further to zeolite surface esters which yield methyl esters after reaction with methanol. Up to three-fold methylated species exist for methyl esters, zeolite esters, and acylium cations, while up to two-fold methylated species exist for ketenes. In Table 5.1, the Gibbs free energy values corresponding to Fig. 5.1b are shown. The DFT free energy barrier of TS(SE1-AC1) referenced to AC1 is only 1 kJ/mol. After adding the cluster-model correction term, the free energy of TS(SE1-AC1) shifts to 18 kJ/mol below the free energy of AC1. Methyl esters, which in principle are easily formed with barriers below $\Delta G^{\ddagger} = 114$ kJ/mol, are very stable compared to the other intermediates during the MTO process and have to be considered as reference states when calculating barriers within the energetic span model.[185]

**Table 5.1:** List of DFT Gibbs free energies and cluster-model corrected Gibbs free energies (corresponding to Fig. 5.1) for the interconversion of methyl esters (ME), zeolite surface esters (SE), acylium cations (AC), and ketenes (K) considering different degree of methylation at 400 °C. Referenced to methyl esters. Reproduced from Ref. 116 with permission of Elsevier.

| State | $\Delta G$ (kJ/mol) | | | | $\Delta G_{\mathrm{DFT}}$ (kJ/mol) | | | |
|---|---|---|---|---|---|---|---|---|
| | 0 | 1 | 2 | 3 | 0 | 1 | 2 | 3 |
| ME | 0 | 0 | 0 | 0 | 0 | 0 | 0 | 0 |
| TS(ME-SE) | 164 | 153 | 145 | 174 | 141 | 130 | 121 | 148 |
| SE | 50 | 46 | 65 | 64 | 52 | 45 | 59 | 51 |
| TS(SE-AC) | 85 | 110 | 98 | 90 | 86 | 98 | 80 | 57 |
| AC | 103 | 88 | 90 | 84 | 85 | 78 | 66 | 51 |
| TS(AC-K) | 110 | 101 | 127 | - | 81 | 71 | 79 | - |
| K | 56 | 53 | 47 | - | 51 | 46 | 36 | - |

The reaction mechanism comparing decarboxylation via lactones and decarbonylation via ketenes is shown in Fig. 5.2a and the reference states of the methyl esters are shown in Fig. 5.2b. Progressing

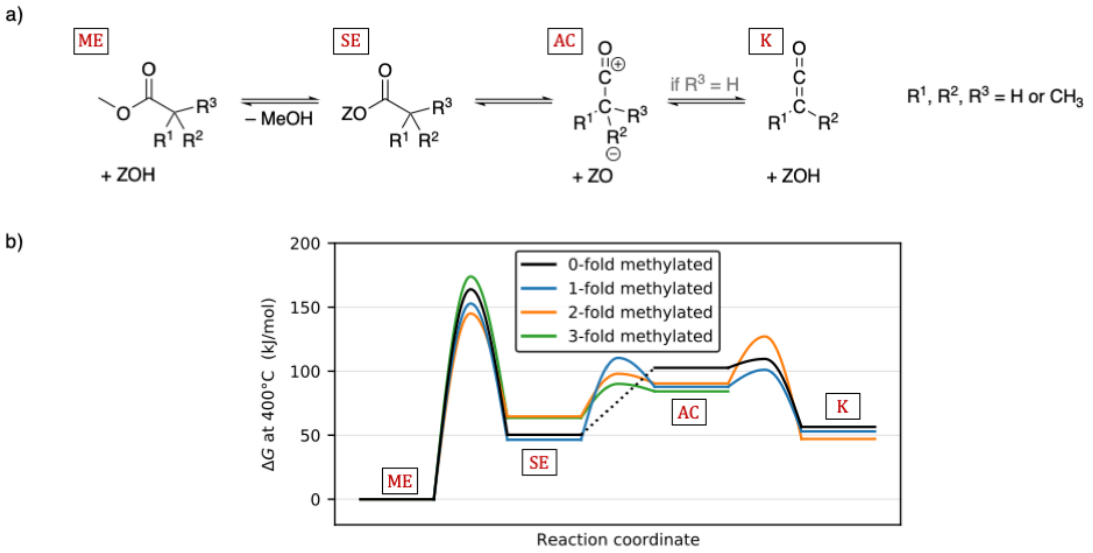


**Figure 5.1:** Mechanism a) and Gibbs free energy diagram b) for the interconversion of methyl esters, zeolite surface esters, acylium cations, and ketenes considering different degrees of methylation at 400 °C. Reference states are the gaseous methyl esters. Reproduced from Ref. 116 with permission of Elsevier.

methylation of ketenes yields methylketene, dimethylketene, and a trimethyl acylium cation (pivaloyl cation). The zero-fold, one-fold and two-fold methylated ketenes can react with formaldehyde to propiolactone (P1), 3-methyloxetan-2-one (P2), and pivalolactone (P3). These lactones subsequently decarboxylate to ethene, propene, and isobutene. Methylketene, dimethylketene, and the pivaloyl cation can be decarbonylated, which also yields ethene, propene, and isobutene. The decarbonylation path thereby requires one more methylation step to yield a specific olefin compared to the decarboxylation path. The Gibbs free energy diagram for these reactions is depicted in Fig. 5.2c and corresponding values are listed in Table A.8. Structures for the methylation and decarbonylation reactions have been taken and recomputed from previous studies of Plessow et al.[113] Methylation reactions of a ketene species proceed via SMS and actually yield the acylium cation (cf. TS(K1-K2) in Fig. 5.3). Since acylium cation, ketene, and zeolite surface ester are easily converted into each other, in Fig. 5.2 only the ketene species is depicted and in the Gibbs free energy diagram, the value of the most favorable of these states is used (cf. Table 5.1). For K1, K2, and K3, this is ketene, for K4, this is the zeolite surface acetate. The decarbonylation reactions actually start from the corresponding zeolite surface acetate instead of ketene. Furthermore, decarbonylation to ethene yields a zeolite ethoxy group in a first step, but the barrier of $\Delta G^{\ddagger} = 152\,\mathrm{kJ/mol}$ for the subsequent dissociation (not shown in Fig. 5.2) from the zeolite to ethene is low compared to the decarbonylation barrier. All barriers are referenced to the corresponding methyl ester, which are the preceding most stable states. The barrier for the last decarbonylation step (TS(K4-N3)) is lower than the barrier from ketene to the methyl ester (TS(SE4-ME4)) by 34 kJ/mol. For consistency, this barrier of $\Delta G^{\ddagger} = 140\,\mathrm{kJ/mol}$ is nevertheless referenced to the methyl ester (ME4). When referenced to the lowest previous state, which is a zeolite surface pivalate (SE4), this barrier is only $\Delta G^{\ddagger} = 76\,\mathrm{kJ/mol}$ The coupling reactions of ketenes with FA have low barriers and are neglected in the following discussion, but will be discussed later separately. Transition state structures of methylation of ketene, decarbonylation of methylketene, C-C coupling between ketene and FA, and decarboxylaton of propiolactone are shown in Fig. 5.3. These structures are equivalent for more highly methylated species.

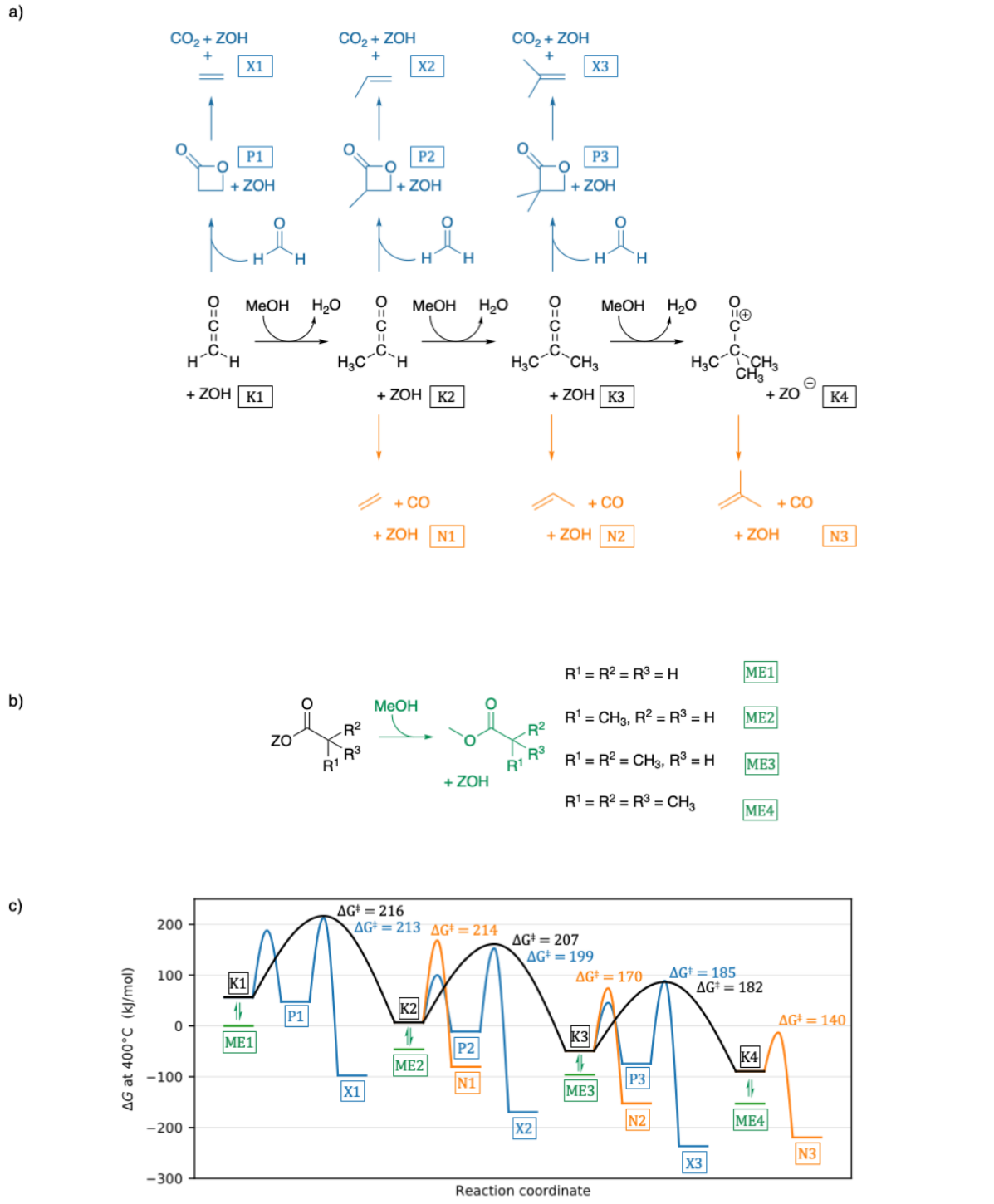


**Figure 5.2:** Mechanism for initiation of the MTO process via decarboxylation of lactones and decarbonylation of ketenes a) and for reactions to methyl esters b). Corresponding Gibbs free energy diagram c) at 400 °C. Reference states are the gaseous methyl esters. Reproduced from Ref. 116 with permission of Elsevier.

Proceeding now with the comparison of the decarbonylation and decarboxylation pathways, the decarboxylation from ketene to ethene has a barrier of $\Delta G^{\ddagger} = 213\,\mathrm{kJ/mol}$. The methylation to methylketene and subsequent decarbonylation have barriers of $\Delta G^{\ddagger} = 216\,\mathrm{kJ/mol}$ and $\Delta G^{\ddagger} = 214\,\mathrm{kJ/mol}$, respectively.

Although the decarboxylation has the lowest value, all three barriers are similar and corresponding deviations are within the error range of the applied method. Compared to decarbonylation to ethene, further methylation to dimethylketene and decarboxylation to propene is more favorable due to lower barriers of $\Delta G^{\ddagger} = 207\,\mathrm{kJ/mol}$ and $\Delta G^{\ddagger} = 199\,\mathrm{kJ/mol}$, respectively. The decarbonylation of dimethylketene to propene has a lower barrier of $\Delta G^{\ddagger} = 170\,\mathrm{kJ/mol}$. Methylation of dimethylketene to the pivaloyl cation and decarboxylation via dimethylketene to isobutene have slightly higher barriers of $\Delta G^{\ddagger} = 182\,\mathrm{kJ/mol}$ and $\Delta G^{\ddagger} = 185\,\mathrm{kJ/mol}$, respectively. The last barrier, decarbonylation to isobutene from pivaloyl cation, has a low barrier of $\Delta G^{\ddagger} = 140\,\mathrm{kJ/mol}$ ($\Delta G^{\ddagger} = 76\,\mathrm{kJ/mol}$, when referenced to zeolite surface pivalate). When following the heights of barriers, formation of ethene via decarboxylation would be most favorable. However, differences between the barriers of the pathways are partly very low. Neglecting decarboxylation reactions, following the heights of barriers leads to propene. Comparison of decarboxylation and decarbonylation to a specific olefin requires consideration of the previous methylation step for the latter. For the decarbonylation pathway, the previous methylation reaction is the rate-determining step. For example, starting from methylketene, decarboxylation to propene has a barrier of $\Delta G^{\ddagger} = 199\,\mathrm{kJ/mol}$, while decarbonylation to propene is controlled by the methylation step with a barrier of $\Delta G^{\ddagger} = 207\,\mathrm{kJ/mol}$ instead of the following lower barrier for decarbonylation of $\Delta G^{\ddagger} = 170\,\mathrm{kJ/mol}$. Generally, the decarboxylation path is slightly more favorable than the decarbonylation path.

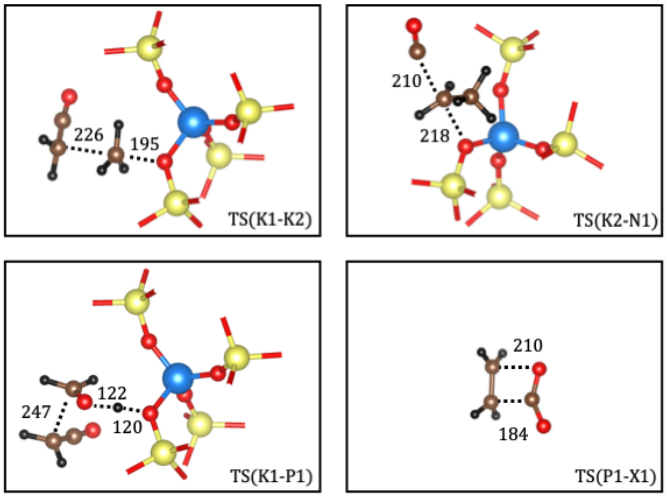


**Figure 5.3:** Important transition state structures during the initiation of the MTO process via decarboxylation of lactones and decarbonylation of ketenes. Reproduced from Ref. 116 with permission of Elsevier.

Now, specific reactions will be discussed in more detail. Several mechanisms for the formation of lactones were computed. Ketenes can first couple via C-C bond formation with FA, which simultaneously becomes protonated by the zeolite (cf. TS(K1-P1) in Fig. 5.3). Afterwards, the four-membered ring is built by C-O bond formation and the proton shifts back to the zeolite. The C-O bond formation can also precede the C-C coupling, whereby the zeolite's proton is involved in a hydrogen bond to the ketene. Depending on the corresponding lactone, these mechanisms proceed in one or two steps. In the one-step reaction, the corresponding second step proceeds without an additional barrier. Furthermore, this reaction can also take place in the gas phase (in absence of a catalyst). In Table 5.2 the corresponding barriers for the formation of the three lactones are shown. The barriers of the first mechanism, i.e., lactone formation initiated by C-C coupling, are by 85 kJ/mol to 142 kJ/mol lower than the barriers for the

other mechanisms. For P1 and P2, this mechanism is a step-wise reaction, whereby the C-C coupling is the rate-determining step with barriers of $\Delta G^{\ddagger} = 188\,\mathrm{kJ/mol}$ and $\Delta G^{\ddagger} = 146\,\mathrm{kJ/mol}$, while for P3, this mechanism proceeds in one step with a barrier of $\Delta G^{\ddagger} = 142\,\mathrm{kJ/mol}$. For the mechanism initiated by C-O bond formation, P1 and P2 are formed in one step, while formation of P3 is a step-wise reaction.

**Table 5.2:** Barriers for formation of lactones in kJ/mol referenced to the preceding methyl esters at 400 °C. Bold values are used in Fig. 5.2c. If no value is given for TS2, the reaction proceeds in one step.

| Reaction / Intermediate | | P1 | P2 | P3 |
|---|---|---|---|---|
| First C-C bond formation | TS1 | **188** | **146** | **142** |
| | TS2 | 149 | 114 | - |
| First C-O bond formation | TS1 | 296 | 276 | 223 |
| | TS2 | - | - | 284 |
| Gas phase reaction | | 273 | 278 | 267 |

The decarboxylation reactions of lactones can proceed catalyzed by the zeolite or uncatalyzed in the gas phase. During the catalyzed reaction, the keto group of the lactone forms a hydrogen bond to the zeolite's proton. For P1 and P2, the reaction is more favorable in the gas phase because of entropical contributions (cf. TS(P1-X1) in Fig. 5.3). Due to increasing dispersion energies for larger species, the decarboxylation of P3 is slightly more favorable when catalyzed by the zeolite.

**Table 5.3:** Barriers for decarboxylation of lactones in kJ/mol referenced to preceding methyl esters at 400 °C. Bold values are used in Fig. 5.2c.

| Reaction / Intermediate | P1 | P2 | P3 |
|---|---|---|---|
| Decarboxylation catalyzed | 231 | 203 | **185** |
| Decarboxylation gas phase | **213** | **199** | 188 |

The gas-phase decarboxylation of propiolactone was also studied experimentally, whereby an intrinsic barrier of $\Delta G^{\ddagger} = 157\,\mathrm{kJ/mol}$ at 400 °C was determined.[233] For the computed barrier referenced to propiolactone, a value of $\Delta G^{\ddagger} = 165\,\mathrm{kJ/mol}$ was obtained here, which differs only by 8 kJ/mol to the experimentally measured barrier.

## 5.2 Decarboxylation of Acrylic Acid in H-SSZ-13

Acrylic acid was proposed as an important intermediate during the initiation of the MTO process by the group of Lercher.[136] In H-ZSM-5, they detected methanol conversion to unsaturated carboxylates via infra-red spectroscopy and simultaneously $CO_2$ from desorption experiments before olefins were formed. From these findings, they proposed that FA reacts with a C2 compound to acrylic acid, which afterwards decarboxylates to ethene. In the following, I present reaction pathways comprising the coupling of formaldehyde with C2 compounds, which are ketene, acetic acid, and its enol. Free energy barriers again have to be referenced to the value for the state of the methyl acetate (in most cases). In Fig. 5.4a the mechanisms comprising the C-C coupling between FA and acetic acid or its enol are shown, and in Fig. 5.4b, the corresponding Gibbs free energy path is depicted.

Methyl acetate first reacts with a barrier of $\Delta G^{\ddagger} = 164\,\mathrm{kJ/mol}$ to a zeolite surface acetate, which is 50 kJ/mol higher in its free energy than the methyl ester. Hydration yields acetic acid with a barrier of

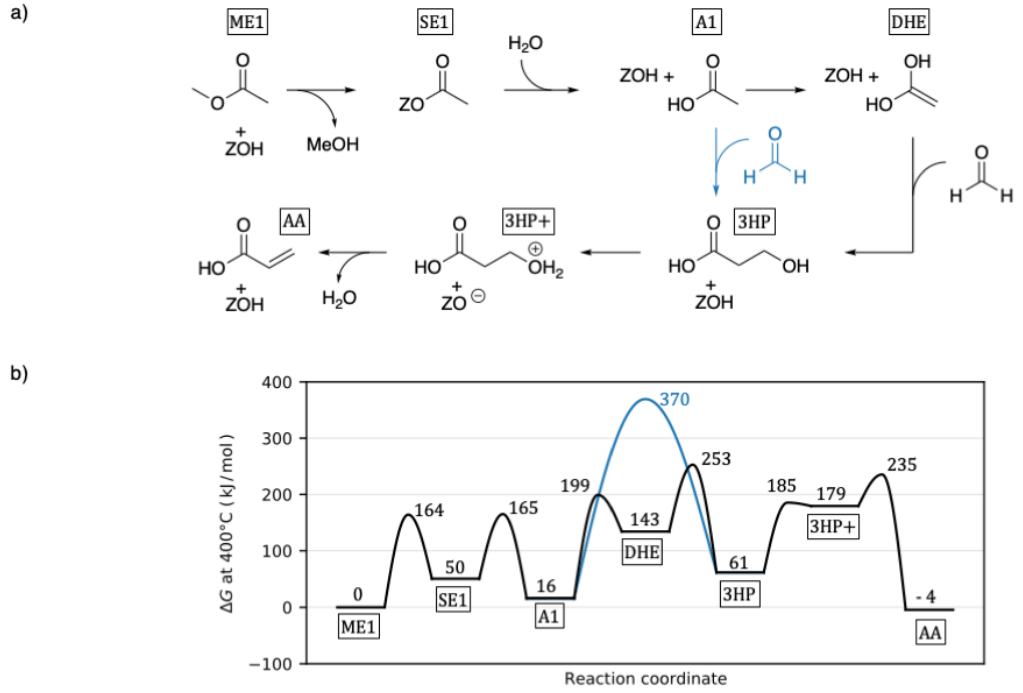


**Figure 5.4:** Additional mechanism a) and Gibbs free energy diagram at 400 °C b) for the formation and decarboxylation of acrylic acid from methyl acetate. Reference state is gaseous methyl acetate. Reproduced from Ref. 116 with permission of Elsevier.

$\Delta G^{\ddagger} = 165\,\mathrm{kJ/mol}$ and subsequent keto-enol tautomerization yields 1,1-dihydroxyethene with a barrier of $\Delta G^{\ddagger} = 199\,\mathrm{kJ/mol}$. The reactions between these C2 compounds already have been discussed in chapter 4. The nucleophilic carbon atom of the enol can react with FA to 3-hydroxypropanoic (3HP) acid with a high barrier of $\Delta G^{\ddagger} = 253\,\mathrm{kJ/mol}$. 3HP becomes protonated at its hydroxy group and dehydrates to acrylic acid with barriers of $\Delta G^{\ddagger} = 185\,\mathrm{kJ/mol}$ and $\Delta G^{\ddagger} = 235\,\mathrm{kJ/mol}$. The final state of adsorbed acrylic acid is by 4 kJ/mol lower than the reference state of methyl acetate. The adsorption free energy of acrylic acid is $-3\,\mathrm{kJ/mol}$. A direct C-C coupling between acetic acid and FA to 3HP is very unlikely with a barrier of $\Delta G^{\ddagger} = 370\,\mathrm{kJ/mol}$. A more favorable mechanism for the formation of acrylic acid is shown in Fig. 5.5a, where ketene reacts with FA.

As discussed before, zeolite surface acetate can react to ketene. Referenced to methyl acetate, this reaction has a small barrier of $\Delta G^{\ddagger} = 110\,\mathrm{kJ/mol}$. Ketene reacts with FA with barriers of $\Delta G^{\ddagger} = 188\,\mathrm{kJ/mol}$ and $\Delta G^{\ddagger} = 149\,\mathrm{kJ/mol}$ to propiolactone as explained in the previous section. Propiolactone can then further react to acrylic acid. First, the ketonic O-atom becomes protonated, leading to a ring opening again and a surface species is formed (SP1). Dissociation from the surface and deprotonation yields acrylic acid. The highest barrier during this process is $\Delta G^{\ddagger} = 205\,\mathrm{kJ/mol}$. Eventually, acrylic acid can be decarboxylated to ethene with a barrier of $\Delta G^{\ddagger} = 235\,\mathrm{kJ/mol}$. However, the decarboxylation of propiolactone is more favorable with a barrier of $\Delta G^{\ddagger} = 217\,\mathrm{kJ/mol}$ (referenced to acrylic acid). While the barrier for decarboxylation is by 14 kJ/mol higher for acrylic acid than for propiolactone (both referenced to acrylic acid), the barrier for formation of acrylic acid is more favorable by 12 kJ/mol than the decarboxylation of propiolactone (both referenced to methyl acetate). Hence, acrylic acid in principle can be formed before ethene and $CO_2$ are released via propiolactone. This finding is in agreement with experimentally detected acrylic acid during the MTO process.[136]

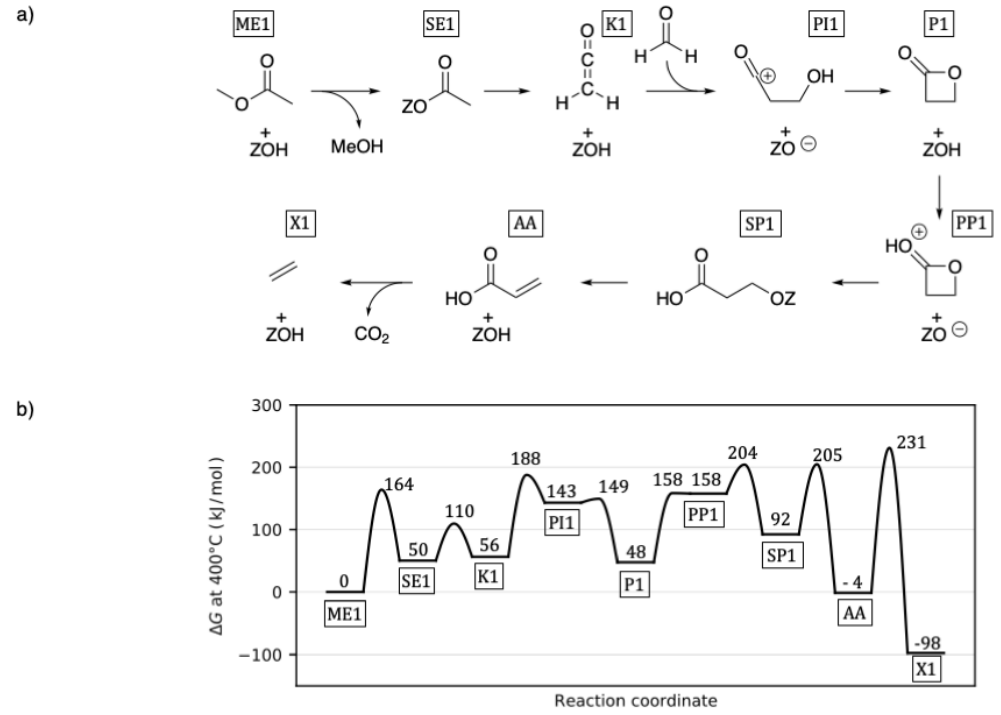


**Figure 5.5:** Mechanism a) and Gibbs free energy diagram at 400 °C b) for the formation and decarboxylation of acrylic acid from methyl acetate. Reference state is gaseous methyl acetate. Reproduced from Ref. 116 with permission of Elsevier.

## 5.3 Kinetic Simulations in H-SSZ-13

While comparing free energy barriers allows qualitative statements to be made regarding the relevance of competing mechanisms, kinetic simulations enable a more quantitative analysis. I applied simulations for a kinetic batch reactor model at 400 °C (see section 2.4 for details). Reaction barriers computed here are only related to the initiation mechanisms of the MTO process starting from ketene and its derivatives. Elementary steps for the conversion of methanol to ketene as well as for the decarbonylation mechanism already have been computed in another work (cf. Table A.9)[113] and are taken from there (for details of this mechanism see section 1.4). The same applies for the methylation and cracking reactions (cf. Table A.10 and A.11) within the autocatalytic olefin cycle taking place after initiation of the MTO process.[76] These barriers have been computed with the same methodology applied here, but used cluster-model corrections at the MP2 level of theory instead of CCSD(T). The average difference between both methods was found to be less than 10 kJ/mol.[166] A corresponding kinetic simulation for a batch reactor model was already conducted previously.[114] Reaction steps from the decarbonylation mechanism have been recomputed with the methodology applied in this work (CCSD(T) level of theory). Four different initiation mechanisms from ketene to olefins will be discussed in the following; the ketonic decarboxylation of acetic acid (cf. chapter 4), the decarbonylation of ketenes, the decarboxylation of $\beta$-lactones, and the decarboxylation of acrylic acid. The barriers used in the kinetic simulation are listed in Tables A.7 and A.9 to A.12.

Competing mechanisms can be compared by evaluating each mechanism's overall rate from a separate simulation. The following mechanisms have been considered in each of the following kinetic simulations:

- Reactions from methanol to ketene[113]
- One of the following mechanisms:
  - Initiation via ketonic decarboxylation of acetic acid
  - Initiation via decarbonylation of ketene species to olefins
  - Initiation via decarboxylation of $\beta$-lactones
  - Initiation via decarboxylation of acrylic acid
- Methylation and cracking reactions of the autocatalytic olefin cycle[76]

For comparing the rates, I defined an initiation time corresponding to a pressure of 0.005 bar of olefins formed. Before going into details, the initiation times for the different initiation mechanisms are listed in Table 5.4. Considering only initiation mechanisms through decarbonylation of ketenes or decarboxylation of $\beta$-lactones, similarly short initiation times of 8.80 s and 8.87 s are obtained. While the initiation time for the mechanism through decarboxylation of acrylic acid with 10.64 s is slightly higher and the initiation time for the mechanism through ketonic decarboxylation of acetic acid with 18.45 s is significantly higher.

**Table 5.4:** Initiation times considering different initiation mechanisms for the MTO process.

| Initiation mechanism | Initiation time / *s* |
|---|---|
| ketonic decarboxylation of acetic acid | 18.45 |
| decarbonylation of ketenes | 8.80 |
| decarboxylation of $\beta$-lactones | 8.87 |
| decarboxylation of acrylic acid | 10.64 |

The kinetic simulations will be discussed in more detail now, starting with the ketonic decarboxylation of acetic acid. In chapter 4, I presented the ketonic decarboxylation of acetic acid to acetone via 3-oxobutanoic acid and subsequent aldol self-condensation of acetone to mesityl oxide, which afterwards decomposes to isobutene. This mechanism in principle can initiate the MTO process as also proposed by the group of Lercher,[136] since acetic acid can be formed from methanol in zeolites (through hydration of ketene, methyl acetate, or zeolite surface acetate) and isobutene enters the autocatalytic olefin cycle. Hence, a kinetic simulation was conducted using the mechanism through ketonic decarboxylation of acetic acid for the path from ketene to olefins. Figure 5.6 shows DME, MeOH, $H_2O$, and olefin pressures of this simulation for a methanol input of 1 bar.

The methanol pressure immediately decreases and DME and water are formed within 5 s. Up to the initiation time, i.e., up to the initiation of the autocatalytic cycle, the olefin pressure increases slowly and afterwards rapidly to 0.2 bar. Accompanying this, the methanol pressure drops to 0 bar and the water pressure increases to 1 bar. The qualitative behavior of these pressures, including the small peak of methanol during the start of the break through of the olefins, is in accordance with experimental results.[6,9] The maximum pressure of $CO_2$ and acetone formed during a simulation time of 30 s is present at the end of the simulation with only $6 \cdot 10^{-19}$ bar and $1.5 \cdot 10^{-11}$ bar, respectively. The majority of acetone is not formed from decarboxylation of 3-oxobutanoic acid, but from the backward reaction via isobutene of the hydrocarbon pool. Comparing the initiation times of this mechanism through ketonic decarboxylation (18.45 s) and the decarbonylation mechanism (8.80 s), the former can be considered to play a minor role for the MTO process. Referenced to methyl acetate, the rate-determining step, which

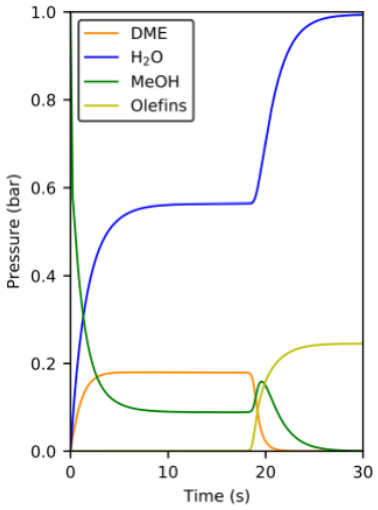


**Figure 5.6:** Kinetic simulations of the initiation mechanism proceeding via acetone at 400 °C using 1 bar methanol as feedstock. Only gas phase species are shown. Reproduced from Ref. 217 with permission of RSC.

is the C-C coupling between a ketene and a zeolite surface acetate, for the ketonic decarboxylation has a barrier of $\Delta G^{\ddagger} = 213\,\mathrm{kJ/mol}$. This is similar to the rate-determining step of the decarbonylation mechanism (methylation of ketene to methylketene) with a barrier of $\Delta G^{\ddagger} = 216\,\mathrm{kJ/mol}$. However, ketene derivatives are present in very low concentrations only during the MTO process. The C-C coupling between two ketene derivatives thus is a reaction of two species present in low concentrations, while the methylation of ketene requires only one species present in low concentration. Hence, the decarbonylation mechanism is intrinsically favored over the ketonic decarboxylation mechanism.

Next, I analyze the role of decarboxylation of lactones and of acrylic acid for the MTO process. Instead of a second ketene derivative, these mechanisms require an FA molecule, which is present in higher concentrations than ketene. I made two additional kinetic simulations considering only one of these mechanisms for the initiation path between ketene and olefins (barriers: cf. Table A.9-A.12). These have initiation times of 8.87 s (decarboxylation via lactones) and 10.64 s (decarboxylation via acrylic acid), respectively. Compared to the initiation time considering the decarbonylation mechanism only (8.80 s), at least the decarboxylation of lactones (8.87 s) might be relevant for the initiation of he MTO process and might explain experimentally detected $CO_2$. The role for decarboxylation of acrylic acid in contrast has a minor role (maximum pressure of acrylic acid formed during this simulation is only $2 \cdot 10^{-13}$ bar).

Furthermore, I simulated a process taking the decarbonylation mechanism as well as the mechanism involving decarboxylation of lactones and decarboxylation of acrylic acid into account, which has an initiation time of 8.72 s. DME, MeOH, $H_2O$, and olefin pressures of this simulation are shown in Fig. 5.7a. The progression of pressures is similar to Fig. 5.6, but only the initiation time differs. Pressures of FA, CO, and $CO_2$ formed during the simulation are very low, as is shown in Fig. 5.7b. The CO pressure is significantly higher than the $CO_2$ pressure; however, this is no indication towards a domination by the decarbonylation mechanism. In the initiation process, CO is first formed from methanol via methyl formate (cf. Fig. 1.9). For the decarbonylation pathway, CO is then catalytically consumed for ketene formation and eventually released during decarbonylation. Thus, the pressure of CO originates from

processes taking place before the decarbonylation of ketenes. $CO_2$ in contrast is only released during the decarboxylation process and its pressure can therefore be used to quantify the relevance of corresponding mechanisms.

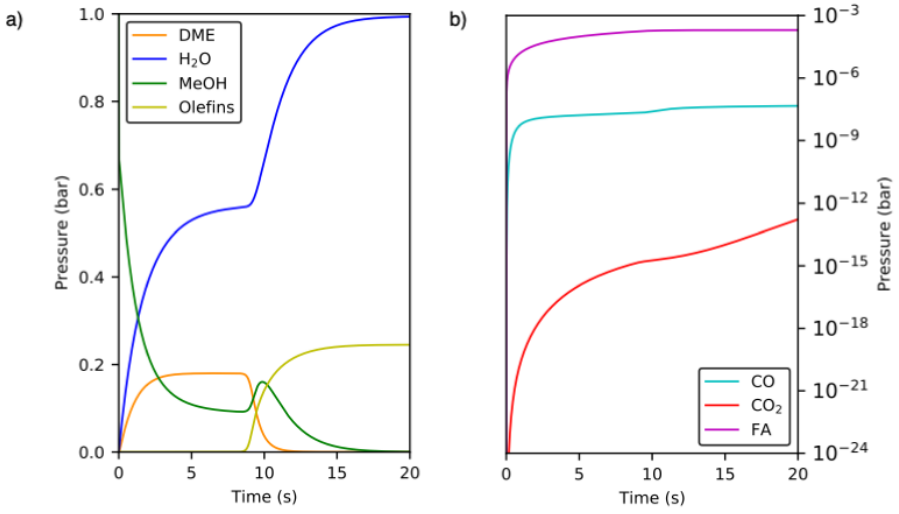


**Figure 5.7:** Kinetic simulations of the initiation mechanism proceeding via decarboxylation of lactones, decarboxylation of acrylic acid and decarbonylation of ketenes at 400 °C using 1 bar methanol as feedstock. Only gas phase species are shown. Pressures of DME, $H_2O$, MeOH, and olefins a), and pressures of CO, $CO_2$, and FA (logarithmic scale) b) are depicted. Reproduced from Ref. 116 with permission of Elsevier.

The amount of FA formed during the simulation is significantly lower than observed in experiments, where several percentage points of FA selectivity were determined for low methanol conversions in H-ZSM-5.[136,141] The group of Lercher, for example, obtained an FA selectivity of 25 % for a MeOH/DME conversion of 0.24 % in H-ZSM-5 at 475 °C. For a simulation in H-SSZ-13 at 400 °C, I obtain an FA selectivity of only $4 \cdot 10^{-5}$ % for a MeOH conversion of 0.25 %. Therefore, I applied additional simulations with varying pressures for FA used as co-feed to 1 bar methanol. In Fig. 5.8a, the pressures for $CO_2$ and CO formed up to the initiation time for a given co-feed of FA are depicted. The initiation time of 8.72 s without co-feed is reduced to 6.56 s for a co-feed of 0.3 bar FA. Corresponding pressures of CO and $CO_2$ increase from $2 \cdot 10^{-8}$ bar and $1 \cdot 10^{-15}$ bar to $2 \cdot 10^{-5}$ bar and $1 \cdot 10^{-9}$ bar, respectively. The corresponding quotient of $p(CO_2)/p(CO_2)$ increases from $6 \cdot 10^{-8}$ bar to $6 \cdot 10^{-5}$ bar. While the total pressure of CO allows no statement regarding the relevance for the competitive decarbonylation mechanism, the increasing value for $p(CO_2)/p(CO_2)$ with increasing co-feed of FA shows that this co-feed clearly favors the decarboxylation pathway. In addition to the FA pressure, the pressure of CO predicted by the simulation is also lower than observed in experiments. Kirchberger et al. observed selectivities of about 0.02 % $CO_2$, 0.08 % CO, and 0.06 % FA from 0.33 % DME conversion in H-ZSM-5 at 475 °C.[142] Reflecting these conditions, I used a co-feed of 0.8 mbar CO and 0.6 mbar FA to 1 bar DME (at 400 °C). $2 \cdot 10^{-18}$ bar $CO_2$ is formed at a DME conversion of 0.33 % and $1 \cdot 10^{-10}$ bar $CO_2$ is formed up to the initiation time. I further varied the FA and CO pressures with $p(\mathrm{FA}) = p(\mathrm{CO})$ as co-feed to 1 bar methanol for additional simulations. The corresponding pressures of $CO_2$ formed up to the initiation time are shown in Fig. 5.8b. For a co-feed of $p(\mathrm{FA}) = p(\mathrm{CO}) = 0.3$ bar, the initiation time is decreased to 4.87 s and the pressure of $CO_2$ formed up to this time is $1 \cdot 10^{-5}$ bar. All in all, the mechanism comprising the decarboxylation reactions of lactone can initiate the MTO process with

similar rates to the decarbonylation mechanism, while significantly higher pressures of $CO_2$ are formed in experiments than predicted by the kinetic simulations.

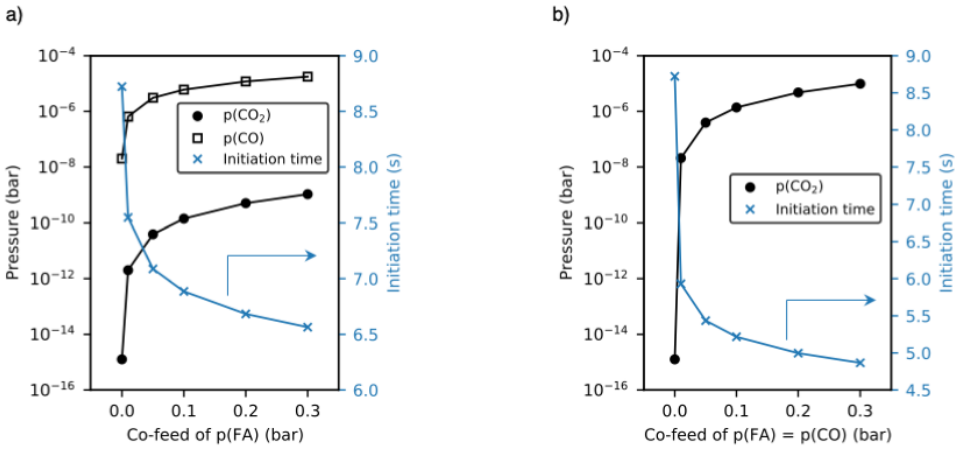


**Figure 5.8:** Kinetic simulations of the initiation mechanism proceeding via decarboxylation of lactones and decarbonylation of ketenes at 400 °C. Varying pressures of FA a) and of FA and CO with p(FA) = p(CO) b) as co-feed to 1 bar at 400 °C. Pressures of CO and $CO_2$ are given at the initiation time. Reproduced from Ref. 116 with permission of Elsevier.

## 5.4 Comparison of H-SSZ-13, H-SAPO-34, and H-ZSM-5

So far, I considered the H-SSZ-13 zeolite only due to its simple structure leading to efficient computations. For industrial applications, zeotypes like H-ZSM-5 and H-SAPO-34 are more relevant and will be discussed in the following. For these two zeotypes, Gibbs free energy barriers for key reaction steps were computed to compare the decarbonylation mechanism with the decarboxylation mechanism (via lactones). While the CHA structure of H-SSZ-13 and H-SAPO-34 has only one unique T-site, the MFI framework of H-ZSM-5 has twelve distinguishable T-sites. Previous studies suggest the T12-site to be the most important,[21,234] which is the only MFI T-site considered here. Barriers for the decarbonylation of ketenes, decarboxylation of lactones, and methylation of ketenes are used in a parity plot (Fig. 5.9), where the DFT free energy barriers as well as the cluster-model corrected free energy barriers of H-SSZ-13 are compared to those of H-SAPO-34 and H-ZSM-5. The values used for the parity plot are listed in Table 5.5. Barriers for the catalyzed decarboxylation are very similar for all three zeotypes. Barriers for methylation and decarbonylation reactions are about 10 kJ/mol to 20 kJ/mol higher in H-SAPO-34 and about 10 kJ/mol to 20 kJ/mol lower in H-ZSM-5 compared to those of H-SSZ-13. This correlation can be taken from pure DFT free energies as well as for corresponding cluster-model corrected barriers. The barrier for the uncatalyzed decarboxylation reaction to ethene in H-SAPO-34 is by 23 kJ/mol lower than the barrier for the rate-determining step of the decarbonylation mechanism. In H-ZSM-5, the barrier for the rate-determining step of the decarbonylation mechanism is 11 kJ/mol lower than the barrier of the competing decarboxylation reaction. Thus, the decarboxylation mechanism is in H-SAPO-34 more and in H-ZSM-5 less important compared to H-SSZ-13 when referring to barriers of these key reaction steps.

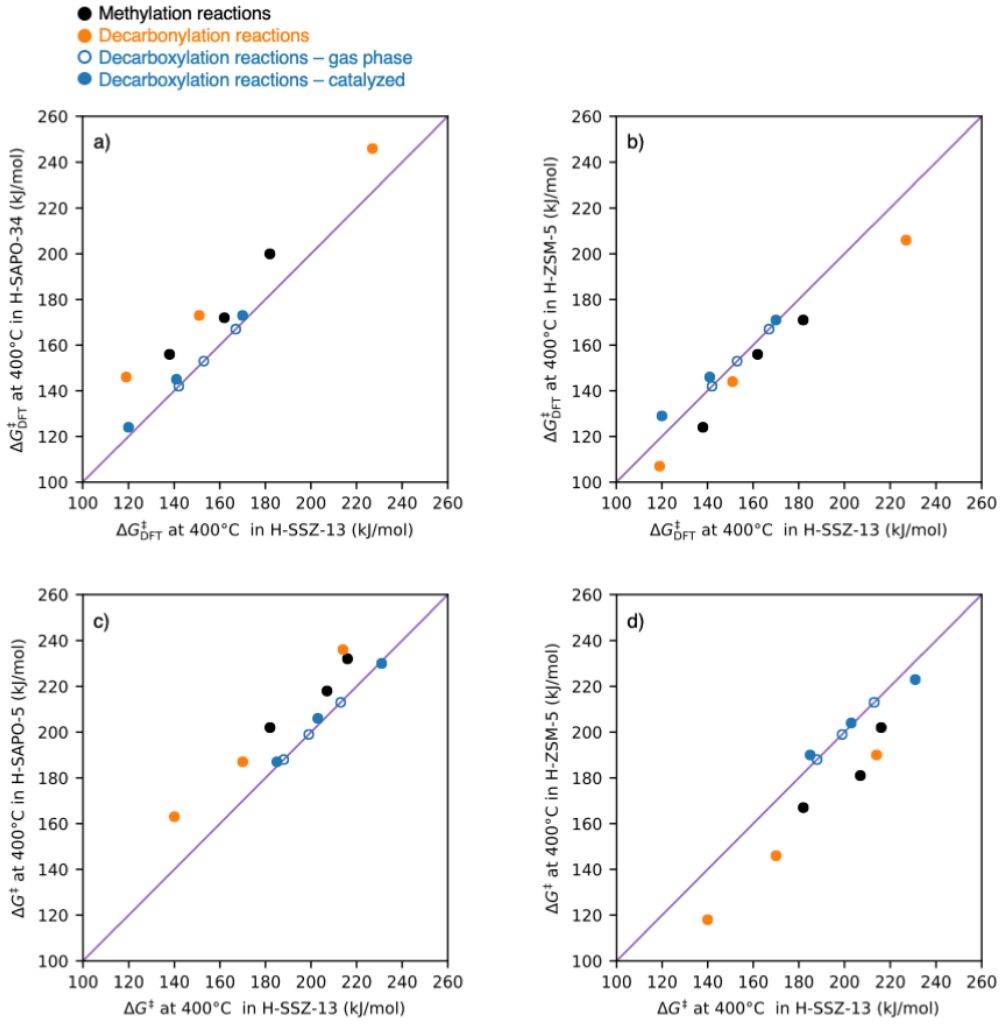


**Figure 5.9:** Parity plot for DFT barriers in H-SSZ-13 and H-SAPO-34 a) and in H-SSZ-13 and H-ZSM-5 b) at 400 °C. Cluster-model corrected barriers in H-SSZ-13 and H-SAPO-34 b) and in H-SSZ-13 and H-ZSM-5 d) at 400 °C. Gaseous methyl esters were used as reference states. Reproduced from Ref. 116 with permission of Elsevier.

**Table 5.5:** Cluster-model corrected Gibbs free energy barriers in H-ZSM-5, H-SAPO-34, H-SSZ-13, and in the gas phase at 400 °C referenced to methyl esters. DFT free energy barriers are also given in parenthesis.

| Reaction | Reactant | H-ZSM-5 | H-SAPO-34 | H-SSZ-13 | gas phase |
|---|---|---|---|---|---|
| | | Methylation of ketenes | | | |
| TS(K1-K2) | ($OCCH_2$) | 202 (171) | 232 (200) | 216 (182) | - |
| TS(K2-K3) | ($OCCHCH_3$) | 181 (156) | 218 (172) | 207 (162) | - |
| TS(K3-K4) | ($OCC(CH_3)_2$) | 167 (124) | 202 (156) | 182 (138) | - |
| | | Decarboxylation of lactones | | | |
| TS(P1-X1) | ($OC_3H_4$) | 223 (171) | 230 (173) | 231 (170) | 213 (167) |
| TS(P2-X2) | ($OC_3H_3CH_3$) | 204 (146) | 206 (145) | 203 (141) | 199 (154) |
| TS(P3-X3) | ($OC_3H_3(CH_3)_2$) | 190 (129) | 187 (124) | 185 (120) | 188 (121) |
| | | Decarbonylation of ketenes | | | |
| TS(K2-N1) | ($OCCHCH_3$) | 190 (206) | 236 (246) | 214 (227) | - |
| TS(K3-N2) | ($OCC(CH_3)_2$) | 146 (144) | 187 (173) | 170 (151) | - |
| TS(K4-N3) | ($OCC(CH_3)_3^+$) | 118 (107) | 163 (146) | 140 (119) | - |

## 5.5 Deactivation Mechanisms via Acrylic Acid in H-SSZ-13

FA and FA-derived species are believed to play a critical role for catalyst deactivation.[235,236] Since FA is formed during the initiation of the MTO process, deactivation mechanisms might proceed through intermediates formed at the early stage of this process. Lercher and coworkers suggest that the catalyst deactivation can occur through two kinds of coke, which deactivate the zeolite's catalytic function.[236] First, coke species can block the Brønsted acid sites by formation of strong chemical bonds. Second, bulky coke species are formed, which clog the pores of the zeolite. They proposed a deactivation mechanism starting from acrylic acid and formaldehyde reacting to hydroxyfuran. This aromatic compound subsequently reacts with ethene to phenol. This path contains intermediates with hydroxy groups, which could react with the acid site by dehydration, forming a chemical bond to the zeolite and thereby blocking its catalytic function. Moreover, aromatics deactivate the zeolite by clogging its pores.[96] I computed a reaction path from acrylic acid to phenole to analyze its role for catalyst deactivation. In Fig. 5.10 and 5.11, I show the mechanism and the corresponding Gibbs free energy diagram, respectively. Acrylic acid reacts with FA to 4-hydroxyisocrotonic acid with a high barrier of $\Delta G^{\ddagger} = 285\,\mathrm{kJ/mol}$. Dehydration yields 2(5H)-furanone and keto-enol tautomerization leads to hydroxyfuran with barriers of $\Delta G^{\ddagger} = 191\,\mathrm{kJ/mol}$ and $\Delta G^{\ddagger} = 135\,\mathrm{kJ/mol}$. Subsequent Diels-Alder reaction with ethene has a barrier of $\Delta G^{\ddagger} = 265\,\mathrm{kJ/mol}$ and yields 1,2-dihydroquinol after additional steps with a maximum barrier of $\Delta G^{\ddagger} = 183\,\mathrm{kJ/mol}$. Phenol can then be formed through dehydration with a barrier of $\Delta G^{\ddagger} = 113\,\mathrm{kJ/mol}$. This mechanism, especially the C-C coupling and the Diels-Alder reaction, has high barriers and thus is unlikely to take place.

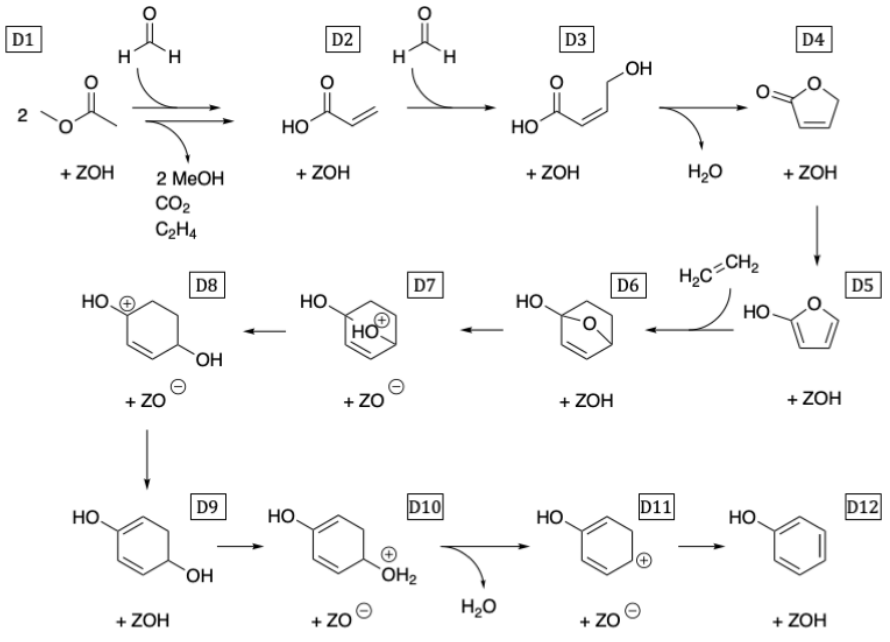


**Figure 5.10:** Deactivation mechanism proceeding through acrylic acid to phenole. Reproduced from Ref. 116 with permission of Elsevier.

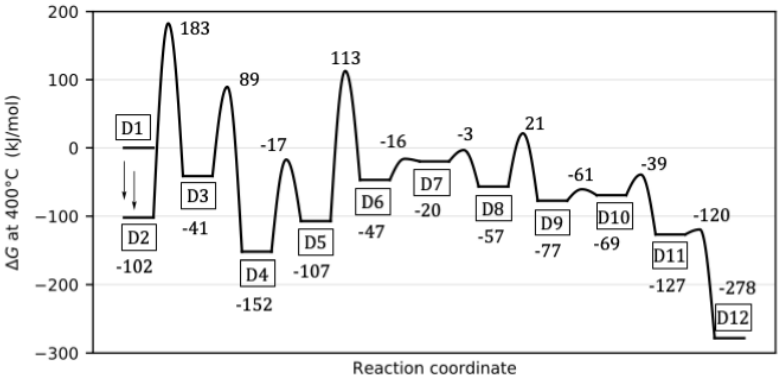


**Figure 5.11:** Gibbs free energy diagram for the deactivation mechanism proceeding through acrylic acid to phenole at 400 °C. Reproduced from Ref. 116 with permission of Elsevier.

## 5.6 Summary and Conclusion

To understand the origin of experimentally detected $CO_2$ during the MTO process, I computed corresponding initiation mechanisms involving decarboxylation reactions for the H-SSZ-13 zeolite at 400 °C. A mechanism proceeding through formation and decarboxylation of acrylic acid is unlikely due to a high decarboxylation barrier of $\Delta G^{\ddagger} = 235\,\mathrm{kJ/mol}$. I found a mechanism proceeding via decarboxylation of $\beta$-lactones to be more likely with a rate-determining barrier of $\Delta G^{\ddagger} = 217\,\mathrm{kJ/mol}$ (referenced to acrylic acid). Analyzing Gibbs free energy barriers, formation of acrylic acid, which was experimentally observed during the MTO process, nevertheless seems plausible, since it has a lower barrier ($\Delta G^{\ddagger} = 205\,\mathrm{kJ/mol}$) than those for the decarboxylation via lactones. However, acrylic acid was formed in negligible amounts only in a corresponding kinetic simulation for a batch reactor model. The mechanism proceeding via decarboxylation of lactones in contrast might explain the experimentally observed $CO_2$. This mechanism has slightly lower barriers than a previous computed initiation mechanism proceeding via decarbonylation of ketenes. The rate-determining steps for these barriers are $\Delta G^{\ddagger} = 213\,\mathrm{kJ/mol}$ and $\Delta G^{\ddagger} = 216\,\mathrm{kJ/mol}$ for the decarboxylation and decarbonylation mechanism, respectively, referenced to methyl acetate. While a kinetic simulation indeed determined a significant role of decarboxylation reactions via lactones, only low pressures of $CO_2$ are formed. This can be explained partly by prediction of too low pressures for FA and CO during the simulation compared to experiments. Additionally, I computed important reaction steps for the H-ZSM-5 and H-SAPO-34 zeotypes. Barriers for decarboxylation of lactones are similar for all three zeotypes. Barriers for decarbonylation and methylation reactions of ketenes are higher for H-SAPO-34 and lower for H-ZSM-5 compared to H-SSZ-13.

# 6

# Conclusion

In this work, I investigated acid sites and reaction mechanisms in zeolites to broaden our knowledge of their complex behavior in catalysis. I focused on three insufficiently understood topics, namely zeolite surface acid sites, conversion of acetic acid to acetone and isobutene, and the initiation mechanism of the MTO process.

There is still uncertainty about the structure of Lewis acid sites (LASs) in zeolites. At zeolite surfaces, which become increasingly relevant for small zeolite crystals, well-defined LAS motifs are expected to form. In chapter 3, I studied Brønsted acid sites (BASs) and LASs located at the surface of the H-SSZ-13 zeolite to capture the reactivity of LASs as well as to compare the reactivities of zeolite surfaces and bulk. First, I investigated the stabilities of purely siliceous H-SSZ-13 surfaces and found that they mainly depend on their number of silanol groups per surface area. The (101) facet is the most stable surface and thus was used for further studies. I additionally considered the (001) surface to discuss the influence of different facets. At these two surfaces, BASs and LASs were modeled and their stabilities were studied by also considering adsorbates. BASs located at the surface were found to be similarly stable as the BAS inside the zeolite bulk, differing on average by 7 kJ/mol. Especially in the presence of $H_2O$, LASs become more stable than BASs above temperatures of about 150 °C. Thus, the formation of LASs is thermodynamically likely during zeolite synthesis. The reactivity of the acid sites has been tested by using the step-wise and concerted dehydration of methanol to DME as a probe reaction. The BASs at the surface have similar barriers as the BAS inside the bulk, where the concerted mechanism is less important. Dehydration of methanol at LASs is similar to the concerted DME formation at BASs with respect to the mechanism and barriers. Consequently, their role for methanol dehydration is insignificant; however, they might be more important for other reactions. In this work, I have introduced

a methodology to computationally explore zeolite surface acid sites that can serve as a foundation for future investigations.

In chapter 4, I investigated the mechanism for conversion of acetic acid to acetone and further to isobutene in H-SSZ-13 at 400 °C. This process provides a sustainable alternative to the cumene process for the production of acetone. However, mechanistic details are still debated. The reaction starts with interconversion of acetic acid to other C2 compounds. The rate-determining step for the overall process is the C-C coupling of two acetic acid derivatives to 3-oxobutanoic acid. I studied several pathways for this reaction and found the lowest barrier of $\Delta G^{\ddagger} = 197\,\mathrm{kJ/mol}$ for a path involving the reaction of ketene with a zeolite surface acetate, which both can be formed from acetic acid. A kinetic simulation including several paths for C-C coupling reactions also showed that this path is the most important. The formed 3-oxobutanoic acid is easily decarboxylated to acetone with a barrier of $\Delta G^{\ddagger} = 155\,\mathrm{kJ/mol}$. The aldol self-condensation of acetone to mesityl oxide and further decomposition to isobutene has higher barriers again with a maximum value of $\Delta G^{\ddagger} = 185\,\mathrm{kJ/mol}$. Acetone is more stable than acetic acid and thus formed as a stable intermediate. The kinetic simulation reproduces experimental observations and also shows that acetone is transitionally formed in high concentration before reacting further to isobutene. This research provides new insights into the reactivity of acetic acid in zeolites by unraveling the reaction mechanisms from acetic acid to acetone and further to isobutene in H-SSZ-13.

In chapter 5, I investigated the initiation of the MTO process, i.e., the formation of the first olefins through direct C-C coupling, by comparing Gibbs free energy barriers of competing reaction pathways and by kinetic simulations. Experimentally, $CO_2$ was observed during the MTO process, which cannot be explained by previously computed mechanisms. The conversion of acetic acid to isobutene releasing $CO_2$ can in principle initiate the MTO process, but kinetic simulations in H-SSZ-13 indicate a minor importance of this pathway. A mechanism proceeding through decarboxylation of $\beta$-lactones, in contrast, can initiate the MTO process in H-SSZ-13 equally efficiently as a previously computed mechanism including decarbonylation reactions of ketenes. The rate-determining steps at 400 °C for the formation of olefins through decarboxylation and decarbonylation have barriers of $\Delta G^{\ddagger} = 213\,\mathrm{kJ/mol}$ and $\Delta G^{\ddagger} = 216\,\mathrm{kJ/mol}$, respectively. However, the amount of $CO_2$ formed during a kinetic simulation is significantly lower than observed experimentally. This can be partly explained by lower amounts of precursors (CO and formaldehyde) formed in the simulation than in the experiment. I additionally computed barriers for key reaction steps of the decarboxylation mechanism via lactones and the decarbonylation mechanism via ketenes in the H-SAPO-34 and H-ZSM-5 zeotypes. In all three zeotypes, the decarboxylation barriers are similar. Compared to H-SSZ-13, the barriers of the decarbonylation mechanism are higher in H-SAPO-34 and lower in H-ZSM-5, suggesting that decarboxylation reactions might play a more important role for H-SAPO-34.

In summary, I introduced a methodology to systematically evaluate the stabilities of zeolite surfaces, the stabilities of zeolite surfaces acid sites, and their reactivities. For the first time, zeolite surface reactivities were studied. I unraveled the mechanism for conversion of acetic acid to acetone and subsequently to isobutene in H-SSZ-13. This is a further step towards sustainable acetone production. Finally, I broadened our understanding of the MTO process by proposing a mechanism for $CO_2$ formation.

# A Appendix

**Table A.1:** Zero-point vibration energy corrected adsorption energies and Gibbs free energies at 200°C and 400°C for MeOH and DME in H-SSZ-13. Values are given in kJ/mol. For BASs, values for adsorption at all Oxygen within the active center are given.

| System | MeOH | | | | DME | | | |
|---|---|---|---|---|---|---|---|---|
| | O1 | O2 | O3 | O4 | O1 | O2 | O3 | O4 |
| | | | | E + ZPVE | | | | |
| BASB | -91 | -65 | -82 | -65 | -90 | -80 | -83 | -85 |
| BAS1(001) | -83 | -70 | -81 | -78 | -81 | -70 | -76 | -88 |
| BAS2(001) | -90 | -73 | -78 | -73 | -86 | -78 | -72 | -84 |
| BAS1(101) | -77 | -82 | -81 | -64 | -69 | -73 | -79 | -72 |
| BAS2(101) | -64 | -86 | -57 | -70 | -79 | -87 | -66 | -76 |
| LAS1(001) | | -158 | | | | -169 | | |
| LAS2(001) | | -154 | | | | -143 | | |
| LAS1(101) | | -148 | | | | -163 | | |
| | | | | $G$ (200) | | | | |
| BASB | -16 | 5 | -1 | 6 | -18 | -4 | -3 | -13 |
| BAS1(001) | -6 | 5 | -2 | 0 | -4 | 4 | 0 | -14 |
| BAS2(001) | -12 | 3 | 2 | 3 | -6 | -4 | 2 | -14 |
| BAS1(101) | 4 | -6 | -7 | 11 | 6 | -1 | -5 | 6 |
| BAS2(101) | 14 | -7 | 16 | 6 | 0 | -11 | 2 | -0 |
| LAS1(001) | | -81 | | | | -93 | | |
| LAS2(001) | | -74 | | | | -70 | | |
| LAS1(101) | | -74 | | | | -89 | | |
| | | | | $G$ (400) | | | | |
| BASB | 16 | 34 | 33 | 36 | 11 | 27 | 29 | 17 |
| BAS1(001) | 27 | 37 | 32 | 33 | 27 | 35 | 32 | 16 |
| BAS2(001) | 21 | 34 | 36 | 35 | 26 | 26 | 33 | 15 |
| BAS1(101) | 38 | 26 | 25 | 43 | 37 | 28 | 25 | 37 |
| BAS2(101) | 47 | 26 | 46 | 38 | 33 | 20 | 30 | 30 |
| LAS1(001) | | -49 | | | | -64 | | |
| LAS2(001) | | -41 | | | | -41 | | |
| LAS1(101) | | -44 | | | | -61 | | |

**Table A.2:** Zero-point vibration energy corrected adsorption energies and Gibbs free energies at 200°C and 400°C for $H_2O$ and pyridine in H-SSZ-13. Values are given in kJ/mol. For BASs, values for adsorption at all Oxygen within the active center are given.

| System | $H_2O$ | | | | Pyridine | | | |
|---|---|---|---|---|---|---|---|---|
| | O1 | O2 | O3 | O4 | O1 | O2 | O3 | O4 |
| | | | | E + ZPVE | | | | |
| BASB | -75 | -59 | -70 | -40 | -171 | -171 | -177 | -176 |
| BAS1(001) | -80 | -49 | -60 | -57 | -157 | -146 | -166 | -171 |
| BAS2(001) | -74 | -37 | -65 | -58 | -167 | -150 | -145 | -170 |
| BAS1(101) | -67 | -67 | -45 | -44 | -147 | -146 | -165 | -147 |
| BAS2(101) | -57 | -74 | -59 | -50 | -165 | -173 | -144 | -156 |
| LAS1(001) | | | -135 | | | | -205 | |
| LAS2(001) | | | -133 | | | | -185 | |
| LAS1(101) | | | -126 | | | | -194 | |
| | | | | $G$ (200) | | | | |
| BASB | -10 | 6 | -3 | 24 | -90 | -93 | -99 | -93 |
| BAS1(001) | -10 | 20 | 7 | 15 | -74 | -67 | -82 | -92 |
| BAS2(001) | -9 | 35 | 1 | 7 | -92 | -67 | -64 | -92 |
| BAS1(101) | 2 | -1 | 19 | 23 | -66 | -59 | -86 | -65 |
| BAS2(101) | 11 | -8 | 5 | 19 | -83 | -89 | -64 | -70 |
| LAS1(001) | | | -65 | | | | -122 | |
| LAS2(001) | | | -62 | | | | -103 | |
| LAS1(101) | | | -62 | | | | -111 | |
| | | | | $G$ (400) | | | | |
| BASB | 19 | 35 | 27 | 53 | -57 | -61 | -68 | -59 |
| BAS1(001) | 22 | 52 | 36 | 47 | -40 | -35 | -48 | -60 |
| BAS2(001) | 20 | 68 | 30 | 36 | -61 | -33 | -31 | -60 |
| BAS1(101) | 33 | 28 | 48 | 53 | -33 | -23 | -54 | -31 |
| BAS2(101) | 41 | 21 | 33 | 50 | -50 | -55 | -32 | -35 |
| LAS1(001) | | | -34 | | | | -88 | |
| LAS2(001) | | | -31 | | | | -71 | |
| LAS1(101) | | | -36 | | | | -77 | |

**Table A.3:** Gibbs free energies at 200°C for step-wise DME formation at BASs considering all four possible oxygen atoms within the active site for catalytic interaction as well as for MeOH and DME adsorption. Values are given in kJ/mol.

| | ZOH+ 2xMeOH(g) | ZOH*MeOH +MeOH(g) | TS-s1 | SMS+$H_2O$(g) +MeOH(g) | TS-s2 | ZOH*DME +$H_2O$(g) | ZOH+DME(g) +$H_2O$(g) |
|---|---|---|---|---|---|---|---|
| | | | | BAS1(001) | | | |
| O1 | 0 | -6 | 130 | -5 | 123 | -18 | -13 |
| O2 | 0 | 5 | 169 | -0 | 137 | -9 | -13 |
| O3 | 0 | -2 | 131 | -0 | 133 | -13 | -13 |
| O4 | 0 | 0 | 152 | -14 | 124 | -27 | -13 |
| | | | | BAS2(001) | | | |
| O1 | 0 | -12 | 145 | -5 | 133 | -20 | -13 |
| O2 | 0 | 3 | 147 | -2 | 140 | -18 | -13 |
| O3 | 0 | 2 | 116 | -2 | 121 | -11 | -13 |
| O4 | 0 | 3 | 159 | -13 | 138 | -27 | -13 |
| | | | | BAS1(101) | | | |
| O1 | 0 | 4 | 153 | 4 | 147 | -8 | -13 |
| O2 | 0 | -6 | 147 | -16 | 125 | -15 | -13 |
| O3 | 0 | -7 | 173 | -3 | 141 | -18 | -13 |
| O4 | 0 | 11 | 155 | -3 | 129 | -8 | -13 |
| | | | | BAS2(101) | | | |
| O1 | 0 | 14 | 141 | -4 | 132 | -13 | -13 |
| O2 | 0 | -7 | 145 | -8 | 132 | -24 | -13 |
| O3 | 0 | 16 | 176 | -1 | 124 | -11 | -13 |
| O4 | 0 | 6 | 157 | -7 | 136 | -14 | -13 |
| | | | | BASB | | | |
| O1 | 0 | -16 | 142 | -9 | 115 | -31 | -13 |
| O2 | 0 | 5 | 137 | -4 | 121 | -17 | -13 |
| O3 | 0 | -1 | 124 | -10 | 119 | -17 | -13 |
| O4 | 0 | 6 | 149 | -11 | 132 | -26 | -13 |

**Table A.4:** Gibbs free energies at 400°C for step-wise DME formation at BASs considering all four possible oxygen atoms within the active site for catalytic interaction as well as for MeOH and DME adsorption. Values are given in kJ/mol.

| | ZOH+ 2xMeOH(g) | ZOH*MeOH +MeOH(g) | TS-s1 | SMS+$H_2O$(g) +MeOH(g) | TS-s2 | ZOH*DME +$H_2O$(g) | ZOH+DME(g) +$H_2O$(g) |
|---|---|---|---|---|---|---|---|
| | | | | BAS1(001) | | | |
| O1 | 0 | 27 | 164 | -2 | 160 | 18 | -9 |
| O2 | 0 | 37 | 204 | 1 | 174 | 26 | -9 |
| O3 | 0 | 32 | 165 | 4 | 170 | 23 | -9 |
| O4 | 0 | 33 | 186 | -11 | 160 | 7 | -9 |
| | | | | BAS2(001) | | | |
| O1 | 0 | 21 | 180 | -2 | 168 | 17 | -9 |
| O2 | 0 | 34 | 182 | 1 | 177 | 17 | -9 |
| O3 | 0 | 36 | 152 | 3 | 161 | 24 | -9 |
| O4 | 0 | 35 | 192 | -11 | 172 | 6 | -9 |
| | | | | BAS1(101) | | | |
| O1 | 0 | 38 | 189 | 7 | 184 | 27 | -9 |
| O2 | 0 | 26 | 181 | -14 | 163 | 19 | -9 |
| O3 | 0 | 25 | 206 | -1 | 176 | 16 | -9 |
| O4 | 0 | 43 | 192 | 1 | 165 | 28 | -9 |
| | | | | BAS2(101) | | | |
| O1 | 0 | 47 | 177 | -1 | 168 | 24 | -9 |
| O2 | 0 | 26 | 180 | -4 | 165 | 11 | -9 |
| O3 | 0 | 46 | 207 | 3 | 161 | 21 | -9 |
| O4 | 0 | 38 | 191 | -5 | 172 | 21 | -9 |
| | | | | BASB | | | |
| O1 | 0 | 16 | 175 | -6 | 153 | 2 | -9 |
| O2 | 0 | 34 | 172 | -1 | 156 | 18 | -9 |
| O3 | 0 | 33 | 158 | -8 | 155 | 20 | -9 |
| O4 | 0 | 36 | 183 | -9 | 168 | 7 | -9 |

**Table A.5:** Cluster-model correction for reaction barriers at BASs referenced to the desorbed acid site. Values are given in kJ/mol.

| | TS-cB | TS-s1 | | | | TS-s1 | | | |
|---|---|---|---|---|---|---|---|---|---|
| | | O1 | O2 | O3 | O4 | O1 | O2 | O3 | O4 |
| BAS1(001) | 35 | 20 | 21 | 18 | 17 | 16 | 18 | 16 | 13 |
| BAS2(001) | 47 | 22 | 20 | 17 | 25 | 26 | 28 | 15 | 19 |
| BAS1(101) | 48 | 24 | 26 | 34 | 20 | 25 | 20 | 29 | 18 |
| BAS1(101) | 37 | 24 | 27 | 27 | 20 | 23 | 25 | 13 | 13 |
| BASB | 51 | 26 | 26 | 25 | 21 | 18 | 26 | 19 | 24 |

**Table A.6:** cluster-model correction for reaction barriers at LASs referenced to the desorbed acid site. Values are given in kJ/mol.

| | TS-cL | TS-r1 | TS-r2 |
|---|---|---|---|
| LAS1(001) | 28 | 6 | 28 |
| LAS2(001) | 33 | 25 | 45 |
| LAS1(101) | 21 | 5 | 22 |

**Table A.7:** Barriers used in the kinetic simulation for the conversion of acetic acid to isobutene in H-SSZ-13. Values are given in kJ/mol.

| Number | Reaction | Forward barrier | Backward barrier |
|---|---|---|---|
| 1 | HO2CMe + ZOH > ZO2CMe O1 pos2 + H2O | 161 | 126 |
| 2 | HO2CMe + ZOH > ZO2CMe O1 pos1 + H2O | 149 | 110 |
| 3 | HO2CMe + ZOH > ZO2CMe O3 + H2O | 153 | 103 |
| 4 | ZO2CMe O1 pos2 > ZOH + Ketene | 86 | 80 |
| 5 | ZO2CMe O3 > ZOH + Ketene | 80 | 89 |
| 6 | HO2CMe + ZOH > CH2C(OH)2 + ZOH | 183 | 65 |
| 7 | ZO2CMe O1 pos1 + Ketene > ZOH + Acetylketene | 117 | 134 |
| 8 | ZO2CMe O1 pos2 + Ketene > ZOH + Acetylketene | 136 | 148 |
| 9 | ZO2CMe O3 + Ketene > D6 | 119 | 50 |
| 10 | ZOH + Acetylketene > D6 | 116 | 20 |
| 11 | ZOH + Acetylketene > D7 | 95 | 62 |
| 12 | D7 + H2O > C5 | 112 | 99 |
| 13 | D6 + H2O > E1 | 36 | 144 |
| 14 | D8 > E1 | 6 | 160 |
| 15 | D6 + H2O > C5 | 37 | 88 |
| 16 | C5 > E1 | 6 | 64 |
| 17 | Acetylketene + H2O > 3-hydroxybut-2-enoic acid | 84 | 77 |
| 18 | 3-hydroxybut-2-enoic acid + ZOH > C5 | 69 | 29 |
| 19 | 3-hydroxybut-2-enoic acid + ZOH > E1 | 128 | 147 |
| 20 | Ketene + Ketene + ZOH > Acetylketene + ZOH | 121 | 139 |
| 21 | Ketene + Ketene + ZOH > D4 | 171 | 141 |
| 22 | Ketene + Ketene + ZOH > D2 | 171 | 47 |
| 23 | D2 + H2O > D3 | 32 | 119 |
| 24 | D3 > D4 + H2O | 154 | 161 |
| 25 | D3 > E1 | 55 | 122 |
| 26 | D4 > D6 | 105 | 56 |
| 27 | ZOH + CH2C(OH)2 + HO2CMe > ZOH + HO2CCHCH(OH)2 | 126 | 101 |
| 28 | ZOH + HO2CCHCH(OH)2 > B3 | 74 | 9 |
| 29 | B3 > C5 + H2O | 34 | 132 |
| 30 | ZOH + HO2CCHCH(OH)2 > E1 + H2O | 240 | 331 |
| 31 | ZO2CMe O1 pos1 + CH2C(OH)2 > E1 | 101 | 208 |
| 32 | ZO2CMe O1 pos2 + CH2C(OH)2 > E1 | 114 | 215 |
| 33 | ZO2CMe O3 + CH2C(OH)2 > E1 | 117 | 233 |
| 34 | HO2CMe + Ketene + ZOH > E1 | 173 | 162 |
| 35 | E1 > ZOH + Propen-2-ol + CO2 | 103 | 169 |
| 36 | ZOH + Propen-2-ol > ZOH + Acetone | 72 | 125 |
| 37 | ZOH + Acetone + Propen-2-ol > E6 | 128 | 20 |
| 38 | E6 > E8 + H2O | 24 | 170 |
| 39 | E8 > ZO2CMe O1 pos1 + Isobutene | 138 | 125 |
| 40 | E8 > ZO2CMe O1 pos2 + Isobutene | 138 | 131 |

**Table A.8:** List of Gibbs free energies for initiation of the MTO process via decarboxylation of lactones and decarbonylation of ketene species at 400 °C. DFT free energies and cluster-model corrected free energies are depicted Reproduced from Ref[116] with permission of Elsevier.

| State | $\Delta G_{\mathrm{DFT}}$ (kJ/mol) | $\Delta G$ (kJ/mol) |
|---|---|---|
| K1 | 51 | 56 |
| TS(K1-K2) | 182 | 216 |
| K2 | 7 | 7 |
| TS(K2-K3) | 124 | 161 |
| K3 | −43 | −49 |
| TS(K3-K4) | 59 | 87 |
| K4 | −72 | −89 |
| TS(K1-ME1) | 141 | 164 |
| ME1 | 0 | 0 |
| TS(K2-ME2) | 91 | 107 |
| ME2 | −39 | −46 |
| TS(K3-ME3) | 42 | 49 |
| ME3 | −79 | −96 |
| TS(K4-ME4) | 24 | 21 |
| ME4 | −123 | −153 |
| TS(K1-P1) | 127 | 188 |
| P1 | 37 | 48 |
| TS(P1-X1) | 167 | 213 |
| X1 | −98 | −98 |
| TS(K2-P2) | 76 | 100 |
| P2 | −14 | −11 |
| TS(P2-X2) | 115 | 153 |
| X2 | −167 | −170 |
| TS(K3-P3) | 13 | 46 |
| P3 | −67 | −74 |
| TS(P3-X3) | 42 | 89 |
| X3 | −228 | −237 |
| TS(K2-N1) | 188 | 168 |
| N1 | −18 | −80 |
| TS(K3-N2) | 72 | 74 |
| N2 | −87 | −152 |
| TS(K4-N3) | −4 | −13 |
| N3 | −148 | −220 |

**Table A.9:** Barriers used in the kinetic simulations for the conversion of methanol to the zeolite surface acetate.[113] Values are given in kJ/mol.

| Number | Reaction | Forward barrier | Backward barrier |
|---|---|---|---|
| 1 | ZOH*MeOH > ZOMe + H2O | 169 | 177 |
| 2 | MeOH + ZOMe > ZOH*DME | 151 | 160 |
| 3 | ZOH*DME > ZOCOMe + H2 | 220 | 153 |
| 4 | MF + ZOH > ZOH*MeOH + CO | 135 | 178 |
| 5 | ZOCOMe + MeOH > DMM + ZOH | 119 | 121 |
| 6 | DMM + ZOH > hacetal + ZOMe | 145 | 137 |
| 7 | hacetal + ZOH > MF + H2 + ZOH | 181 | 249 |
| 8 | CO + ZOMe > ZO2CMe | 190 | 177 |
| 9 | ZOH*MeOH > ZOH + H2 + FA | 226 | 206 |
| 10 | FA + ZOMe > ZOCOMe | 173 | 137 |
| 11 | ZOH + MeOH > ZOH*MeOH | 82 | 80 |
| 12 | ZOH + DME > ZOH*DME | 80 | 81 |
| 13 | ZOH + H2O > ZOH*H2O | 109 | 80 |
| 14 | ZOMe + MeOH > ZOH + CH4 + FA | 237 | 345 |
| 15 | ZOMe + DMM > ZOMe + CH4 + MF | 205 | 394 |
| 16 | ZOMe + hacetal > ZOH + CH4 + MF | 215 | 412 |
| 17 | ZOMe + DME > ZOCOMe + CH4 | 232 | 296 |
| 18 | ZOH*DME + DME > ZOCOMe + CH4 + MeOH | 245 | 299 |
| 19 | ZOH*MeOH + DME > ZOCOMe + CH4 + H2O | 260 | 332 |
| 20 | ZOH*DME + DMM > ZOMe + CH4 + MF + MeOH | 235 | 414 |
| 21 | ZOH*MeOH + DMM > ZOMe + CH4 + MF + H2O | 255 | 452 |
| 22 | ZOH*DME + hacetal > ZOH*MeOH + CH4 + MF | 208 | 394 |
| 23 | ZOH*MeOH + hacetal > ZOH*H2O + CH4 + MF | 248 | 423 |
| 24 | ZOH*MeOH + DME > ZOH*MeOH + CH4 + FA | 228 | 328 |
| 25 | ZOH*MeOH + MeOH > ZOH*H2O + CH4 + FA | 275 | 361 |
| 26 | ZOH*MeOH + MeOH > ZOH*DME + H2O | 192 | 210 |
| 27 | FA + ZOH > ZOH + CO + H2 | 251 | 322 |
| 28 | FA + ZOH*DME > s ch4-fa + ZOH | 274 | 456 |
| 29 | DME + ZOCOMe > s ch4-fa + ZOH | 244 | 456 |

**Table A.10:** Barriers used in the kinetic simulations for methylation reactions within the olefin cycle. [76] Values are given in kJ/mol.

| Number | Reaction | Forward barrier | Backward barrier |
|---|---|---|---|
| 30 | C4b + ZOMe > C5a + ZOH | 147 | 206 |
| 31 | C2 + ZOMe > C3 + ZOH | 176 | 250 |
| 32 | C3 + ZOMe > C4a + ZOH | 155 | 218 |
| 33 | C4a + ZOMe > C5a + ZOH | 154 | 218 |
| 34 | C5a + ZOMe > C6a + ZOH | 132 | 196 |
| 35 | C6a + ZOMe > C7a + ZOH | 146 | 188 |
| 36 | C2 + ZOH*MeOH > C3 + ZOH*H2O | 208 | 260 |
| 37 | C6a + ZOH*MeOH > C7b + ZOH*H2O | 140 | 151 |
| 38 | C7b + ZOH*MeOH > C8b + ZOH*H2O | 156 | 193 |
| 39 | C3 + ZOH*MeOH > C4a + ZOH*H2O | 195 | 236 |
| 40 | C4a + ZOH*MeOH > C5a + ZOH*H2O | 178 | 221 |
| 41 | C5a + ZOH*MeOH > C6a + ZOH*H2O | 157 | 199 |
| 42 | C2 + ZOH*DME > C3 + ZOH*MeOH | 216 | 276 |
| 43 | C3 + ZOH*DME > C4a + ZOH*MeOH | 208 | 258 |
| 44 | C4a + ZOH*DME > C5a + ZOH*MeOH | 195 | 247 |
| 45 | C5a + ZOH*DME > C6a + ZOH*MeOH | 165 | 215 |
| 46 | C6a + ZOH*DME > C7b + ZOH*MeOH | 173 | 192 |
| 47 | C7b + ZOH*DME > C8b + ZOH*MeOH | 165 | 210 |
| 48 | C4a + ZOH*MeOH > C5b + ZOH*H2O | 200 | 232 |
| 49 | C4a + ZOH*DME > C5b + ZOH*MeOH | 207 | 247 |
| 50 | C5b + ZOH*MeOH > C6b + ZOH*H2O | 187 | 216 |
| 51 | C5b + ZOH*DME > C6b + ZOH*MeOH | 208 | 245 |
| 52 | C5b + ZOH*MeOH > C6c + ZOH*H2O | 176 | 219 |
| 53 | C5b + ZOH*DME > C6c + ZOH*MeOH | 183 | 234 |
| 54 | C6b + ZOH*MeOH > C7c + ZOH*H2O | 194 | 227 |
| 55 | C6b + ZOH*DME > C7c + ZOH*MeOH | 194 | 235 |
| 56 | C7c + ZOH*MeOH > C8c + ZOH*H2O | 201 | 229 |
| 57 | C6b + ZOH*MeOH > C7d + ZOH*H2O | 173 | 213 |
| 58 | C6b + ZOH*DME > C7d + ZOH*MeOH | 190 | 238 |
| 59 | C7c + ZOH*MeOH > C8d + ZOH*H2O | 198 | 238 |
| 60 | C7c + ZOH*DME > C8d + ZOH*MeOH | 187 | 234 |
| 61 | C7a + ZOMe > C8a + ZOH | 115 | 169 |
| 62 | C8a + ZOMe > C9a + ZOH | 130 | 156 |
| 63 | C5a + ZOH > C3 + C2 + ZOH | 211 | 185 |
| 64 | C8a + ZOH > C3 + C5a + ZOH | 168 | 183 |
| 65 | C9a + ZOH > C4b + C5a + ZOH | 87 | 145 |
| 66 | C7a + ZOH > C3 + C4a + ZOH | 187 | 191 |
| 67 | C7a + ZOH > C2 + C5a + ZOH | 179 | 174 |
| 68 | C6a + ZOMe > C7b + ZOH | 130 | 162 |
| 69 | C7b + ZOMe > C8b + ZOH | 110 | 168 |
| 70 | C8b + ZOMe > C9a + ZOH | 129 | 160 |
| 71 | C8b + ZOH > C4b + C4a + ZOH | 111 | 135 |
| 72 | C4a + ZOMe > C5b + ZOH | 171 | 223 |
| 73 | C5b + ZOMe > C6c + ZOH | 149 | 213 |
| 74 | C5b + ZOMe > C6b + ZOH | 159 | 209 |
| 75 | C6b + ZOMe > C7c + ZOH | 146 | 200 |
| 76 | C7c + ZOMe > C8c + ZOH | 174 | 222 |
| 77 | C8c + ZOMe > C9b + ZOH | 171 | 220 |
| 78 | C6b + ZOMe > C7d + ZOH | 141 | 202 |
| 79 | C7c + ZOMe > C8d + ZOH | 154 | 214 |
| 80 | C8c + ZOMe > C9c + ZOH | 142 | 208 |

**Table A.11:** Barriers used in the kinetic simulations for cracking reactions within the olefin cycle.[76] Values are given in kJ/mol.

| Number | Reaction | Forward barrier | Backward barrier |
|---|---|---|---|
| 81 | C4a + ZOH > ZOH + C2 + C2 | 246 | 210 |
| 82 | C5b + ZOH > ZOH + C3 + C2 | 238 | 224 |
| 83 | C6c + ZOH > ZOH + C4b + C2 | 186 | 177 |
| 84 | C6c + ZOH > ZOH + C3 + C3 | 199 | 194 |
| 85 | C6b + ZOH > ZOH + C4a + C2 | 211 | 209 |
| 86 | C7d + ZOH > ZOH + C3 + C4a | 209 | 220 |
| 87 | C7d + ZOH > ZOH + C5a + C2 | 168 | 169 |
| 88 | C7c + ZOH > ZOH + C3 + C4a | 215 | 233 |
| 89 | C8c + ZOH > ZOH + C5b + C3 | 200 | 221 |
| 90 | C8d + ZOH > ZOH + C5b + C3 | 236 | 245 |
| 91 | C9b + ZOH > ZOH + C6b + C3 | 201 | 224 |
| 92 | C9c + ZOH > ZOH + C6b + C3 | 233 | 238 |

**Table A.12:** Barriers used in the kinetic simulations for initiation mechanisms of the MTO process via decarboxylation of acrylic acid, decarboxylation of lactones, and decarbonylation of ketenes. Values are given in kJ/mol.

| Number | Reaction | Forward barrier | Backward barrier |
|---|---|---|---|
| 1 | ZO2CMe > Ketene + ZOH | 86 | 80 |
| 2 | ZOH + FA + Ketene > PI1 | 131 | 45 |
| 3 | PI1 > PL + ZOH | 6 | 102 |
| 4 | ZOH + FA + Ketene > PL + ZOH | 239 | 248 |
| 5 | FA + Ketene > PL | 217 | 226 |
| 6 | PL + ZOH > ZOH + CO2 + C2 | 184 | 329 |
| 7 | PL > CO2 + C2 | 165 | 310 |
| 8 | ZOMe + Ketene > ZO2CEt | 166 | 216 |
| 9 | ZO2CEt > ZOH + Mketene | 87 | 80 |
| 10 | ZOH + FA + Mketene > MPL + ZOH | 93 | 111 |
| 11 | ZOH + FA + Mketene > MPL + ZOH | 223 | 241 |
| 12 | FA + Mketene > MPL | 225 | 243 |
| 13 | MPL + ZOH > ZOH + CO2 + C3 | 168 | 327 |
| 14 | MPL > CO2 + C3 | 164 | 323 |
| 15 | ZOMe + Mketene > ZO2CiPr | 161 | 193 |
| 16 | ZO2CiPr > ZOH + Dketene | 80 | 98 |
| 17 | ZOH + FA + Dketene > PI3 | 112 | 53 |
| 18 | PI3 > DPL + ZOH | 7 | 91 |
| 19 | ZOH + FA + Dketene > DPL + ZOH | 95 | 120 |
| 20 | FA + Mketene > DPL | 225 | 1760 |
| 21 | DPL + ZOH > ZOH + CO2 + C4b | 163 | 326 |
| 22 | DPL > CO2 + C4b | 166 | 329 |
| 23 | ZOMe + Dketene > ZO2CtBu | 142 | 176 |
| 24 | ZO2CEt > ZOH + C2 + CO | 168 | 249 |
| 25 | ZO2CiPr > ZOH + C3 + CO | 106 | 227 |
| 26 | ZO2CtBu > ZOH + C4b + CO | 76 | 207 |
| 27 | MeOH + ZO2CMe > MeO2CMe + ZOH | 114 | 164 |
| 28 | MeOH + ZO2CEt > MeO2CEt + ZOH | 106 | 153 |
| 29 | MeOH + ZO2CiPr > MeO2CiPr + ZOH | 80 | 145 |
| 30 | MeOH + ZO2CtBu > MeO2CtBu + ZOH | 110 | 174 |
| 31 | PL + ZOH > PP1 | 111 | 1 |
| 32 | PP1 > SP1 | 46 | 112 |
| 33 | SP1 > ZOH*AA | 112 | 209 |
| 34 | ZOH*AA > ZOH + C2 + CO2 | 236 | 329 |

# B List of Publications

- Philipp Huber, Felix Studt, and Philipp N Plessow. Reactivity of Surface Lewis and Brønsted Acid Sites in Zeolite Catalysis: A Computational Case Study of DME Synthesis Using H-SSZ-13. *J. Phys. Chem. C* 126(13):5896–5905, 2022.

- Philipp N Plessow, Annika E Enss, Philipp Huber, and Felix Studt. A new mechanistic proposal for the aromatic cycle of the MTO process based on a computational investigation for H-SSZ-13. *Catal. Sci. Technol.*, 12(11):3516–3523, 2022.

- Philipp Treu, Philipp Huber, Philipp N Plessow, Felix Studt, and Erisa Saraçi. Lewis acid Sn-Beta catalysts for the cycloaddition of isoprene and methyl acrylate: a greener route to bio-derived monomers. *Catal. Sci. Technol.*, 12(24):7439–7447, 2022.

- Aisulu Aitbekova, Chengshuang Zhou, Michael L Stone, Juan Salvador Lezama-Pacheco, An-Chih Yang, Adam S Hoffman, Emmet D Goodman, Philipp Huber, Jonathan F Stebbins, Karen C Bustillo, Peter Ercius, Jim Ciston, Simon R Bare, Philipp N Plessow, and Matteo Cargnello. Templated encapsulation of platinum-based catalysts promotes high-temperature stability to 1,100 °C. *Nat. Mater.*, 21(11):1290–1297, 2022.

- Philipp Huber and Philipp N Plessow. A computational investigation of the decomposition of acetic acid in H-SSZ-13 and its role in the initiation of the MTO process. *Catal. Sci. Technol.*, 13(6):1905–1917, 2023.

- Philipp Huber and Philipp N Plessow. The role of decarboxylation reactions during the initiation of the methanol-to-olefins process. *J. Catal.*, 428:115134, 2023.

# C Abbreviations

| | |
|---|---|
| 3HP | 3-hydroxypropanoic |
| ALPO | Aluminophosphate |
| BAS | Brønsted Acid Site |
| BSZ | Brønsted Saures Zentrum |
| BZ | Brillouin Zone |
| CBS | Complete Basis Set |
| CC | Coupled Cluster |
| CCSD(T) | Coupled Cluster Singles Doubles (Triples) |
| CM | Cluster Model |
| CHA | Chabazite |
| DFT | Density Functional Theory |
| DLPNO | Domain Based Local Pair Natural Orbital |
| DME | Dimethyl Ether |
| DMM | Dimethoxymethane |
| FA | Formaldehyde |
| GGA | Generalized Gradient Approximation |
| HF | Hartree Fock |
| HT | Hydrogen Transfer |
| LDA | Local density approximation |
| MEP | Minimum Energy Path |
| MF | Methylformate |
| MFI | Mordenite Framework Inverted |
| MP | Møller Plesset |
| MTA | Methanol-to-Aromatics |
| MTG | Methanol-to-Gasoline |
| MTH | Methanol-to-Hydrocarbons |
| MTO | Methanol-to-Olefins |
| LAS | Lewis Acid Site |
| LSZ | Lewis Saures Zentrum |
| PBC | Periodic Boundary Condition |
| PES | Potential Energy Surface |
| RHF | Restricted Hartree Fock |
| SAPO | Silioaluminophosphate |
| SMM | Surface Methylmethoxy |
| SMS | Surface Methoxy Species |
| UHF | Unrestricted Hartree Fock |

# D Acknowledgments

First I want to thank Prof. Dr. Felix Studt for giving me the opportunity to work in his group. His relaxed leadership style and scientific expertise provided me an excellent foundation for my research. Special thanks go to Dr. Philipp Pleßow for guiding me through the PhD process with his sharp mind and great knowledge. Also, thanks for the introduction to the joys of climbing. I want to thank all my colleagues for inspiring insights into their research and for the pleasant atmosphere with thrilling table soccer games. In particular, thanks to my former colleagues Dr. Michal Fečík and Dr. Tiago Goncalves for helping me through the initial period of my PhD and to Dr. Lucas Spiske (alias Dr. Gusch) for proofreading my thesis. I appreciate my interesting collaborations and therefore thank Philipp Treu, Dominik Neukum, Dr. Erisa Saraçi, Dr. Aisulu Aitbekova, Prof. Dr. Matteo Cargnello, Raquel Peláez, and Prof. Dr. Gonzalo Prieto. Vielen Dank an meine Familie für ihre Unterstützung und Geduld während der gesamten Studienzeit. Finally, many thanks to Marie for the mental, language-knowledge, and daily-life support.

# E Eidesstattliche Versicherung

Bei dieser Dissertation handelt es sich um meine eigenständig erbrachte Leistung. Ich habe nur die angegebenen Quellen und Hilfsmittel benutzt und mich keiner unzulässigen Hilfe Dritter bedient. Insbesondere habe ich wörtlich oder sinngemäß aus anderen Werken übernommene Inhalte als solche kenntlich gemacht. Ich habe die "Regeln zur Sicherung guter wissenschaftlicher Praxis am Karlsruher Institut für Technologie (KIT)" beachtet. Die Arbeit oder Teile davon habe ich bislang nicht an einer Hochschule des In- oder Auslands als Bestandteil einer Prüfungs- oder Qualifikationsleistung vorgelegt. Die Richtigkeit der vorstehenden Erklärungen bestätige ich. Die Bedeutung der eidesstattlichen Versicherung und die strafrechtlichen Folgen einer unrichtigen oder unvollständigen eidesstattlichen Versicherung sind mir bekannt. Ich versichere an Eides statt, dass ich nach bestem Wissen die reine Wahrheit erklärt und nichts verschwiegen habe.

# Bibliography


[1] P. Friedlingstein, M. O'sullivan, M. W. Jones, R. M. Andrew, L. Gregor, J. Hauck, C. Le Quéré, I. T. Luijkx, A. Olsen, G. P. Peters, et al. Global Carbon Budget 2022. *Earth System Science Data Discussions*, 2022:1–159, 2022.

[2] M. W. Jones, G. P. Peters, T. Gasser, R. M. Andrew, C. Schwingshackl, J. Gütschow, R. A. Houghton, P. Friedlingstein, J. Pongratz, and C. Le Quéré. National Contributions to Climate Change Due to Historical Emissions of Carbon Dioxide, Methane, and Nitrous Oxide since 1850. *Sci. Data*, 10(1):155, 2023.

[3] Our World in Data, Energy Institute Statistical Review of World Energy. URL `https://ourworldindata.org`. Accessed: 2023-10-12.

[4] Certain Data Included Herein Are Derived from Clarivate Web of Science. © Copyright Clarivate 202, All rights reserved. URL `https://www.webofscience.com`. Accessed: 2023-10-12.

[5] A. Corma, S. Iborra, and A. Velty. Chemical Routes for the Transformation of Biomass into Chemicals. *Chem. Rev.*, 107(6):2411–2502, 2007.

[6] U. Olsbye, S. Svelle, M. Bjørgen, P. Beato, T. V. W. Janssens, F. Joensen, S. Bordiga, and K. P. Lillerud. Conversion of Methanol to Hydrocarbons: How Zeolite Cavity and Pore Size Controls Product Selectivity. *Angew. Chem. Int. Ed.*, 51(24):5810–5831, 2012.

[7] T. Ennaert, J. Van Aelst, J. Dijkmans, R. De Clercq, W. Schutyser, M. Dusselier, D. Verboekend, and B. F. Sels. Potential and Challenges of Zeolite Chemistry in the Catalytic Conversion of Biomass. *Chem. Soc. Rev.*, 45(3):584–611, 2016.

[8] H. Li, A. Riisager, S. Saravanamurugan, A. Pandey, R. S. Sangwan, S. Yang, and R. Luque. Carbon-Increasing Catalytic Strategies for Upgrading Biomass into Energy-Intensive Fuels and Chemicals. *ACS Catal.*, 8(1):148–187, 2018.

[9] M. Stöcker. Methanol-to-Hydrocarbons: Catalytic Materials and Their Behavior. *Microporous Mesoporous Mater.*, 29(1-2):3–48, 1999.

[10] P. Treu, P. Huber, P. N. Plessow, F. Studt, and E. Saraçi. Lewis Acid Sn-Beta Catalysts for the Cycloaddition of Isoprene and Methyl Acrylate: A Greener Route to Bio-Derived Monomers. *Catal. Sci. Technol.*, 12(24):7439–7447, 2022.

[11] A. G. Gayubo, A. T. Aguayo, A. Atutxa, R. Aguado, M. Olazar, and J. Bilbao. Transformation of Oxygenate Components of Biomass Pyrolysis Oil on a HZSM-5 Zeolite. II. Aldehydes, Ketones, and Acids. *Ind. Eng. Chem. Res.*, 43(11):2619–2626, 2004.

[12] C. H. Baerlocher and L. B. McCusker. Database of Zeolite Structures, Structure Commission of the International Zeolite Association. URL `http://www.iza-structure.org/databases/`. Accessed: 2023-09-21.

[13] J. Weitkamp. Zeolites and Catalysis. *Solid State Ion.*, 131(1-2):175–188, 2000.

[14] J. Čejka, G. Centi, J. Perez-Pariente, and W. J. Roth. Zeolite-Based Materials for Novel Catalytic Applications: Opportunities, Perspectives and Open Problems. *Catal.Today*, 179(1):2–15, 2012.

[15] C. S. Cundy and P. A. Cox. The Hydrothermal Synthesis of Zeolites: History and Development from the Earliest Days to the Present Time. *Chem. Rev.*, 103(3):663–702, 2003.

[16] M. Moliner, F. Rey, and A. Corma. Towards the Rational Design of Efficient Organic Structure-Directing Agents for Zeolite Synthesis. *Angew. Chem. Int. Ed.*, 52(52):13880–13889, 2013.

[17] M. E. Davis. Zeolites from a Materials Chemistry Perspective. *Chem. Mater.*, 26(1):239–245, 2014.

[18] K. Momma and F. Izumi. VESTA 3 for Three-Dimensional Visualization of Crystal, Volumetric and Morphology Data. *J. Appl. Crystallogr.*, 44(6):1272–1276, 2011.

[19] J. Li, M. Gao, W. Yan, and J. Yu. Regulation of the Si/Al Ratios and Al Distributions of Zeolites and Its Impact on Properties. *Chem. Sci.*, 2023.

[20] W. Loewenstein. The Distribution of Aluminum in the Tetrahedra of Silicates and Aluminates. *American Mineralogist: Journal of Earth and Planetary Materials*, 39(1-2):92–96, 1954.

[21] A. T. Smith, P. N. Plessow, and F. Studt. Effect of Aluminum Siting in H-ZSM-5 on Reaction Barriers. *J. Phys. Chem. C*, 125(37):20373–20379, 2021.

[22] H. Y. Luo, J. D. Lewis, and Y. Román-Leshkov. Lewis Acid Zeolites for Biomass Conversion: Perspectives and Challenges on Reactivity, Synthesis, and Stability. *Annu. Rev. Chem. Biomol. Eng.*, 7:663–692, 2016.

[23] M. Ravi, V. L. Sushkevich, and J. A. van Bokhoven. Towards a Better Understanding of Lewis Acidic Aluminium in Zeolites. *Nat. Mater.*, 19(10):1047–1056, 2020.

[24] E. V. Khramenkova, H. Venkatraman, V. Soethout, and E. A. Pidko. Global Optimization of Extraframework Ensembles in Zeolites: Structural Analysis of Extraframework Aluminum Species in MOR and MFI Zeolites. *Phys. Chem. Chem. Phys.*, 24(44):27047–27054, 2022.

[25] Y. Li, L. Li, and J. Yu. Applications of Zeolites in Sustainable Chemistry. *Chem*, 3(6):928–949, 2017.

[26] M. E. Davis. Ordered Porous Materials for Emerging Applications. *Nature*, 417(6891):813–821, 2002.

[27] A. Corma. From Microporous to Mesoporous Molecular Sieve Materials and Their Use in Catalysis. *Chem. Rev.*, 97(6):2373–2420, 1997.

[28] E. Pérez-Botella, S. Valencia, and F. Rey. Zeolites in Adsorption Processes: State of the Art and Future Prospects. *Chem. Rev.*, 122(24):17647–17695, 2022.

[29] G. Centi and S. Perathoner. Opportunities and Prospects in the Chemical Recycling of Carbon Dioxide to Fuels. *Catal.Today*, 148(3-4):191–205, 2009.

[30] A. Phan, C. J. Doonan, F. J. Uribe-Romo, C. B. Knobler, M. O'keeffe, and O. M. Yaghi. Synthesis, Structure, and Carbon Dioxide Capture Properties of Zeolitic Imidazolate Frameworks. *Acc. Chem. Res.*, 143(1):58–67, 2010.

[31] M. A. Ghalia and Y. Dahman. Development and Evaluation of Zeolites and Metal–Organic Frameworks for Carbon Dioxide Separation and Capture. *Energy Technol.*, 5(3):356–372, 2017.

[32] V. J. Frillette, W. O. Haag, and R. M. Lago. Catalysis by Crystalline Aluminosilicates: Characterization of Intermediate Pore-Size Zeolites by the "Constraint Index". *Journal of Catalysis*, 67 (1):218–222, 1981.

[33] A. Corma. State of the Art and Future Challenges of Zeolites as Catalysts. *J. Catal.*, 216(1-2): 298–312, 2003.

[34] J. A. Martens, M. Wydoodt, P. Espeel, and P. A. Jacobs. Acid-Catalyzed Ketonization of Mixtures of Low Carbon Number Carboxylic Acids on Zeolite HT. In *Studies in Surface Science and Catalysis*, volume 78, pages 527–534. Elsevier, 1993.

[35] M. Renz. Ketonization of Carboxylic Acids by Decarboxylation: Mechanism and Scope. *Eur. J. Org. Chem.*, 2005(6):979–988, 2005.

[36] M. Wervecken, Y. Servotte, M. Wydoodt, L. Jacobs, J. A. Martens, and P. A. Jacobs. Zeolite-Induced Selectivity in the Conversion of the Lower Aliphatic Carboxylic Acids. In *Chemical Reactions in Organic and Inorganic Constrained Systems*, volume 165, page 95. Springer Science & Business Media, 2012.

[37] O. Kresnawahjuesa, R. J. Gorte, and D. White. Characterization of Acylating Intermediates Formed on H-ZSM-5. *J. Mol. Catal. A Chem.*, 208(1-2):175–185, 2004.

[38] T. Yan, L. Yang, W. Dai, G. Wu, N. Guan, M. Hunger, and L. Li. Cascade Conversion of Acetic Acid to Isobutene over Yttrium-Modified Siliceous Beta Zeolites. *ACS Catal.*, 9(11):9726–9738, 2019.

[39] W. Deng, Q. Zhang, and Y. Wang. Catalytic Transformations of Cellulose and Cellulose-Derived Carbohydrates into Organic Acids. *Catal. Today*, 234:31–41, 2014.

[40] L. Yan and X. Qi. Degradation of Cellulose to Organic Acids in Its Homogeneous Alkaline Aqueous Solution. *ACS Sustain. Chem. Eng.*, 2(4):897–901, 2014.

[41] J. Zhang, M. Sun, X. Liu, and Y. Han. Catalytic Oxidative Conversion of Cellulosic Biomass to Formic Acid and Acetic Acid with Exceptionally High Yields. *Catal. Today*, 233:77–82, 2014.

[42] T. Sarchami, N. Batta, and F. Berruti. Production and Separation of Acetic Acid from Pyrolysis Oil of Lignocellulosic Biomass: A Review. *Biofuels Bioprod. Bioref.*, 15(6):1912–1937, 2021.

[43] J. Grand, S. N. Talapaneni, A. Vicente, C. Fernandez, E. Dib, H. A. Aleksandrov, G. N. Vayssilov, R. Retoux, P. Boullay, J.-P. Gilson, et al. One-Pot Synthesis of Silanol-Free Nanosized MFI Zeolite. *Nat. Mater.*, 16(10):1010–1015, 2017.

[44] R. Kolvenbach, L. F. Gonzalez Peña, A. Jentys, and J. A. Lercher. Diffusion of Mixtures of Light Alkanes and Benzene in Nano-Sized H-ZSM5. *J. Phys. Chem. C*, 118(16):8424–8434, 2014.

[45] Z. Li, M. T. Navarro, J. Martínez-Triguero, J. Yu, and A. Corma. Synthesis of Nano-SSZ-13 and Its Application in the Reaction of Methanol to Olefins. *Catal. Sci. Technol.*, 6(15):5856–5863, 2016.

[46] S. Mintova, M. Jaber, and V. Valtchev. Nanosized Microporous Crystals: Emerging Applications. *Chem. Soc. Rev.*, 44(20):7207–7233, 2015.

[47] Y.-R. He, Y.-L. Zhu, Y. Duan, M. Zhang, and J. Jiang. Green Route to Grow Hierarchical SAPO-34 Crystal with Excellent Catalytic Performance in Methanol to Olefin Reaction. *Cryst. Growth Des.*, 20(1):17–23, 2019.

[48] J. Pérez-Ramírez, C. H. Christensen, K. Egeblad, C. H. Christensen, and J. C. Groen. Hierarchical Zeolites: Enhanced Utilisation of Microporous Crystals in Catalysis by Advances in Materials Design. *Chem. Soc. Rev.*, 37(11):2530–2542, 2008.

[49] C. Pagis, A. R. Morgado Prates, D. Farrusseng, N. Bats, and A. Tuel. Hollow Zeolite Structures: An Overview of Synthesis Methods. *Chem. Mater.*, 28(15):5205–5223, 2016.

[50] E. Koohsaryan and M. Anbia. Nanosized and Hierarchical Zeolites: A Short Review. *Chinese J. Catal.*, 37(4):447–467, 2016.

[51] L. Wu, V. Degirmenci, P. C. M. M. Magusin, N. J. H. G. M. Lousberg, and E. J. M. Hensen. Mesoporous SSZ-13 Zeolite Prepared by a Dual-Template Method with Improved Performance in the Methanol-to-Olefins Reaction. *J. Catal.*, 298:27–40, 2013.

[52] W. J. Roth, P. Nachtigall, R. E. Morris, and J. Cejka. Two-Dimensional Zeolites: Current Status and Perspectives. *Chem. Rev.*, 114(9):4807–4837, 2014.

[53] M. Choi, K. Na, J. Kim, Y. Sakamoto, O. Terasaki, and R. Ryoo. Stable Single-Unit-Cell Nanosheets of Zeolite MFI as Active and Long-Lived Catalysts. *Nature*, 461(7261):246–249, 2009.

[54] J. Přech, P. Pizarro, D. P. Serrano, and J. Čejka. From 3D to 2D Zeolite Catalytic Materials. *Chem. Soc. Rev.*, 47(22):8263–8306, 2018.

[55] L. Treps, C. Demaret, D. Wisser, B. Harbuzaru, A. Methivier, E. Guillon, D. V. Benedis, A. Gomez, T. de Bruin, M. Rivallan, et al. Spectroscopic Expression of the External Surface Sites of H-ZSM-5. *J. Phys. Chem. C*, 125(3):2163–2181, 2021.

[56] S. Bordiga, C. Lamberti, F. Bonino, A. Travert, and F. Thibault-Starzyk. Probing Zeolites by Vibrational Spectroscopies. *Chem. Soc- Rev.*, 44(20):7262–7341, 2015.

[57] J. Rey, P. Raybaud, and C. Chizallet. Ab Initio Simulation of the Acid Sites at the External Surface of Zeolite Beta. *ChemCatChem*, 9(12):2176–2185, 2017.

[58] L. Treps, A. Gomez, T. de Bruin, and C. Chizallet. Environment, Stability and Acidity of External Surface Sites of Silicalite-1 and ZSM-5 Micro and Nano Slabs, Sheets, and Crystals. *ACS Catal.*, 10(5):3297–3312, 2020.

[59] C. Chizallet. Toward the Atomic Scale Simulation of Intricate Acidic Aluminosilicate Catalysts. *ACS Catal.*, 10(10):5579–5601, 2020.

[60] J. Brus, L. Kobera, W. Schoefberger, M. Urbanová, P. Klein, P. Sazama, E. Tabor, S. Sklenak, A. V. Fishchuk, and J. Dědeček. Structure of Framework Aluminum Lewis Sites and Perturbed Aluminum Atoms in Zeolites as Determined by 27Al {1H} REDOR (3Q) MAS NMR Spectroscopy and DFT/Molecular Mechanics. *Angew. Chem. Int. Ed.*, 54(2):541–545, 2015.

[61] M. Ravi, V. L. Sushkevich, and J. A. van Bokhoven. Lewis Acidity Inherent to the Framework of Zeolite Mordenite. *J. Phys. Chem. C*, 123(24):15139–15144, 2019.

[62] J. A. van Bokhoven, A. M. J. Van der Eerden, and D. C. Koningsberger. Three-Coordinate Aluminum in Zeolites Observed with In Situ X-ray Absorption Near-Edge Spectroscopy at the Al K-edge: Flexibility of Aluminum Coordinations in Zeolites. *J. Am. Chem. Soc.*, 125(24):7435–7442, 2003.

[63] M. J. Remy, M. J. Genet, G. Poncelet, P. F. Lardinois, and P. P. Notte. Investigation of Dealuminated Mordenites by X-ray Photoelectron Spectroscopy. *J. Phys. Chem.*, 96(6):2614–2617, 1992.

[64] T. F. Narbeshuber, A. Brait, K. Seshan, and J. A. Lercher. The Influence of Extraframework Aluminum on H-FAU Catalyzed Cracking of Light Alkanes. *Appl. Catal. Al*, 146(1):119–129, 1996.

[65] S. Müller, Y. Liu, F. M. Kirchberger, M. Tonigold, M. Sanchez-Sanchez, and J. A. Lercher. Hydrogen Transfer Pathways during Zeolite Catalyzed Methanol Conversion to Hydrocarbons. *J. Am. Chem. Soc.*, 138(49):15994–16003, 2016.

[66] I. Yarulina, K. De Wispelaere, S. Bailleul, J. Goetze, M. Radersma, E. Abou-Hamad, I. Vollmer, M. Goesten, B. Mezari, E. J. M. Hensen, et al. Structure–Performance Descriptors and the Role of Lewis Acidity in the Methanol-to-Propylene Process. *Nat. Chem.*, 10(8):804–812, 2018.

[67] S. Farzad, M. A. Mandegari, and J. F. Görgens. A Critical Review on Biomass Gasification, Co-Gasification, and Their Environmental Assessments. *Biofuel Res. J.*, 3(4):483–495, 2016.

[68] J. Artz, T. E. Müller, K. Thenert, J. Kleinekorte, R. Meys, A. Sternberg, A. Bardow, and W. Leitner. Sustainable Conversion of Carbon Dioxide: An Integrated Review of Catalysis and Life Cycle Assessment. *Chem. Rev.*, 118(2):434–504, 2018.

[69] X. Zhang, A. O. Oyedun, A. Kumar, D. Oestreich, U. Arnold, and J. Sauer. An Optimized Process Design for Oxymethylene Ether Production from Woody-Biomass-Derived Syngas. *Biomass Bioenergy*, 90:7–14, 2016.

[70] G. A. Olah. Beyond Oil and Gas: The Methanol Economy. *Angew. Chem. Int. Ed.*, 44(18): 2636–2639, 2005.

[71] G. A. Olah. Towards Oil Independence through Renewable Methanol Chemistry. *Angew. Chem. Int. Ed.*, 52(1):104–107, 2013.

[72] W. Song, D. M. Marcus, H. Fu, J. O. Ehresmann, and J. F. Haw. An Oft-Studied Reaction That May Never Have Been: Direct Catalytic Conversion of Methanol or Dimethyl Ether to Hydrocarbons on the Solid Acids HZSM-5 or HSAPO-34. *J. Am. Chem. Soc.*, 124(15):3844–3845, 2002.

[73] J. Amsler, P. N. Plessow, and F. Studt. Effect of Impurities on the Initiation of the Methanol-to-Olefins Process: Kinetic Modeling Based on Ab Initio Rate Constants. *Catal. Lett.*, pages 1–8, 2021.

[74] Y. Jiang, W. Wang, V. R. R. Marthala, J. Huang, B. Sulikowski, and M. Hunger. Effect of Organic Impurities on the Hydrocarbon Formation via the Decomposition of Surface Methoxy Groups on Acidic Zeolite Catalysts. *J. Catal.*, 238(1):21–27, 2006.

[75] W. Wang, A. Buchholz, M. Seiler, and M. Hunger. Evidence for an Initiation of the Methanol-to-Olefin Process by Reactive Surface Methoxy Groups on Acidic Zeolite Catalysts. *J. Am. Chem. Soc*, 125(49):15260–15267, 2003.

[76] P. N. Plessow and F. Studt. Olefin Methylation and Cracking Reactions in H-SSZ-13 Investigated with Ab Initio and DFT Calculations. *Catal. Sci. Technol.*, 8(17):4420–4429, 2018.

[77] R. Y. Brogaard, R. Henry, Y. Schuurman, A. J. Medford, P. G. Moses, P. Beato, S. Svelle, J. K. Nørskov, and U. Olsbye. Methanol-to-Hydrocarbons Conversion: The Alkene Methylation Pathway. *J. Catal.*, 314:159–169, 2014.

[78] J. Van der Mynsbrugge, S. L. C. Moors, K. De Wispelaere, and V. Van Speybroeck. Insight into the Formation and Reactivity of Framework-Bound Methoxide Species in H-ZSM-5 from Static and Dynamic Molecular Simulations. *ChemCatChem*, 6(7):1906–1918, 2014.

[79] D. Lesthaeghe, J. Van der Mynsbrugge, M. Vandichel, M. Waroquier, and V. Van Speybroeck. Full Theoretical Cycle for Both Ethene and Propene Formation during Methanol-to-Olefin Conversion in H-ZSM-5. *ChemCatChem*, 3(1):208–212, 2011.

[80] M. N. Mazar, S. Al-Hashimi, A. Bhan, and M. Cococcioni. Methylation of Ethene by Surface Methoxides: A Periodic PBE+ D Study across Zeolites. *J. Phys. Chem. C*, 116(36):19385–19395, 2012.

[81] K. Hemelsoet, J. Van der Mynsbrugge, K. De Wispelaere, M. Waroquier, and V. Van Speybroeck. Unraveling the Reaction Mechanisms Governing Methanol-to-Olefins Catalysis by Theory and Experiment. *ChemPhysChem*, 14(8):1526–1545, 2013.

[82] S. Xu, A. Zheng, Y. Wei, J. Chen, J. Li, Y. Chu, M. Zhang, Q. Wang, Y. Zhou, J. Wang, et al. Direct Observation of Cyclic Carbenium Ions and Their Role in the Catalytic Cycle of the Methanol-to-Olefin Reaction over Chabazite Zeolites. *Angew. Chem. Int. Ed.*, 52(44):11564–11568, 2013.

[83] J. F. Haw, W. Song, D. M. Marcus, and J. B. Nicholas. The Mechanism of Methanol to Hydrocarbon Catalysis. *Acc. Chem. Res.*, 36(5):317–326, 2003.

[84] M. Fečík, P. N. Plessow, and F. Studt. Theoretical Investigation of the Side-Chain Mechanism of the MTO Process over H-SSZ-13 Using DFT and Ab Initio Calculations. *Catal. Sci. Technol.*, 11 (11):3826–3833, 2021.

[85] M. W. Erichsen, S. Svelle, and U. Olsbye. The Influence of Catalyst Acid Strength on the Methanol to Hydrocarbons (MTH) Reaction. *Catal. Today*, 215:216–223, 2013.

[86] T. Mole, J. A. Whiteside, and D. Seddon. Aromatic Co-Catalysis of Methanol Conversion over Zeolite Catalysts. *J. Catal.*, 82(2):261–266, 1983.

[87] D. Lesthaeghe, A. Horré, M. Waroquier, G. B. Marin, and V. Van Speybroeck. Theoretical Insights on Methylbenzene Side-Chain Growth in ZSM-5 Zeolites for Methanol-to-Olefin Conversion. *Chem. Eur. J.*, 15(41):10803–10808, 2009.

[88] B. Arstad, J. B. Nicholas, and J. F. Haw. Theoretical Study of the Methylbenzene Side-Chain Hydrocarbon Pool Mechanism in Methanol to Olefin Catalysis. *J. Am. Chem. Soc.*, 126(9):2991–3001, 2004.

[89] R. F. Sullivan, C. J. Egan, G. E. Langlois, and R. P. Sieg. A New Reaction That Occurs in the Hydrocracking of Certain Aromatic Hydrocarbons. *J. Am. Chem. Soc.*, 83(5):1156–1160, 1961.

[90] M. Bjørgen, U. Olsbye, and S. Kolboe. Coke Precursor Formation and Zeolite Deactivation: Mechanistic Insights from Hexamethylbenzene Conversion. *J. Catal.*, 215(1):30–44, 2003.

[91] C. Wang, Y. Chu, A. Zheng, J. Xu, Q. Wang, P. Gao, G. Qi, Y. Gong, and F. Deng. Frontispiece: New Insight into the Hydrocarbon-Pool Chemistry of the Methanol-to-Olefins Conversion over Zeolite H-ZSM-5 from GC-MS, Solid-State NMR Spectroscopy, and DFT Calculations. *Chem. Eur. J.*, 20(39), 2014.

[92] C.-M. Wang, Y.-D. Wang, H.-X. Liu, Z.-K. Xie, and Z.-P. Liu. Theoretical Insight into the Minor Role of Paring Mechanism in the Methanol-to-Olefins Conversion within HSAPO-34 Catalyst. *Microporous Mesoporous Mater.*, 158:264–271, 2012.

[93] P. N. Plessow, A. E. Enss, P. Huber, and F. Studt. A New Mechanistic Proposal for the Aromatic Cycle of the MTO Process Based on a Computational Investigation for H-SSZ-13. *Catal. Sci. Technol.*, 12(11):3516–3523, 2022.

[94] M. Bjørgen, U. Olsbye, S. Svelle, and S. Kolboe. Conversion of Methanol to Hydrocarbons: The Reactions of the Heptamethylbenzenium Cation over Zeolite H-Beta. *Catal. Lett*, 93:37–40, 2004.

[95] T. Li, T. Shoinkhorova, J. Gascon, and J. Ruiz-Martinez. Aromatics Production via Methanol-Mediated Transformation Routes. *ACS Catal.*, 11(13):7780–7819, 2021.

[96] E. T. C. Vogt, D. Fu, and B. M. Weckhuysen. Carbon Deposit Analysis in Catalyst Deactivation, Regeneration, and Rejuvenation. *Angew. Chem. Int. Ed.*, 62(29):e202300319, 2023.

[97] I. M. Dahl and S. Kolboe. On the Reaction Mechanism for Propene Formation in the MTO Reaction over SAPO-34. *Catal. Lett.*, 20(3):329–336, 1993.

[98] X. Gong, M. Caglayan, Y. Ye, K. Liu, J. Gascon, and A. D. Chowdhury. First-Generation Organic Reaction Intermediates in Zeolite Chemistry and Catalysis. *Chem. Rev.*, 122(18):14275–14345, 2022.

[99] G. J. Hutchings and R. Hunter. Hydrocarbon Formation from Methanol and Dimethyl Ether: A Review of the Experimental Observations concerning the Mechanism of Formation of the Primary Products. *Catal.Today*, 6(3):279–306, 1990.

[100] D. Lesthaeghe, V. Van Speybroeck, G. B. Marin, and M. Waroquier. Understanding the Failure of Direct C-C Coupling in the Zeolite-Catalyzed Methanol-to-Olefin Process. *Angew. Chem.*, 118 (11):1746–1751, 2006.

[101] G. A. Olah, H. Doggweiler, J. D. Felberg, S. Frohlich, M. J. Grdina, R. Karpeles, T. Keumi, S. Inaba, W. M. Ip, K. Lammertsma, et al. Onium Ylide Chemistry. 1. Bifunctional Acid-Base-Catalyzed Conversion of Heterosubstituted Methanes into Ethylene and Derived Hydrocarbons. The Onium Ylide Mechanism of the C1 - C2 Conversion. *J. Am. Chem. Soc.*, 106(7):2143–2149, 1984.

[102] N. Tajima, T. Tsuneda, F. Toyama, and K. Hirao. A New Mechanism for the First Carbon- Carbon Bond Formation in the MTG Process: A Theoretical Study. *J. Am. Chem. Soc*, 120(32):8222–8229, 1998.

[103] S. R. Blaszkowski and R. A. van Santen. Theoretical Study of C- C Bond Formation in the Methanol-to-Gasoline Process. *J. Am. Chem. Soc.*, 119(21):5020–5027, 1997.

[104] C. D. Chang and A. J. Silvestri. The Conversion of Methanol and Other O-Compounds to Hydrocarbons over Zeolite Catalysts. *J. Catal.*, 47(2):249–259, 1977.

[105] E. A. Swabb and B. C. Gates. Diffusion, Reaction, and Fouling in H-Mordenite Crystallites. The Catalytic Dehydration of Methanol. *Ind. Eng. Chem. Fundam.*, 11(4):540–545, 1972.

[106] P. E. Sinclair and C. R. A. Catlow. Generation of Carbenes during Methanol Conversion over Brønsted Acidic Aluminosilicates. A Computational Study. *J. Phys. Chem. B*, 101(3):295–298, 1997.

[107] J. K. A. Clarke, R. Darcy, B. F. Hegarty, E. O'Donoghue, V. Amir-Ebrahimi, and J. J. Rooney. Free Radicals in Dimethyl Ether on H-ZSM-5 Zeolite. A Novel Dimension of Heterogeneous Catalysis. *J. Chem. Soc., Chem. Commun.*, 5:425–426, 1986.

[108] R. Hunter, G. J. Hutchings, and W. Pickl. Mechanistic Studies on Initial C–C Bond Formation in the Zeolite ZSM-5 Catalysed Methanol Conversion Reaction: Evidence against a Radical Pathway. *J. Chem. Soc., Chem. Commun.*, 11:843–844, 1987.

[109] R. Hunter, G. J. Hutchings, and W. Pickl. Methanol Conversion to Hydrocarbons over the Zeolite Catalyst H-ZSM-5 in the Presence of Oxygen and Nitric Oxide: Further Evidence against a Radical Reaction Mechanism. *J. Chem. Soc., Chem. Commun.*, 18:1369–1371, 1987.

[110] Y. Ono and T. Mori. Mechanism of Methanol Conversion into Hydrocarbons over ZSM-5 Zeolite. *J. Chem. Soc., Farad. Trans. 1*, 77(9):2209–2221, 1981.

[111] J. Li, Z. Wei, Y. Chen, B. Jing, Y. He, M. Dong, H. Jiao, X. Li, Z. Qin, J. Wang, et al. A Route to Form Initial Hydrocarbon Pool Species in Methanol Conversion to Olefins over Zeolites. *J. Catal.*, 317:277–283, 2014.

[112] J. E. Jackson and F. M. Bertsch. Conversion of Methanol to Gasoline: New Mechanism for Formation of the First Carbon-Carbon Bond. *J. Am. Chem. Soc.*, 112(25):9085–9092, 1990.

[113] P. N. Plessow and F. Studt. Unraveling the Mechanism of the Initiation Reaction of the Methanol to Olefins Process Using Ab Initio and DFT Calculations. *ACS Catal.*, 7(11):7987–7994, 2017.

[114] P. N. Plessow, A. Smith, S. Tischer, and F. Studt. Identification of the Reaction Sequence of the MTO Initiation Mechanism Using Ab Initio-Based Kinetics. *J. Am. Chem. Soc.*, 141(14): 5908–5915, 2019.

[115] P. N. Plessow and F. Studt. Theoretical Insights into the Effect of the Framework on the Initiation Mechanism of the MTO Process. *Catal. Lett.*, 148:1246–1253, 2018.

[116] P. Huber and P. N. Plessow. The Role of Decarboxylation Reactions during the Initiation of the Methanol-to-Olefins Process. *J. Catal.*, 428:115134, 2023.

[117] W. Wang and M. Hunger. Reactivity of Surface Alkoxy Species on Acidic Zeolite Catalysts. *Acc. Chem. Res.*, 41(8):895–904, 2008.

[118] S. R. Blaszkowski and R. A. van Santen. The Mechanism of Dimethyl Ether Formation from Methanol Catalyzed by Zeolitic Protons. *J. Am. Chem. Soc*, 118(21):5152–5153, 1996.

[119] E. Sandré, M. C. Payne, and J. D. Gale. First Principles Location of the Transition State for Formation of Dimethyl Ether in a Zeolite. *Chem. Commun.*, 22:2445–2446, 1998.

[120] W. Wang, M. Seiler, and M. Hunger. Role of Surface Methoxy Species in the Conversion of Methanol to Dimethyl Ether on Acidic Zeolites Investigated by In Situ Stopped-Flow MAS NMR Spectroscopy. *J. Phys. Chem. B*, 105(50):12553–12558, 2001.

[121] R. T. Carr, M. Neurock, and E. Iglesia. Catalytic Consequences of Acid Strength in the Conversion of Methanol to Dimethyl Ether. *J. Catal.*, 278(1):78–93, 2011.

[122] P. G. Moses and J. K. Nørskov. Methanol to Dimethyl Ether Over ZSM-22: A Periodic Density Functional Theory Study. *ACS Catal.*, 3(4):735–745, 2013.

[123] A. J. Jones and E. Iglesia. Kinetic, Spectroscopic, and Theoretical Assessment of Associative and Dissociative Methanol Dehydration Routes in Zeolites. *Angew. Chem.*, 126(45):12373–12377, 2014.

[124] A. Ghorbanpour, J. D. Rimer, and L. C. Grabow. Computational Assessment of the Dominant Factors Governing the Mechanism of Methanol Dehydration over H-ZSM-5 with Heterogeneous Aluminum Distribution. *ACS Catal.*, 6(4):2287–2298, 2016.

[125] P. Huber, F. Studt, and P. N. Plessow. Reactivity of Surface Lewis and Brønsted Acid Sites in Zeolite Catalysis: A Computational Case Study of DME Synthesis Using H-SSZ-13. *J. Phys. Chem. C*, 126(13):5896–5905, 2022.

[126] C. E. Bronnimann and G. E. Maciel. Carbon-13 NMR Study of Methanol in HY Zeolite. *J. Am. Chem. Soc.*, 108(23):7154–7159, 1986.

[127] T. R. Forester, S.-T. Wong, and R. F. Howe. In Situ Fourier Transform IR Observation of Methylating Species in ZSM-5. *J. Chem. Soc. Chem. Commun.*, 21:1611–1613, 1986.

[128] T. R. Forester and R. F. Howe. In Situ FTIR Studies of Methanol and Dimethyl Ether in ZSM-5. *J. Am. Chem. Soc.*, 109(17):5076–5082, 1987.

[129] V. Bosáček. Formation of Surface-Bonded Methoxy Groups in the Sorption of Methanol and Methyl Iodide on Zeolites Studied by Carbon-13 MAS NMR Spectroscopy. *J. Phys. Chem.*, 97 (41):10732–10737, 1993.

[130] F. Salehirad and M. W. Anderson. Solid-State NMR Studies of Adsorption Complexes and Surface Methoxy Groups on Methanol-Sorbed Microporous Materials. *J. Catal.*, 177(2):189–207, 1998.

[131] V. Bosáček, R. Klik, F. Genoni, G. Spano, F. Rivetti, and F. Figueras. Terminal and Bridging Methoxyls on Zeolites Detected by 13C Magic Angle Spinning NMR Spectroscopy. *Magn. Reson. Chem.*, 37(13):S135–S141, 1999.

[132] M. Seiler, U. Schenk, and M. Hunger. Conversion of Methanol to Hydrocarbons on Zeolite HZSM-5 Investigated by In Situ MAS NMR Spectroscopy Under Flow Conditions and On-Line Gas Chromatography. *Catal. Lett.*, 62:139–145, 1999.

[133] M. Migliori, A. Aloise, E. Catizzone, and G. Giordano. Kinetic Analysis of Methanol to Dimethyl Ether Reaction over H-MFI Catalyst. *Ind. Eng. Chem. Res.*, 53(38):14885–14891, 2014.

[134] D. Masih, S. Rohani, J. N. Kondo, and T. Tatsumi. Low-Temperature Methanol Dehydration to Dimethyl Ether over Various Small-Pore Zeolites. *Appl. Catal. B*, 217:247–255, 2017.

[135] G. J. Hutchings, F. Gottschalk, and R. Hunter. Comments On" Kinetic Model for Methanol Conversion to Olefins" With Respect to Methane Formation at Low Conversion. *Ind. Eng. Chem. Res.*, 26(3):635–637, 1987.

[136] Y. Liu, F. M. Kirchberger, S. Müller, M. Eder, M. Tonigold, M. Sanchez-Sanchez, and J. A. Lercher. Critical Role of Formaldehyde During Methanol Conversion to Hydrocarbons. *Nat. Commun.*, 10 (1):1–9, 2019.

[137] J. Nováková, L. Kubelková, K. Habersberger, and Z. Dolejšek. Catalytic Activity of Dealuminated Y and HZSM-5 Zeolites Measured by the Temperature-Programmed Desorption of Small Amounts of Preadsorbed Methanol and by the Low-Pressure Flow Reaction of Methanol. *J. Chem. Soc., Faraday Trans. 1*, 80(6):1457–1465, 1984.

[138] J. Nováková, L. Kubelková, and Z. Dolejšek. Primary Reaction Steps in the Methanol-to-Olefin Transformation on Zeolites. *J. Catal.*, 108(1):208–213, 1987.

[139] F. Salehirad and M. W. Anderson. Solid-State13C MAS NMR Study of Methanol-to-Hydrocarbon Chemistry over H-SAPO-34. *J. Catal.*, 164(2):301–314, 1996.

[140] X. Wu, M. G. Abraha, and R. G. Anthony. Methanol Conversion on SAPO-34: Reaction Condition for Fixed-Bed Reactor. *Appl. Catal. A*, 260(1):63–69, 2004.

[141] O. Dewaele, V. L. Geers, G. F. Froment, and G. B. Marin. The Conversion of Methanol to Olefins: A Transient Kinetic Study. *Chem. Eng. Sci.*, 54(20):4385–4395, 1999.

[142] F. M. Kirchberger, Y. Liu, P. N. Plessow, M. Tonigold, F. Studt, M. Sanchez-Sanchez, and J. A. Lercher. Mechanistic Differences between Methanol and Dimethyl Ether in Zeolite-Catalyzed Hydrocarbon Synthesis. *Proc. Natl. Acad. Sci. USA*, 119(4):e2103840119, 2022.

[143] L. Yang, T. Yan, C. Wang, W. Dai, G. Wu, M. Hunger, W. Fan, Z. Xie, N. Guan, and L. Li. Role of Acetaldehyde in the Roadmap from Initial Carbon–Carbon Bonds to Hydrocarbons during Methanol Conversion. *ACS Catal.*, 9(7):6491–6501, 2019.

[144] A. D. Chowdhury, K. Houben, G. T. Whiting, M. Mokhtar, A. M. Asiri, S. A. Al-Thabaiti, S. N. Basahel, M. Baldus, and B. M Weckhuysen. Initial Carbon–Carbon Bond Formation during the Early Stages of the Methanol-to-Olefin Process Proven by Zeolite-Trapped Acetate and Methyl Acetate. *Angew. Chem.*, 128(51):16072–16077, 2016.

[145] Y. Liu, S. Müller, D. Berger, J. Jelic, K. Reuter, M. Tonigold, M. Sanchez-Sanchez, and J. A. Lercher. Formation Mechanism of the First Carbon–Carbon Bond and the First Olefin in the Methanol Conversion into Hydrocarbons. *Angew. Chem.*, 128(19):5817–5820, 2016.

[146] X. Chen, M. L. Neidig, R. Tuinstra, and A. Malek. Direct Observation of Acetyl Group Formation from the Reaction of CO with Methylated H-MOR by In Situ Diffuse Reflectance Infrared Spectroscopy. *J. Phys. Chem. Lett.*, 1(20):3012–3015, 2010.

[147] W. Chen, G. Li, X. Yi, S. J. Day, K. A. Tarach, Z. Liu, S.-B. Liu, S. C. Edman Tsang, K. Góra-Marek, and A. Zheng. Molecular Understanding of the Catalytic Consequence of Ketene Intermediates under Confinement. *J. Am.Chem. Soc.*, 143(37):15440–15452, 2021.

[148] D. B. Rasmussen, J. M. Christensen, B. Temel, F. Studt, P. G. Moses, J. Rossmeisl, A. Riisager, and A. D. Jensen. Ketene as a Reaction Intermediate in the Carbonylation of Dimethyl Ether to Methyl Acetate over Mordenite. *Angew. Chem. Int. Ed.*, 54(25):7261–7264, 2015.

[149] X. Wu, Z. Zhang, Z. Pan, X. Zhou, A. Bodi, and P. Hemberger. Ketenes in the Induction of the Methanol-to-Olefins Process. *Angew. Chem. Int. Ed.*, 2022.

[150] F. Neese, F. Wennmohs, A. Hansen, and U. Becker. Efficient, Approximate and Parallel Hartree–Fock and Hybrid DFT Calculations. A 'Chain-of-Spheres' Algorithm for the Hartree–Fock Exchange. *Chem. Phys.*, 356(1-3):98–109, 2009.

[151] K. Eichkorn, O. Treutler, H. Öhm, M. Häser, and R. Ahlrichs. Auxiliary Basis Sets to Approximate Coulomb Potentials. *Chem. Phys. Lett.*, 240(4):283–290, 1995.

[152] F. Weigend. A Fully Direct RI-HF Algorithm: Implementation, Optimised Auxiliary Basis Sets, Demonstration of Accuracy and Efficiency. *Phys. Chem. Chem. Phys.*, 4(18):4285–4291, 2002.

[153] C. Møller and M. S. Plesset. Note on an Approximation Treatment for Many-Electron Systems. *Phys. Rev.*, 46(7):618, 1934.

[154] F. Jensen. *Introduction to Computational Chemistry*. John wiley & sons, 2017.

[155] D. G. Liakos, M. Sparta, M. K. Kesharwani, J. M. L. Martin, and F. Neese. Exploring the Accuracy Limits of Local Pair Natural Orbital Coupled-Cluster Theory. *J. Chem. Theory Comput.*, 11(4): 1525–1539, 2015.

[156] J. P. Perdew, K. Burke, and M. Ernzerhof. Generalized Gradient Approximation Made Simple. *Phys. Rev. Lett.*, 77(18):3865, 1996.

[157] S. M. Cybulski and C. E. Seversen. Critical Examination of the Supermolecule Density Functional Theory Calculations of Intermolecular Interactions. *J. Chem. Phys.*, 122(1), 2005.

[158] S. Grimme, J. Antony, S. Ehrlich, and H. Krieg. A Consistent and Accurate Ab Initio Parametrization of Density Functional Dispersion Correction (DFT-D) for the 94 Elements H-Pu. *J. Chem. Phys.*, 132(15):154104, 2010.

[159] G. Kresse and D. Joubert. From Ultrasoft Pseudopotentials to the Projector Augmented-Wave Method. *Phys. Rev. B*, 59(3):1758, 1999.

[160] M. Rybicki and J. Sauer. Ab Initio Prediction of Proton Exchange Barriers for Alkanes at Brønsted Sites of Zeolite H-MFI. *J. Am. Chem. Soc.*, 140(51):18151–18161, 2018.

[161] S. Svelle, B. Arstad, S. Kolboe, and O. Swang. A Theoretical Investigation of the Methylation of Alkenes with Methanol over Acidic Zeolites. *J. Phys. Chem. B*, 107(35):9281–9289, 2003.

[162] C. Tuma and J. Sauer. Treating Dispersion Effects in Extended Systems by Hybrid MP2: DFT Calculation–Protonation of Isobutene in Zeolite Ferrierite. *Phys. Chem. Chem. Phys.*, 8(34):3955–3965, 2006.

[163] C. Tuma, T. Kerber, and J. Sauer. The Tert-Butyl Cation in H-Zeolites: Deprotonation to Isobutene and Conversion into Surface Alkoxides. *Angew. Chem. Int. Ed.*, 49(27):4678–4680, 2010.

[164] S. Svelle, C. Tuma, X. Rozanska, T. Kerber, and J. Sauer. Quantum Chemical Modeling of Zeolite-Catalyzed Methylation Reactions: Toward Chemical Accuracy for Barriers. *J. Am. Chem. Soc.*, 131(2):816–825, 2009.

[165] N. Hansen, T. Kerber, J. Sauer, A. T. Bell, and F. J. Keil. Quantum Chemical Modeling of Benzene Ethylation over H-ZSM-5 Approaching Chemical Accuracy: A Hybrid MP2: DFT Study. *J. Am. Chem. Soc.*, 132(33):11525–11538, 2010.

[166] T. J. Goncalves, P. N. Plessow, and F. Studt. On the Accuracy of Density Functional Theory in Zeolite Catalysis. *ChemCatChem*, 11(17):4368–4376, 2019.

[167] P. N. Plessow. Efficient Transition State Optimization of Periodic Structures through Automated Relaxed Potential Energy Surface Scans. *J. Chem. Theory Comput.*, 14(2):981–990, 2018.

[168] G. Henkelman and H. Jónsson. Improved Tangent Estimate in the Nudged Elastic Band Method for Finding Minimum Energy Paths and Saddle Points. *J. Chem. Phys.*, 113(22):9978–9985, 2000.

[169] G. Henkelman, B. P. Uberuaga, and H. Jónsson. A Climbing Image Nudged Elastic Band Method for Finding Saddle Points and Minimum Energy Paths. *J. Chem. Phys.*, 113(22):9901–9904, 2000.

[170] G. Henkelman and H. Jónsson. A Dimer Method for Finding Saddle Points on High Dimensional Potential Surfaces Using Only First Derivatives. *J. Chem. Phys.*, 111(15):7010–7022, 1999.

[171] G. Kresse and J. Hafner. Ab Initio Molecular Dynamics for Liquid Metals. *Phys. Rev. B*, 47: 558–561, Jan 1993.

[172] G. Kresse and J. Hafner. Ab Initio Molecular-Dynamics Simulation of the Liquid-Metal—Amorphous-Semiconductor Transition in Germanium. *Phys. Rev. B*, 49:14251–14269, May 1994.

[173] G. Kresse and J. Furthmüller. Efficiency of Ab-Initio Total Energy Calculations for Metals and Semiconductors Using a Plane-Wave Basis Set. *Comput. Mater. Sci.*, 6(1):15–50, 1996. ISSN 0927-0256.

[174] G. Kresse and J. Furthmüller. Efficient Iterative Schemes for Ab Initio Total-Energy Calculations Using a Plane-Wave Basis Set. *Phys. Rev. B*, 54(16):11169, 1996.

[175] T. H. Dunning Jr. Gaussian Basis Sets for Use in Correlated Molecular Calculations. I. the Atoms Boron through Neon and Hydrogen. *J. Chem. Phys.*, 90(2):1007–1023, 1989.

[176] D. Feller. Application of Systematic Sequences of Wave Functions to the Water Dimer. *J. Chem. Phys.*, 96(8):6104–6114, 1992.

[177] T. Helgaker, W. Klopper, H. Koch, and J. Noga. Basis-Set Convergence of Correlated Calculations on Water. *J. Chem. Phys.*, 106(23):9639–9646, 1997.

[178] C. Riplinger, P. Pinski, U. Becker, E. F. Valeev, and F. Neese. Sparse Maps—a Systematic Infrastructure for Reduced-Scaling Electronic Structure Methods. II. Linear Scaling Domain Based Pair Natural Orbital Coupled Cluster Theory. *J. Chem. Phys.*, 144(2):024109, 2016.

[179] C. Riplinger and F. Neese. An Efficient and Near Linear Scaling Pair Natural Orbital Based Local Coupled Cluster Method. *J. Chem. Phys.*, 138(3), 2013.

[180] F. Neese. The ORCA Program System. *WIREs Comput. Mol. Sci.*, 2(1):73–78, 2012.

[181] F. Weigend and R. Ahlrichs. Balanced Basis Sets of Split Valence, Triple Zeta Valence and Quadruple Zeta Valence Quality for H to Rn: Design and Assessment of Accuracy. *Phys. Chem. Chem. Phys.*, 7(18):3297–3305, 2005.

[182] *A development of University of Karlsruhe and Forschungszentrum Karlsruhe GmbH (1989–2007)*, TURBOMOLE GmbH since 2007. Turbomole V7.4.1, 2019. URL `http://www.turbomole.com`.

[183] M. Fecik, P. N. Plessow, and F. Studt. A Systematic Study of Methylation from Benzene to Hexamethylbenzene in H-SSZ-13 Using Density Functional Theory and Ab Initio Calculations. *ACS Catal.*, 10(15):8916–8925, 2020.

[184] J. Amsler, S. Bernart, P. N. Plessow, and F. Studt. Theoretical Investigation of the Olefin Cycle in H-SSZ-13 for the Ethanol-to-Olefins Process Using Ab Initio Calculations and Kinetic Modeling. *Catal. Sci. Technol.*, 12(10):3311–3321, 2022.

[185] S. Kozuch and S. Shaik. How to Conceptualize Catalytic Cycles? The Energetic Span Model. *Acc. Chem. Ress*, 44(2):101–110, 2011.

[186] L. Sommer, D. Mores, S. Svelle, M. Stöcker, B. M. Weckhuysen, and U. Olsbye. Mesopore Formation in Zeolite H-SSZ-13 by Desilication with NaOH. *Microporous Mesoporous Mater.*, 132(3):384–394, 2010.

[187] H. Ghobarkar, O. Schäf, and P. Knauth. Zeolite Synthesis by the High-Pressure Hydrothermal Method: Synthesis of Natural 6-Ring Zeolites with Different Void Systems. *Angew. Chem. Int. Ed.*, 40(20):3831–3833, 2001.

[188] H. G. Nguyen, G. Konya, E. M. Eyring, D. B. Hunter, and T. N. Truong. Theoretical Study on the Interaction between Xenon and Positively Charged Silver Clusters in Gas Phase and on the (001) Chabazite Surface. *J. Phys. Chem. C*, 113(29):12818–12825, 2009.

[189] G. A. Nasser, O. Muraza, T. Nishitoba, Z. Malaibari, T. K. Al-Shammari, and T. Yokoi. OSDA-Free Chabazite (CHA) Zeolite Synthesized in the Presence of Fluoride for Selective Methanol-to-Olefins. *Microporous Mesoporous Mater.*, 274:277–285, 2019.

[190] Y. Akacem and E. Kassab. Vibrational Analysis of Pyridine Adsorption on the Brønsted Acid Sites of Zeolites Based on Density Functional Cluster Calculations. *J. Phys. Chem. C*, 112(48): 19045–19054, 2008.

[191] J. A. Boscoboinik, X. Yu, E. Emmez, B. Yang, S. Shaikhutdinov, F. D. Fischer, J. Sauer, and H.-J. Freund. Interaction of Probe Molecules with Bridging Hydroxyls of Two-Dimensional Zeolites: A Surface Science Approach. *J. Phys. Chem. C*, 117(26):13547–13556, 2013.

[192] J. A. Lercher, C. Gründling, and G. Eder-Mirth. Infrared Studies of the Surface Acidity of Oxides and Zeolites Using Adsorbed Probe Molecules. *Catal. Today*, 27(3-4):353–376, 1996.

[193] W. Wu and E. Weitz. Modification of Acid Sites in ZSM-5 by Ion-Exchange: An In-Situ FTIR Study. *Appl. Surf. Sci.*, 316:405–415, 2014.

[194] E.-M. El-Malki, R. A. Van Santen, and W. M. H. Sachtler. Introduction of Zn, GA, and Fe into HZSM-5 Cavities by Sublimation: Identification of Acid Sites. *J. Phys. Chem. B*, 103(22): 4611–4622, 1999.

[195] C. H. Kline Jr and J. Turkevich. The Vibrational Spectrum of Pyridine and the Thermodynamic Properties of Pyridine Vapors. *J. Chem. Phys.*, 12(7):300–309, 1944.

[196] A. A. Arvidsson, P. N. Plessow, F. Studt, and A. Hellman. Influence of Acidity on the Methanol-to-DME Reaction in Zeotypes: A First Principles-Based Microkinetic Study. *J. Phys. Chem. C*, 124(27):14658–14663, 2020.

[197] J. R. Di Iorio, A. J. Hoffman, C. T. Nimlos, S. Nystrom, D. Hibbitts, and R. Gounder. Mechanistic Origins of the High-Pressure Inhibition of Methanol Dehydration Rates in Small-Pore Acidic Zeolites. *J. Catal.*, 380:161–177, 2019.

[198] Z. Zhao, H. Shi, C. Wan, M. Y. Hu, Y. Liu, D. Mei, D. M. Camaioni, J. Z. Hu, and J. A. Lercher. Mechanism of Phenol Alkylation in Zeolite H-BEA Using In Situ Solid-State NMR Spectroscopy. *J. Am. Chem. Soc.*, 139(27):9178–9185, 2017.

[199] J. H. Ahn, R. Kolvenbach, S. S. Al-Khattaf, A. Jentys, and J. A. Lercher. Methanol Usage in Toluene Methylation with Medium and Large Pore Zeolites. *ACS Catal.*, 3(5):817–825, 2013.

[200] J. H. Ahn, R. Kolvenbach, O. Y. Gutiérrez, S. S. Al-Khattaf, A. Jentys, and J. A. Lercher. Tailoring P-Xylene Selectivity in Toluene Methylation on Medium Pore-Size Zeolites. *Microporous Mesoporous Mater.*, 210:52–59, 2015.

[201] M. DeLuca, P. Kravchenko, A. Hoffman, and D. Hibbitts. Mechanism and Kinetics of Methylating C6–C12 Methylbenzenes with Methanol and Dimethyl Ether in H-MFI Zeolites. *ACS Catal.*, 9(7): 6444–6460, 2019.

[202] T. A. Semelsberger, R. L. Borup, and H. L. Greene. Dimethyl Ether (DME) as an Alternative Fuel. *J. Power Sources*, 156(2):497–511, 2006.

[203] M. Fečík, P. N. Plessow, and F. Studt. Simple Scheme to Predict Transition-State Energies of Dehydration Reactions in Zeolites with Relevance to Biomass Conversion. *J. Phys. Chem. C*, 122 (40):23062–23067, 2018.

[204] A. Gumidyala, T. Sooknoi, and S. Crossley. Selective Ketonization of Acetic Acid over HZSM-5: The Importance of Acyl Species and the Influence of Water. *J. Catal.*, 340:76–84, 2016.

[205] T. N. Pham, T. Sooknoi, S. P. Crossley, and D. E. Resasco. Ketonization of Carboxylic Acids: Mechanisms, Catalysts, and Implications for Biomass Conversion. *ACS Catal.*, 3(11):2456–2473, 2013.

[206] T. N. Pham, D. Shi, T. Sooknoi, and D. E. Resasco. Aqueous-Phase Ketonization of Acetic Acid over Ru/TiO2/Carbon Catalysts. *J. Catal.*, 295:169–178, 2012.

[207] T. N. Pham, D. Shi, and D. E. Resasco. Evaluating Strategies for Catalytic Upgrading of Pyrolysis Oil in Liquid Phase. *Appl. Catal. B*, 145:10–23, 2014.

[208] T. N. Pham, D. Shi, and D. E. Resasco. Kinetics and Mechanism of Ketonization of Acetic Acid on Ru/TiO2 Catalyst. *Top. Catal.*, 57(6):706–714, 2014.

[209] G. Pacchioni. Ketonization of Carboxylic Acids in Biomass Conversion over TiO2 and ZrO2 Surfaces: A DFT Perspective. *ACS Catal.*, 4(9):2874–2888, 2014.

[210] R. Pestman, A. van Duijne, J. A. Z. Pieterse, and V. Ponec. The Formation of Ketones and Aldehydes from Carboxylic Acids, Structure-Activity Relationship for Two Competitive Reactions. *J. Mol. Catal. A Chem.*, 103(3):175–180, 1995.

[211] R. Pestman, R. M. Koster, A. Van Duijne, J. A. Z. Pieterse, and V. Ponec. Reactions of Carboxylic Acids on Oxides: 2. Bimolecular Reaction of Aliphatic Acids to Ketones. *J. Catal.*, 168(2):265–272, 1997.

[212] M. A. Hasan, M. I. Zaki, and L. Pasupulety. Oxide-Catalyzed Conversion of Acetic Acid into Acetone: An FTIR Spectroscopic Investigation. *Appl. Catal. A: Gen.*, 243(1):81–92, 2003.

[213] S. Wang and E. Iglesia. Experimental and Theoretical Evidence for the Reactivity of Bound Intermediates in Ketonization of Carboxylic Acids and Consequences of Acid–Base Properties of Oxide Catalysts. *J. Phys. Chem. C*, 121(33):18030–18046, 2017.

[214] M. A. Benvenuto and H. Plaumann. *Industrial Catalysis*. Walter de Gruyter GmbH & Co KG, 2021.

[215] V. M. Zakoshansky. The Cumene Process for Phenol-Acetone Production. *Pet. Chem.*, 47(4): 273–284, 2007.

[216] O. Neunhoeffer and P. Paschke. Über den Mechanismus der Ketonbildung aus Carbonsäuren. *Berichte DChG)*, 72(4):919–929, 1939.

[217] P. Huber and P. N. Plessow. A Computational Investigation of the Decomposition of Acetic Acid in H-SSZ-13 and Its Role in the Initiation of the MTO Process. *Catal. Sci. Technol.*, 13(6):1905–1917, 2023.

[218] C. D. Chang, N. Y. Chen, L. R. Koenig, and D. E. Walsh. Synergism in Acetic Acid/Methanol Reactions over ZSM-5 Zeolites. *Prepr. Pap.-Am. Chem. Soc., Div. Fuel Chem.;(United States)*, 28 (CONF-830303-), 1983.

[219] B. Boekaerts and B. F. Sels. Catalytic Advancements in Carboxylic Acid Ketonization and Its Perspectives on Biomass Valorisation. *Appl. Catal. B: Environ.*, 283:119607, 2021.

[220] Y. Zhang, P. Gao, F. Jiao, Y. Chen, Y. Ding, G. Hou, X. Pan, and X. Bao. Chemistry of Ketene Transformation to Gasoline Catalyzed by H-SAPO-11. *J. Am. Chem. Soc.*, 144(40):18251–18258, 2022.

[221] T. Tago, H. Konno, S. Ikeda, S. Yamazaki, W. Ninomiya, Y. Nakasaka, and T. Masuda. Selective Production of Isobutylene from Acetone over Alkali Metal Ion-Exchanged BEA Zeolites. *Catal. Today*, 164(1):158–162, 2011.

[222] P. Reif, N. K. Gupta, and M. Rose. Liquid Phase Aromatization of Bio-Based Ketones over a Stable Solid Acid Catalyst under Batch and Continuous Flow Conditions. *Catal. Commun.*, 163: 106402, 2022.

[223] J. Nováková and L. Kubelková. Reactions of 12C and 13C Acetone Mixtures with a HZSM-5 Zeolite. *J. Catal.*, 126(2):689–692, 1990.

[224] A. I. Biaglow, J. Sepa, R. J. Gorte, and D. White. A 13C NMR Study of the Condensation Chemistry of Acetone and Acetaldehyde Adsorbed at the Brønsted Acid Sites in H-ZSM-5. *J. Catal.*, 151(2):373–384, 1995.

[225] L. Kubelková and J. Nováková. Temperature-Programmed Desorption and Conversion of Acetone and Diethyl Ketone Preadsorbed on HZSM-5. *Zeolites*, 11(8):822–826, 1991.

[226] W. Song, J. B. Nicholas, and J. F. Haw. A Persistent Carbenium Ion on the Methanol-to-Olefin Catalyst HSAPO-34: Acetone Shows the Way. *J. Phys. Chem. B*, 105(19):4317–4323, 2001.

[227] S. Herrmann and E. Iglesia. Selective Conversion of Acetone to Isobutene and Acetic Acid on Aluminosilicates: Kinetic Coupling between Acid-Catalyzed and Radical-Mediated Pathways. *J. Catal.*, 360:66–80, 2018.

[228] S. Herrmann and E. Iglesia. Elementary Steps in Acetone Condensation Reactions Catalyzed by Aluminosilicates with Diverse Void Structures. *J. Catal.*, 346:134–153, 2017.

[229] C.-M. Wang, Y.-D. Wang, and Z.-K. Xie. Methylation of Olefins with Ketene in Zeotypes and Its Implications for the Direct Conversion of Syngas to Light Olefins: A Periodic DFT Study. *Catal. Sci. Technol.*, 6(17):6644–6649, 2016.

[230] A. D. Chowdhury and J. Gascon. The Curious Case of Ketene in Zeolite Chemistry and Catalysis. *Angew. Chem. Int. Ed.*, 57(46):14982–14985, 2018.

[231] K. Zang, W. Zhang, J. Huang, P. Feng, and J. Ding. First Molecule with Carbon–Carbon Bond in Methanol-to-Olefins Process. *Chem. Phys. Lett.*, 737:136844, 2019.

[232] X. Gong, Y. Ye, and A. D. Chowdhury. Evaluating the Role of Descriptor–and Spectator-Type Reaction Intermediates during the Early Phases of Zeolite Catalysis. *ACS Catal.*, 12(24):15463–15500, 2022.

[233] T. L. James and C. A. Wellington. Thermal Decomposition of $\beta$-Propiolactone in the Gas Phases. *J. Am. Chem. Soc.*, 91(27):7743–7746, 1969.

[234] A. Ghorbanpour, J. D. Rimer, and L. C. Grabow. Periodic, vdW-Corrected Density Functional Theory Investigation of the Effect of Al Siting in H-ZSM-5 on Chemisorption Properties and Site-Specific Acidity. *Catal. Commun.*, 52:98–102, 2014.

[235] B. L. Foley, B. A. Johnson, and A. Bhan. Kinetic Evaluation of Deactivation Pathways in Methanol-to-Hydrocarbon Catalysis on HZSM-5 with Formaldehyde, Olefinic, Dieneic, and Aromatic Co-Feeds. *ACS Catal.*, 11(6):3628–3637, 2021.

[236] S. Müller, Y. Liu, M. Vishnuvarthan, X. Sun, A. C. van Veen, G. L. Haller, M. Sanchez-Sanchez, and J. A. Lercher. Coke Formation and Deactivation Pathways on H-ZSM-5 in the Conversion of Methanol to Olefins. *J. Catal.*, 325:48–59, 2015.